University of Modena and Reggio Emilia

Department of Engineering Sciences "E. Ferrari"

Recovery of Interlaminar Tensile Stresses (ILTS) in Curved Laminates Subjected to Bending

Development and Validation of a Computationally Efficient Numerical Method

Advanced Automotive Engineering

Academic Year 2025/2026

Student: Michele Chiomento **ID:** 189830

Supervisor: Prof. Enrico Bertocchi

Acknowledgements

Writing these acknowledgements is perhaps the most difficult part of this entire thesis. Not because words are lacking, but because there are too many of them, and all of them matter. This thesis bears my name on the cover, but within it there are many more people, many more voices, and many more hands than one might imagine. It is the result of a journey that has never been mine alone.

To my mother, Stefania.

My first and deepest thanks are for you, and they come before everything else. Thank you for always being there, in every phase of my life, without ever asking anything in return. Thank you for your profound and constant love, and for the strength with which you have supported me even when I myself did not know where I was going.

You taught me what it truly means to love: a love made of presence, kindness, and simple yet meaningful gestures. You passed on to me generosity, empathy towards others, and sincere attention to those around me. Through the way you live and care, you taught me sensitivity, the value of small things, and the ability to face difficulties without losing humanity.

Even in moments of exhaustion, even when the path seemed longer than expected, you continued to believe in me, often more than I believed in myself. This thesis is also yours, because without your emotional, human, and daily support, it would never have reached completion.

To my father, Stefano.

Thank you for teaching me, through example even more than through words, what it truly means to commit oneself. Thank you for passing on to me tenacity, determination, and the ability to never give up. You have been a solid guide, a reliable presence on whom I could always rely.

You taught me a sense of duty, responsibility, and the value of sacrifice, as well as determination in bringing to completion what one starts. In moments of doubt, fatigue, and uncertainty, the way you face challenges helped me look ahead, grit my teeth, and keep going.

This achievement also bears the mark of your teachings, your trust, and the strength that, often without words, you have transmitted to me day after day.

To my grandparents, Lucia, Rosita, Adriano, and Manlio.

Thank you for being deep and solid roots. Each of you, in your own way, taught me something precious: respect, simplicity, dignity, the importance of family, and the value of memory. You passed on to me an appreciation for time, for things done patiently, and for affection that does not need grand words.

Thank you for the stories, for the glances, for the meaningful gestures, and for your authentic and unconditional love. In you, I have always found a steady point, a safe place, and an example of life shaped by sacrifice, resilience, and humanity. Your presence has quietly built an important part of who I am today.

To my brother, Riccardo.

Thank you for always being there, in good times and bad, in lighter moments as well as in more difficult ones. Thank you for sharing, for exchange, and for a bond made of complicity, differences, and mutual growth.

Growing up together means learning from one another, often without even realising it. With you I have shared paths, challenges, moments of strength and vulnerability. Having a brother means knowing the comfort of never being truly

alone, and this is a value I carry with me every day.

To all other family members.

Thank you for your support, for your sincere interest, and for your words of encouragement along the way. Even when you were not present on a daily basis, I always felt your closeness and your quiet support.

Your presence, even in the simplest and most everyday moments, helped create that sense of balance and belonging which allowed me to face this journey with greater serenity.

To my friends.

Thank you for making this journey lighter. For the laughter, the necessary distractions, the endless conversations, but also for the advice, the support, and your ability to bring me back down to earth when needed.

You have been a fundamental point of reference, a release valve, and a source of energy in moments of fatigue. With you I have shared not only this academic path, but an important part of my personal growth.

And finally, but no less importantly, to the person who stood by my side in a special way.

Thank you for your patience, for your understanding, and for the love shown through everyday gestures. Thank you for sharing anxieties, fatigue, and achievements, without ever making me feel alone.

Your presence has been a constant support, a quiet strength that helped me move forward even in the most challenging moments. This achievement also carries the mark of your closeness and your ability to believe in me.

This achievement is not a point of arrival, but a milestone. And if today I can look ahead with awareness and gratitude, it is because along the way I have never walked alone.

Contents

List of Figures

List of Tables

Abstract

Curved composite laminates are widely employed in aerospace and automotive structures due to their high specific stiffness and strength-to-weight ratio. However, the presence of geometric curvature significantly amplifies out-of-plane stress components, particularly interlaminar tensile stresses (ILTS), which are a primary driver of delamination. Despite their importance, ILTS are not directly available in standard shell finite element formulations, which remain the preferred modeling strategy in industrial practice due to their computational efficiency.

This thesis proposes and validates a computationally efficient numerical post-processing methodology for the recovery of interlaminar tensile stresses in curved laminates subjected to bending. The approach is grounded in laminate theory and shell equilibrium equations, and combines symbolic derivation with numerical implementation. A complete workflow is developed: from theoretical formulation and symbolic manipulation in Maxima, to numerical implementation in Octave, including through-thickness integration, energetic assembly, kernel identification, static condensation, and field reconstruction.

The proposed method reconstructs the interlaminar normal stress component σ_{zz} from shell-based strain and curvature fields without requiring full three-dimensional solid discretization. Validation is performed against high-fidelity 3D finite element models under butterfly bending loading for multiple material configurations, including isotropic aluminum, quasi-isotropic CFRP, sandwich, and "anti-sandwich" laminates. Additional comparison with reference results from literature further confirms

the reliability of the approach.

Results demonstrate that the recovered ILTS distributions closely match solid FEM predictions within a moderate thickness-to-radius range, while significantly reducing computational cost. The methodology enables accurate interlaminar stress estimation within shell-based industrial workflows, thus bridging the gap between computational efficiency and delamination-sensitive design.

The proposed framework represents a robust and extensible strategy for interlaminar stress recovery in curved composite structures and provides a solid foundation for future developments involving complex loading conditions and damage modeling.

Chapter 1

Introduction

1.1 Context and motivations

Over the last few decades, fibre-reinforced polymer matrix composites have become increasingly widespread in numerous industrial sectors, particularly in aerospace and automotive. The reasons for this expansion can be found in the combination of unique properties that these materials offer: high mechanical strength, specific stiffness, lightness, the possibility of creating complex geometries and design freedom that is difficult to achieve with traditional metallic materials. The need to reduce structural weight while maintaining increasingly high levels of safety and performance has led designers and engineers to favour composite solutions, especially in applications where the strength-to-weight ratio is critical to the overall efficiency of the system.

In the aerospace sector, the use of composites is now well established in primary and secondary components. Structures such as fuselages, wing spars, skin panels and internal bulkheads are increasingly being made from curved composite laminates, capable of withstanding complex and variable stresses over time. The immediate benefit lies in weight reduction and, consequently, fuel savings, with significant economic and environmental impacts. However, the large-scale adoption of aerospace

composites also entails greater responsibility in terms of structural safety: a failure due to delamination or interlaminar failure can seriously compromise the integrity of the aircraft, with catastrophic consequences.

Similarly, in the automotive sector, the use of composite materials has gradually expanded from racing cars to some mass-produced vehicles, especially electric and high-end vehicles. The aim is to reduce overall weight, increase the range of electric vehicles and improve dynamic performance. In this context, curved laminates are used in structural elements, chassis, suspensions and body parts. However, safety remains a key issue here too: crash tests and type-approval regulations require precise control of the behaviour of composite materials, especially at critical points where interlaminar stresses can be concentrated.

A crucial aspect common to both sectors is the difficulty of predicting and managing delamination, i.e. the separation between two adjacent layers of the laminate. This phenomenon is closely linked to interlaminar tensile stresses (ILTS), which arise mainly in correspondence with geometric variations (curves, folds, edges), structural discontinuities (holes, inserts, joint areas) or under specific complex load conditions. If not properly assessed during the design phase, ILTS can generate microcracks that evolve into macroscopic delamination, resulting in a reduction in the stiffness and load-bearing capacity of the structure. This translates into high industrial costs, both for extraordinary maintenance and for the replacement of components that are no longer safe, as well as for the possible machine or production line downtime that results.[1]

A further element of complexity arises from the fact that ILTS are not directly observable or easily measurable during experimental testing. Their evaluation requires indirect methodologies, such as tensile or flexural tests on specially made

[1]Hiel, C. C. (1991). *A Curved Beam Test Specimen for Determining the Interlaminar Tensile Strength of a Laminated Composite. Journal of Applied Mechanics*, 58(3), 607–615. `https://doi.org/10.1117/002199839102500705`

samples, or sophisticated non-destructive testing techniques (ultrasound, thermography, X-ray tomography), which, however, involve high costs and long execution times. For this reason, the use of numerical tools, in particular the finite element method (FEM), has become indispensable in supporting the design and validation of composite components. However, the FEM models commonly used in industry – such as shell elements – are not able to directly provide ILTS, as these represent higher-order quantities than the primary variables calculated by the elements. Consequently, it is necessary to adopt post-processing strategies capable of accurately and efficiently reconstructing interlaminar stress fields from the available information.[2]

In this scenario, the motivations behind this research work are clear. On the one hand, there is a growing industrial need for reliable tools to predict and prevent delamination phenomena in curved composite laminates; on the other hand, there is still a gap in the scientific literature regarding numerical methodologies for ILTS recovery that are simultaneously accurate, robust and implementable in industrial FEM codes. The objective of the thesis fits precisely into this context: to propose, describe and validate an innovative numerical strategy that fills this gap, with the aim of making the design of curved composites safer, more efficient and more sustainable.

[2]Zumaquero, P. L., Justo, J., & Graciani, E. (2018). *On the Thickness Dependence of Interlaminar Tensile Strength in Curved Composite Laminates. Key Engineering Materials*, 774, 523–528. https://doi.org/10.4028/www.scientific.net/KEM.774.523

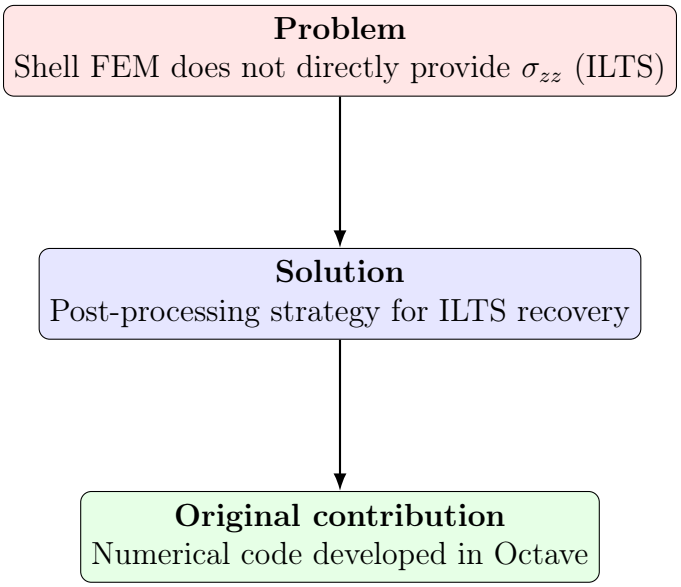

Figure 1.1: Schematic overview: from the limitations of shell FEM to the proposed ILTS recovery method implemented in Octave.

1.2 Delamination in composites: challenges and costs

Delamination is one of the most significant and insidious problems in fibre-reinforced polymer matrix composite materials. It manifests itself as a progressive separation between two or more layers of the laminate and represents an intrinsic weakness in the design and use of multilayer structures. There are many possible causes of this phenomenon, including mechanical factors such as out-of-plane stresses due to tension, shear or bending, and production conditions such as manufacturing defects, inclusions, voids or residual stresses generated during the polymerisation process. In addition to these aspects, there are cyclic loads, accidental impact and thermal gradients, which can act synergistically to accelerate the damage process. Delamination, therefore, is not an isolated phenomenon, but occurs in a complex context of interaction between different types of damage, including microcracking, fibre breakage and fibre-matrix detachment, giving rise to highly non-linear structural behaviour that is difficult to predict.[3]

[3]Huang, T., & Bobyr, M. (2023). *A review of delamination damage of composite materials. Journal of Composites Science*, 7(11), 468. https://doi.org/10.3390/jcs7110468

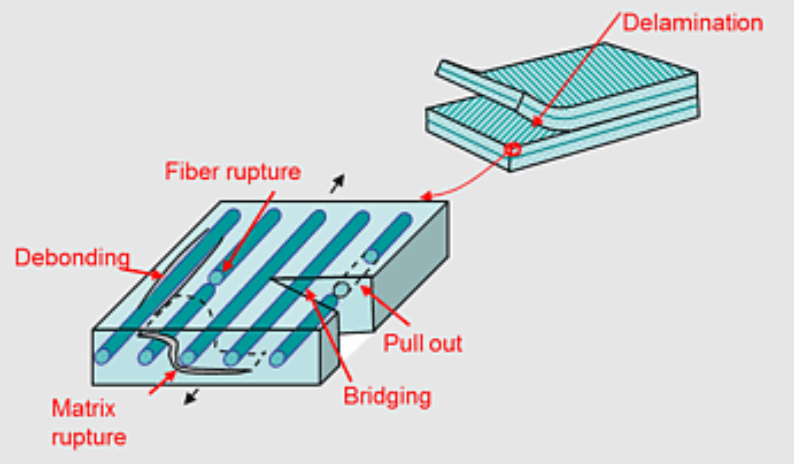

Figure 1.2: Typical damage mechanisms in composite laminates, including matrix rupture, fiber rupture, debonding, pull-out, bridging, and delamination between adjacent plies.

The critical issues arising from the presence of delamination are numerous and have significant consequences on structural performance. One of the main repercussions concerns the reduction in the load-bearing capacity and stiffness of the component: even a small delamination can drastically alter the distribution of stresses, facilitating local instability and precipitating the collapse of the entire structure. This is particularly problematic in aerospace and automotive applications, where safety and reliability are essential requirements and where tolerance for defects is minimised. In addition to reducing strength, delamination increases vulnerability to operating conditions, as it tends to grow over time and under repeated stress, progressively enlarging the compromised area and making the structure more fragile and less predictable.

From an economic point of view, delamination has a significant impact throughout the entire life cycle of the component. During production, the need to check for and eliminate defects requires the use of sophisticated inspection procedures, such as computed tomography, ultrasonography or active thermography, which require additional processing time and high costs. During operation, on the other hand, the appearance of delamination requires frequent maintenance, periodic inspections and,

in the most serious cases, premature replacement of defective components. Although essential to ensure operational safety, these interventions contribute to a significant increase in operating costs, reducing the overall economic efficiency of the system. In the aerospace sector, for example, the need to ensure the full integrity of structures leads to oversized laminates, very high safety margins and complex and costly certification campaigns. In the automotive sector, on the other hand, delamination limits the spread of certain advanced composite components, as the risk of failure and the costs of control are not always sustainable in a mass production context.[4]

Another critical aspect concerns the difficulty of detecting delamination. In fact, it is often invisible to the naked eye and cannot be detected using simple surface inspection methods. The intrinsic nature of the defect, located between the layers of the laminate, requires the use of high-resolution non-destructive methods, which inevitably increase inspection times and costs. This invisibility of the defect also increases engineering and regulatory risk, as the design must take into account the possibility that undetected delamination could compromise structural integrity, imposing additional safety margins and making the certification process even more burdensome.[5]

[4]Taherzadeh-Fard, A., Cornejo, A., Jiménez, S., & Barbu, L. G. (2025). *Numerical analysis of damage in composites: From intra-layer to delamination and data-assisted methods. Mathematics*, 13(10), 1578. https://doi.org/10.3390/math13101578

[5]Seon, G., Choi, J., & Kim, H. (2019). *Measurement of interlaminar tensile strength and elastic properties of CFRP laminates. Applied Sciences*, 9(13), 2647. https://doi.org/10.3390/app9132647

Cause	**Effect**	**Industrial consequence**
Manufacturing defects (voids, inclusions, poor curing)	Initiation of microcracks in the matrix or at interfaces	Reduced service life, premature inspection/repair
Fibre/matrix mismatch or weak interface adhesion	Debonding, fibre pull-out	Loss of stiffness and load transfer efficiency
Geometric discontinuities (holes, free edges, ply drops)	Local stress concentrations, onset of delamination	Design limitations, need for conservative safety margins
Out-of-plane loading (impact, compression, bending–shear coupling)	Interlaminar normal/shear stresses exceed strength	Delamination propagation, structural instability
Thermal gradients / residual stresses	Microcracking and delamination growth under cyclic loads	Increased maintenance and certification costs

Table 1.1: Main causes of delamination in composite laminates, with corresponding effects and industrial consequences.

1.3 Objectives and structure of the thesis

The objectives of this thesis are part of a broader framework concerning the understanding and accurate modelling of interlaminar stresses in curved composite laminates. Scientific and industrial interest in this topic stems from the fact that, despite composite materials having revolutionized the aerospace, automotive and other high-tech sectors, there are still critical issues related to predicting their out-of-plane behaviour. In particular, interlaminar stresses are one of the main causes of delamination, a phenomenon that compromises structural integrity, drastically reduces the useful life of components and increases maintenance and certification costs.

The first major objective of this work is therefore to develop a numerical post-processing strategy capable of estimating interlaminar tensile stresses (ILTS) with high accuracy and computational efficiency from finite element models. The idea is

not to replace classic FEM models, but to integrate them with a recovery method that overcomes the intrinsic limitations of shell-based formulations. Although widely used for their favourable ratio between computational cost and reliability in complex structural analyses, shell-based formulations are unable to directly capture out-of-plane stresses. A post-processing approach, on the other hand, can provide the necessary information without having to resort to solid models with very high mesh density, which would entail calculation times and costs that are unsustainable in industrial applications.

A second fundamental objective concerns the validation of the proposed method through comparison with data available in the literature and with already established approaches, such as derivative or smoothing methods. The decision to proceed with a thorough validation phase responds to the need to position this work within the state of the art, identifying its strengths, application potential and any remaining critical issues. In this sense, the thesis does not merely propose a new tool, but aims to place it within a path of scientific progress that contributes to the improvement of techniques for the analysis and design of curved composites.

A further objective concerns the optimization of the design process: the availability of an efficient post-processing tool makes it possible to reduce excessively conservative safety margins, optimize the use of materials and reduce costs associated with over-design. In the aerospace sector, for example, even a minimal reduction in structural margins translates into significant savings in terms of weight and energy consumption. In the automotive sector, on the other hand, better control of ILTS can promote the wider use of curved composites in safety components, where resistance to delamination is a major barrier to their adoption.

The structure of the thesis has been designed to gradually guide the reader from the general context to a detailed description of the numerical strategy developed. The first chapter introduces the topic, outlining the motivations, the problems of de-

lamination and the specific objectives of this research. The second chapter presents the state of the art, critically analysing the available models and the main techniques proposed in the literature for ILTS recovery. The third chapter provides the theoretical background necessary to understand the fundamentals of laminate theory, the constitutive equations and the limitations of classical models when applied to curved laminates. The second part of the thesis is dedicated to the application and methodology: it describes the proposed numerical post-processing strategy, illustrates the code developed, discusses its implementation and the results obtained, with a specific focus on validation and comparison with data in the literature. The thesis concludes with a final summary chapter, which presents the conclusions, application potential and possible prospects for future research.

In this way, the entire work aims to provide an original contribution to the problem of estimating interlaminar stresses in curved laminates, combining scientific rigour, industrial applicability and methodological innovation.

Chapter 2

State of the Art

Understanding interlaminar stresses in curved composite laminates requires careful analysis of the state of the art, as scientific literature in recent decades has produced a considerable number of theoretical, numerical and experimental studies aimed at investigating the origins, effects and possible methods of mitigating such stresses. Interest in this topic is not accidental: the use of composite materials has grown exponentially over the last thirty years, driven by high-tech sectors such as aerospace, automotive and naval, where weight reduction and increased structural performance are fundamental requirements. However, it is precisely the most complex geometric configurations, such as curves, joints and shells, that have proved particularly critical due to the high incidence of out-of-plane stresses.

Over the years, various approaches have been developed to interpret the behaviour of laminates, ranging from classic formulations of flat laminate theory to the latest numerical techniques for three-dimensional analysis. Research has moved along two main lines: on the one hand, the study of the damage mechanisms that characterise curved composites, and on the other, the search for modelling and calculation strategies capable of overcoming the intrinsic limitations of traditional tools. In this sense, interlaminar stresses have taken on a central role, as they have been identified as one of the main triggers of delamination, a phenomenon which, while

not immediately reducing the overall load-bearing capacity of the component, can seriously compromise its durability and safety.

The literature has highlighted how finite element models based on shell elements, while ensuring fast calculation and simple implementation, are unable to directly capture out-of-plane stresses. This limitation has prompted researchers to develop post-processing methods aimed at the so-called recovery of interlaminar tensile stresses (ILTS). Starting with the pioneering work of Whitney and Pagano[6], who emphasised the need for three-dimensional representation to correctly capture local stress states, up to the most recent formulations based on smoothing and derivative methods, a scientific tradition has been established that attempts to reconcile accuracy and computational sustainability.

At the same time, experimental research has played a fundamental role in validating numerical predictions and highlighting the limitations of theoretical models. Specific tests on curved beams, connectors and panels have shown that interlaminar stresses are not just a negligible detail, but can have a decisive influence on the residual strength and failure mode of composite structures. This direct link between ILTS and delamination has highlighted the urgent need for more sophisticated modelling strategies capable of guiding industrial design towards truly reliable solutions.

The objective of this chapter is therefore twofold: on the one hand, to provide an overview of the main knowledge available on flat and curved laminates, with particular attention to differences in terms of mechanical behaviour and damage phenomena; on the other hand, to critically discuss the numerical methods and ILTS recovery strategies proposed in the literature, highlighting their strengths, limitations and potential for future development. This approach will make it possible

[6]Whitney, J. M., & Pagano, N. J. (1970). *Shear deformation in heterogeneous anisotropic plates. Journal of Applied Mechanics*, 37(4), 1031–1036. https://doi.org/10.1115/1.3408654

to identify the main gaps in knowledge and operations that justify the research conducted in this thesis, outlining the scientific context in which the proposed numerical methodology is situated.

2.1 Composite laminates: flat vs curved configurations

The behaviour of composite laminates varies substantially when moving from flat geometries to curved configurations, and this change is not simply 'geometric': it modifies the coupling mechanisms between stresses and deformations, the order of magnitude of out-of-plane stresses and, consequently, the propensity for delamination.

In flat laminates, Classical Laminate Theory (CLT) generally provides a reliable description of stress and strain states under predominantly membrane loading conditions and for low thickness/span ratios. In this context, the assumption of flat sections that remain flat and the absence of the intrinsic curvature term allow the effects of membrane to be separated relatively clearly from those of bending: tensile/compressive stresses in the plane dominate, while interlaminar stresses (shear and normal) are concentrated near discontinuities (free edges, holes, joints) or in lay-up transitions, often as "boundary layers" that require mesh refinements or post-processing corrections to be accurately captured.[7] Where the thickness or severity of the shear gradient increases, it becomes necessary to switch to first-order theories with transverse shear (FSDT) and specific shear correction factors for orthotropic laminates, in order to avoid underestimating angular deformations and, therefore, out-of-plane stresses. This requirement, already clarified in the classical literature on anisotropic plates, remains the theoretical pillar even when discussing curved configurations, because curvature amplifies the influence of transverse shear and

[7]Maragoni, L., Carraro, P. A., & Quaresimin, M. (2018). *Periodic boundary conditions for FE analyses of a representative volume element for composite laminates with one cracked ply and delaminations. Composite Structures*, 201, 932–941. https://doi.org/10.1016/j.compstruct.2018.06.058

out-of-plane deformations on the overall response.[8]

In curved laminates, the physics of the problem changes in three main ways. First, the presence of intrinsic curvature introduces a geometric coupling between membrane and flexural fields: even a symmetrically stacked laminate (zero B matrix in the plane formulation) can generate membrane forces under a bending moment, or vice versa, due to the curvature terms in the shell equilibrium equations.[9]

This coupling alters the distribution of stresses across the thickness and shifts the interlaminar normal stresses (INS) and interlaminar tensile stresses (ILTS), i.e. the tensile stresses between the layers, which are often responsible for triggering delamination, upwards. Second, the geometric parameter h/R (thickness to radius) controls the relevance of these effects: as h/R increases, the deviations from "flat" kinematics become marked, and out-of-plane fields can no longer be neglected. Thirdly, the lay-up and orientation of the fibres with respect to the main directions of curvature determine "geometric" anisotropies that add to the "material" anisotropies, with local effects on stress peaks near constraints, connections or regions with variable radius.[10]

[8]Mao, K. M., & Sun, C. T. (1991). *A refined global–local finite element analysis method. International Journal for Numerical Methods in Engineering*, 32(1), 29–43. `https://doi.org/10.1002/nme.1620320103`

[9]Reddy, J. N. (2003). *Mechanics of laminated composite plates and shells: Theory and analysis* (2nd ed.).*Boca Raton, FL: CRC Press.*

[10]Roos, R., Kress, G., & Ermanni, P. (2007). *A post-processing method for interlaminar normal stresses in doubly curved laminates. Composite Structures*, 81(3), 463–470. `https://doi.org/10.1016/j.compstruct.2006.09.016`

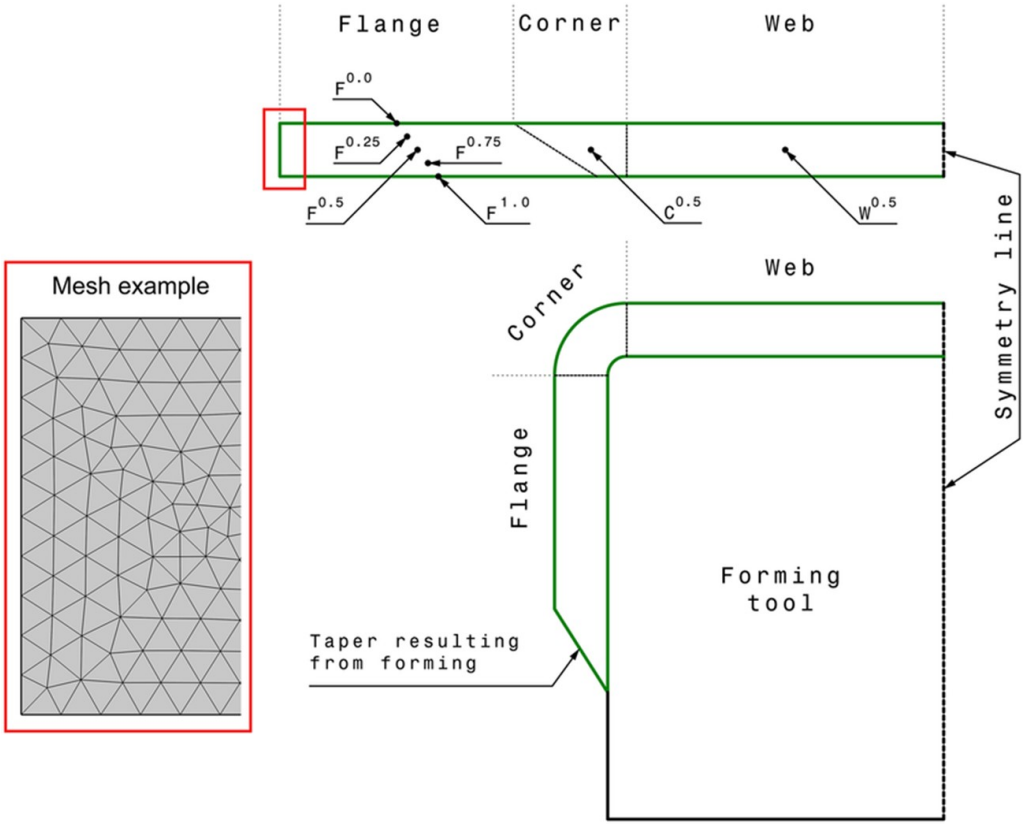

Figure 2.1: Flat laminate.

From the point of view of numerical modelling, the differences between flat and curved are immediately reflected in the choice of elements and the type of reliable output quantities. Modern shell elements represent in-plane stresses well and, with appropriate formulations, also average transverse stresses; however, they do not directly provide interlaminar σ_{zz} (INS/ILTS), which are higher-order quantities related to three-dimensional equilibrium across the thickness. This limitation is particularly critical in curved shells of moderate thickness, where the interaction between curvature, shear and bending produces non-negligible INS distributions. To fill this gap, the literature has developed post-processing methods that reconstruct ILTS from fields calculated with shells, imposing three-dimensional equilibrium or simplified differential formulations in the shell coordinate system. For singly curved laminates, models derived from radial equilibrium, possibly enriched by contributions from transverse shear averaged over the thickness, have been shown to reproduce

the INS distribution with good accuracy compared to solid reference models, with much lower computational costs. The extension to doubly curved structures requires a more sophisticated treatment of curvature terms and derivatives along the principal coordinates of the shell, but still allows for effective recovery of ILTS if the input (average membrane/bending and shear deformations) is well resolved by the shell model. These strategies, designed precisely to bridge the "gap" between what a shell element sees and what is really needed in design, represent a turning point for curved structures: accuracy close to solid modelling can be achieved with calculation times compatible with industrial practice, provided that the domains of validity are adhered to (moderate thicknesses, non-extreme curvature, regularity of the deformation field).[11]

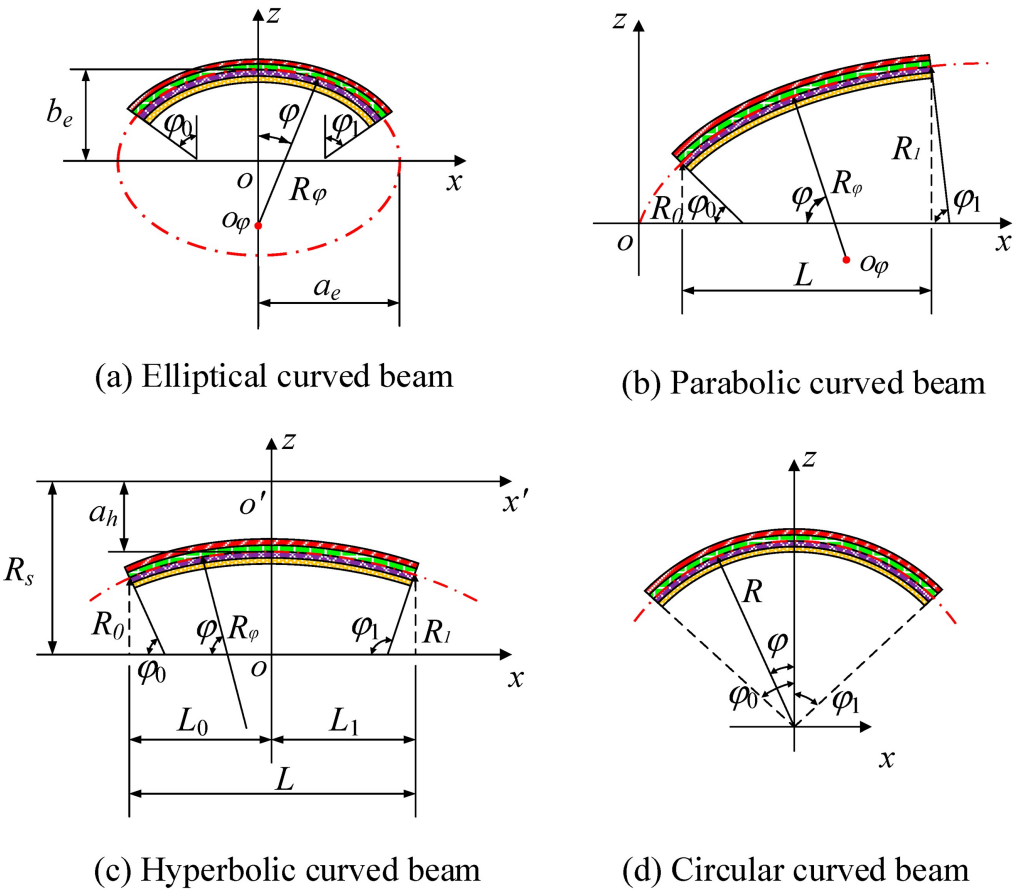

Figure 2.2: Curved laminate.

[11] Roos, R., Kress, G., Barbezat, M., & Ermanni, P. (2007). *Enhanced model for interlaminar normal stress in singly curved laminates. Composite Structures*, 80(3), 327–333. https://doi.org/10.1016/j.compstruct.2006.05.022

The differences between flat and curved laminates also emerge when considering damage. In a flat laminate, the appearance of interlaminar microcracks and the evolution of delamination depend largely on stress states induced by load gradients, free edges and lay-up inhomogeneities. In a curved laminate, the curvature itself is a primary source of stress inhomogeneity: not only does it amplify interlaminar peaks at geometric constraints, but it also creates preferential paths for the initiation of delamination near fibres that are more disadvantaged than the main directions of curvature. In this context, multiscale approaches and Representative Volume Elements (RVE) with periodic boundary conditions have been proposed to study, at the local level, the interaction between intralaminar cracking and delamination in laminates, including general ones; these tools become particularly valuable when one wants to transfer "effective" properties or damage trends to component-scale shell models. The rigorous use of periodic conditions and strategies such as the Virtual Crack Closure Technique (VCCT) facilitates the calculation of release energy and, therefore, the prediction of damage growth in configurations that, if treated in full 3D on the entire component, would be computationally prohibitive. Although not limited to curved geometries, these methodologies are often adopted precisely when curvature makes local fields more complex to reduce to equivalent parameters.

On a system or large component scale, the inevitable difference between local accuracy requirements (for ILTS and delamination initiation) and computational economy has motivated the development of refined global–local strategies. In short, a global analysis is performed on relatively coarse meshes to capture the overall displacement and force fields, then the analysis "zooms in" on regions of interest—typically curved connections, small-radius areas, or areas where the curvature changes rapidly—where finer discretisation or enriched models are used; the local results are finally reinserted into a "refined" global phase to improve consistency and balance. These strategies, which arose as a general response to the inefficiency of uniformly refined 3D models, are particularly effective for curved shells, because the

spatial gradient of the curvature naturally creates domains where the required accuracy is much higher than the average of the component. When combined with ILTS recovery methods, this philosophy allows reliable interlaminar maps to be obtained in critical areas without penalizing the entire model with unsustainable costs.

2.2 Damage mechanisms in curved composites

The phenomenology of damage in curved composite laminates is the result of a non-linear overlap between material anisotropy, geometric curvature and loading conditions which, even when they appear "simple" at a global level, generate locally complex three-dimensional stress states. Compared to flat laminates, in which intralaminar and interlaminar mechanisms can often be analysed by separating the membrane and bending effects with relative approximations, curved structures have an intrinsic coupling between membranes and bending that redistributes stresses through the thickness. This coupling, together with the inevitable presence of shear gradients, makes interlaminar normal and tangential stresses particularly relevant, i.e. precisely those quantities that govern the initiation and propagation of delamination. In other words, curvature acts as an "amplifier" of out-of-plane fields: even for modest thickness/radius ratios, interlaminar tensile stresses can reach critical values near fillet radii, changes in curvature, layer discontinuities and free edges, anticipating the appearance of damage that would appear later or with less intensity in flat plates. At the local level, this translates into the formation of transition zones where the kinematics of the shell deviates from plane kinematics, with the effect of concentrating σ_{zz} and τ_{xz}/ τ_{yz} over characteristic lengths of the order of a few thicknesses, often below the resolution adopted in global design analyses.[12]

The first typical stage of evolution is intralamellar damage to the matrix, in the form of microcracks that develop preferentially in layers with orientations that

[12]Maragoni, L., Carraro, P. A., & Quaresimin, M. (2018). *Periodic boundary conditions for FE analyses of a representative volume element for composite laminates with one cracked ply and delaminations. Composite Structures*, 201, 932–941. https://doi.org/10.1016/j.compstruct.2018.06.058

are unfavourable with respect to the main directions of curvature. In cylindrical or toroidal shells, for example, off-axis laminations can exhibit microcracking at lower load levels than in the plane case, because the curvature modifies the mix of local deformation modes and increases the transverse tensile component across the lamination. This microcracking alters the stress permeability of the layer and changes, in a non-trivial way, both the effective stiffness and the deformation field in the vicinity of the interfaces. The next step is fibre-matrix decohesion along the interfaces of the most stressed reinforcements, which reduces load transfer efficiency and introduces further local heterogeneity. The combination of microcracking and decohesion, in the presence of curvature, tends to generate areas with a strong stiffness gradient which, in turn, intensify interlaminar stresses near edges, holes, laminated ends or ply drops, predisposing the initiation of delamination.[13]

The initiation of delamination in curved laminates cannot be attributed to a single universal mechanism, but rather to a continuous spectrum ranging from conditions close to mode I (opening) to mixtures of modes I/II, with possible contributions from mode III in double curvature configurations or in the presence of torsion. Curvature systematically modifies mode-mixity along the interlaminar crack front, making the distribution of release energy and therefore the "preferred direction" of growth non-uniform. This results in propagation trajectories that follow local mix-mode maxima, with asymmetrical advances of the front, which explains why, in tests on cylindrical arcs or small-radius fittings, delamination tabs that curve or bifurcate are observed. The dependence on the stack sequence is marked: sequences with $\pm 45^\circ$ layers adjacent to $0^\circ/90^\circ$ can generate abrupt transitions in the interlaminar shear field during bending, while lay-ups that are "smoother" with respect to the main bending directions mitigate the peaks. Temperature and thermal gradients also play an important role, because the difference in expansion coefficients and the

[13] Roos, R., Kress, G., & Ermanni, P. (2007). *A post-processing method for interlaminar normal stresses in doubly curved laminates. Composite Structures*, 81(3), 463–470. https://doi.org/10.1016/j.compstruct.2006.09.016

geometric constraint imposed by the curvature introduce out-of-plane residual stress states even in the unloaded state, reducing the margins available under mechanical load.[14]

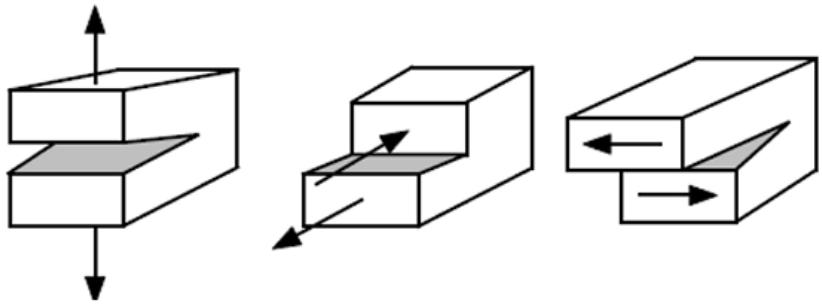

Figure 2.3: Schematic representation of the main delamination fracture modes: Mode I (opening), Mode II (sliding shear), and Mode III (tearing shear).

Under quasi-static static loading, curved shells typically exhibit damage in the order of matrix damage → delamination → fibre rupture, with delamination acting as an "accelerator" of local instability and loss of stiffness, especially in compressed regions where buckling of delaminated sub-lamellae can be triggered. In fatigue, however, curvature accelerates the transition from microcracking to delamination for two concurrent reasons: greater sensitivity to tensile components through the thickness, which amplify cyclic interface openings, and asymmetry of stress fields along the delamination edge, which favours mixed mode propagation. In the presence of impacts or rapid dynamic loads, thickness inertia and curvature-constrained kinematics lead to transient fields of σ_{zz} and $\tau_{xz}/\ \tau_{yz}$ that exceed the peaks expected in quasi-static conditions: This is one of the reasons why curved fillets and thick shells require larger margins or local protections, and why the interpretation of impact test results on curved panels cannot be directly transferred from that on flat panels.[15]

[14]Roos, R., Kress, G., Barbezat, M., & Ermanni, P. (2007). *Enhanced model for interlaminar normal stress in singly curved laminates. Composite Structures*, 80(3), 327–333. `https://doi.org/10.1016/j.compstruct.2006.05.022`

[15]Reddy, J. N. (2003). *Mechanics of laminated composite plates and shells: Theory and analysis* (2nd ed.).*Boca Raton, FL: CRC Press.*

From a modelling point of view, the fact that shell elements do not directly provide interlaminar stresses makes it natural to adopt post-process recovery methodologies. For singly curved shells, models based on radial equilibrium, combined with laminate constitutive relations and, when necessary, with an effective representation of shear through the thickness, allow the distribution of interlaminar normal stresses to be reconstructed with good accuracy and regions at risk of delamination to be predicted in advance. The extension to doubly curved shells requires the inclusion of shell geometry terms and the variation of reduced properties along the surface coordinates, but still allows reliable maps of σ_{zz} and contributions to energy release along the interfaces to be obtained, with a much lower computational cost than a fine 3D solid model of the entire component. The validation of these approaches, comparing the reconstructed fields with solid reference solutions or experimental evidence, has shown that, in a domain of moderate thicknesses and non-extreme curvatures, the difference is often within a few percentage points on the quantities of interest, with savings in time and memory of orders of magnitude. This is an essential interpretation of damage in curved composites: the mechanism does not change in "nature" compared to the flat case, but changes in scale and location, and the calculation tools must shift the focus towards the three-dimensional reconstruction of interlaminar quantities starting from shell results.[16]

The complexity of local damage fields has led, in parallel, to the use of global–local strategies and periodic RVE to isolate and study the interaction between intralaminar cracks and delaminations in representative portions of laminate subjected to load conditions typical of shells. In a global flow, a relatively simple shell model provides the displacements and average magnitudes; locally, at narrow radii, curvature variations or discontinuities, a refined 3D analysis is performed or an RVE with periodic conditions is used to reproduce the repetition of the defect (e.g. a family

[16]Reddy, J. N. (2003). *Mechanics of laminated composite plates and shells: Theory and analysis* (2nd ed.).*Boca Raton, FL: CRC Press.*

of matrix cracks and the delaminations they cause). This allows the energy release rates of the various modes to be calculated accurately and damage growth laws compatible with the shell field to be fed in, without having to solve the entire component in 3D. The rigorous use of periodic conditions, combined with techniques such as the Virtual Crack Closure Technique, is particularly effective when curvature and lay-up generate inhomogeneities that would be costly to describe on a global scale. In practice, damage prediction in a robust curved joint involves an iterative cycle: global shell pre-analysis, local zoom or RVE to extract damage parameters, return to the shell with updated information on stiffness and thresholds. This cycle closes the circle between physical interpretation of mechanisms and industrial feasibility of the calculation.[17]

In terms of theoretical foundations, it is useful to remember that most of the difficulties arise from the fact that, in classical laminate theories derived for flat plates, transverse shear deformations and curvature terms appear in effective form or are even absent, while in real curved structures, shear contributions and geometric terms of the shell directly determine interlaminar quantities. First-order shear deformation extensions and variants with specific shear corrections for orthotropic laminates are intended to consistently reintroduce the shear effect and make that contribution consistent with three-dimensional equilibrium. In curved shells, where kinematics imposes rotations and curvatures that change with position, neglecting or inadequately representing shear leads to systematic underestimations of interlaminar stresses and, consequently, to overly optimistic predictions of delamination onset. For this reason, the most reliable recovery models always start from an accurate description of the average shear and "propagate" its effect in the equilibrium relations along the thickness, so as to obtain profiles of $\sigma_{zz}(\mathrm{z})$ and $\tau(\mathrm{z})$ compatible with the anisotropic behaviour of the laminate and with the curvature of the surface.

[17]Reddy, J. N. (2003). *Mechanics of laminated composite plates and shells: Theory and analysis* (2nd ed.).*Boca Raton, FL: CRC Press.*

The description of the damage mechanisms highlights the importance of accurately estimating interlaminar stresses. The next paragraphs will analyze numerical models and recovery methods, while Chapter 3 will provide the theoretical foundations for the strategy implemented in the developed code.

2.3 Numerical modeling approaches and limitations

The numerical modeling of composite laminates, especially in curved configurations, represents one of the most significant challenges in modern structural engineering. The adoption of numerical approaches stems from the impossibility of relying solely on analytical solutions, which are only feasible for simple geometries and idealized loading conditions. The finite element method (FEM) is now the predominant tool for the analysis of composite structures, thanks to its flexibility in dealing with complex geometries, realistic boundary conditions, and anisotropic material properties. However, despite significant progress in recent decades, FEM applied to curved laminates still has significant limitations, particularly with regard to the evaluation of interlaminar stresses, the prediction of delamination, and the accuracy of out-of-plane response.[18]

The theoretical starting point for numerical modeling of laminates is Classical Laminate Theory (CLT), which is based on the assumption that planes remain flat and that transverse shear deformations are negligible. This theory provides the constitutive relationships between resulting stresses and generalized deformations through the stiffness matrices [A], [B], and [D], so that, for an orthotropic laminate, the fundamental relationship can be written as

$$\begin{bmatrix} \mathbf{N} \\ \mathbf{M} \end{bmatrix} = \begin{bmatrix} \mathbf{A} & \mathbf{B} \\ \mathbf{B} & \mathbf{D} \end{bmatrix} \begin{bmatrix} \boldsymbol{\varepsilon}^0 \\ \boldsymbol{\kappa} \end{bmatrix}$$

[18] Mao, K. M., & Sun, C. T. (1991). *A refined global–local finite element analysis method. International Journal for Numerical Methods in Engineering*, 32(1), 29–43. https://doi.org/10.1002/nme.1620320103

where N represents membrane forces, M represents bending moments, ε^0 represents deformations in the median plane, and κ represents curvatures. This formulation is widely used in numerical codes based on shell elements, which have the great advantage of drastically reducing the number of degrees of freedom compared to 3D solid models. However, the intrinsic limitation is evident: the interlaminar stresses σ_{zz} and τ_{xz}, τ_{yz} do not appear directly in this formulation, because they are "derived" quantities that emerge from three-dimensional equilibrium and are not part of the primary variables of shell elements.[19]

To overcome this shortcoming, several approaches have been developed. The use of solid elements (bricks) allows the three-dimensional stress field to be solved explicitly, providing a complete distribution along the thickness. In theory, a solid model with a sufficiently refined mesh allows the local gradients of interlaminar stresses to be captured and the initiation of delamination to be predicted with greater accuracy. However, the computational cost increases almost prohibitively: a real curved component, such as an aeronautical fitting or an automotive shell, would require millions of degrees of freedom, calculation times, and memory resources that are unsustainable for industrial practice. For this reason, pure solid models are generally reserved for detailed studies on limited regions, while hybrid or shell-based approaches are preferred for the component scale.

Shell elements therefore remain the preferred choice for design, but require post-processing procedures for stress recovery. One of the most common strategies is to impose three-dimensional equilibrium across the thickness to reconstruct σ_{zz}, using the derivatives of the stresses in the plane. A typical expression, simplified in one dimension, is

$$\sigma_{zz}(z) = -\int \left(\frac{\partial \sigma_{xx}}{\partial x} + \frac{\partial \tau_{xz}}{\partial z} \right) dz$$

[19] Roos, R., Kress, G., & Ermanni, P. (2007). *A post-processing method for interlaminar normal stresses in doubly curved laminates. Composite Structures*, 81(3), 463–470. https://doi.org/10.1016/j.compstruct.2006.09.016

which shows how knowledge of in-plane and shear stresses allows interlaminar normals to be estimated. More sophisticated variants include derivative methods, smoothing, and formulations based on enriched shape functions, which can improve the regularity of the reconstructed stress fields. In particular, the work of Roos and colleagues has shown how, even for curved laminates, it is possible to obtain accurate results with low computational costs, provided that the initial shell model provides reliable deformations of the mean plane.

Another significant direction in numerical research is the development of global–local models. The idea is to perform a global analysis with relatively coarse shell elements to capture the general deformations of the component, and then extract local portions at critical areas (curved connections, areas of discontinuity, regions with curvature variation) to be analyzed with more refined models, often 3D solids. This strategy allows local accuracy and computational sustainability to be reconciled. One of the most widely used formulations is based on Mao and Sun's "Refined Global-Local FEM," which involves an iterative cycle of exchange between global and local analysis until consistency is achieved in the displacement and stress fields.[20]

The limitations of numerical approaches become clear when considering damage prediction. Firstly, mesh dependency can introduce significant errors, especially near free edges or lay-up variations, where interlaminar stresses exhibit steep gradients. Secondly, shell models fail to capture out-of-plane behavior in the presence of high thicknesses or pronounced curvatures, circumstances in which the kinematics assumed by shell theory become too restrictive. Thirdly, experimental validation is complex, as direct measurement of ILTS is difficult: as a result, numerical models often have to be calibrated on indirect tests, such as delamination tests or bending tests on curved beams. Finally, there is a constant tension between accuracy

[20]Mao, K. M., & Sun, C. T. (1991). *A refined global–local finite element analysis method. International Journal for Numerical Methods in Engineering*, 32(1), 29–43. `https://doi.org/10.1002/nme.1620320103`

and computational cost: high-fidelity solid models offer superior detail but are not scalable at an industrial level, while shell models are sustainable but require sophisticated corrective procedures to provide useful quantities for the designer.

2.3.1 Accuracy vs computational cost: shell, solid and global–local approaches

One of the central issues in the numerical modelling of curved composite laminates concerns the balance between predictive accuracy and computational cost. This trade-off directly influences the designer's choices and defines the margins within which reliable simulations can be performed without exceeding the limits of available time and resources. In the context of aerospace and automotive design, where analyses must be repeated on numerous geometric configurations and load conditions, evaluating the compromise between simulation fidelity and computational sustainability plays a crucial role.

Shell elements are the most widely used choice in the analysis of large composite structures. Their formulation is based on Classical Laminate Theory (CLT) or its first-order extensions (FSDT), projecting three-dimensional behaviour onto a two-dimensional model centred on the mid-plane. This approach allows for a drastic reduction in the degrees of freedom of the problem, resulting in computational efficiency that makes it possible to model entire aircraft or vehicles. However, due to their simplified nature, shell elements do not directly provide interlaminar stresses, in particular the components normal to the thickness, which are essential for predicting delamination phenomena. These quantities must be recovered through post-processing procedures based on three-dimensional equilibrium or smoothing techniques. As a result, overall accuracy is high for in-plane stresses and deformations, but limited for out-of-plane quantities.

Solid elements, on the other hand, explicitly solve the distribution of stresses

and deformations along the thickness of the laminate. Each layer can be discretised with multiple layers of elements, and the three-dimensional stress fields emerge as primary variables of the solution. This feature allows for a much more accurate representation of interlaminar stresses, local gradients and free edge phenomena. However, the use of solid elements involves a very high computational cost, which increases rapidly with the number of layers and geometric complexity. In curved laminates, where accurate resolution of three-dimensional fields is particularly important, the solid model therefore encounters practical limitations that confine its use to detailed studies and restricted regions of the component.

This scenario is the backdrop for the global–local approach philosophy, designed to integrate the advantages of both strategies. The idea is to use a global shell model to capture the overall behaviour of the structure, keeping computational costs down, and to focus the solid model on regions of interest, such as connection areas, free edges or geometric discontinuities. The global solution provides the boundary conditions for local three-dimensional analysis, which in turn allows interlaminar stress peaks and potential delamination triggers to be verified. This two-level scheme allows a systemic view to be maintained while at the same time delving into critical details, striking an effective compromise between accuracy and computational cost.

The comparison between these three approaches can be summarised in the following table:

Numerical approach	**Accuracy on in-plane stresses**	**Accuracy on out-of-plane stresses (ILTS)**	**Computational cost**	**Typical application field**
Shell	High	Limited, requires post-processing	Low	Global analysis of large structures; preliminary design
Solid	Very high	Very high	Very high	Local detailed analysis; validation of reduced models
Global–local	High at global scale	High at local scale, depending on sub-model	Medium–high	Critical zones (joints, free edges); compromise between efficiency and accuracy

Table 2.1: Comparison of numerical approaches for curved composite laminates.

This comparison highlights how the choice of method depends heavily on the objective of the analysis. In the initial design stages or in very large structures, shells are the most practical solution, bearing in mind that ILTS must be evaluated using additional methods. When the objective is to accurately predict delamination phenomena or evaluate performance in areas subject to high stress, solid elements guarantee a higher level of detail, albeit with longer calculation times. Finally, global-local approaches offer an integrated strategy that combines an overview with local detail, making them particularly suitable for industrial scenarios where resources and time need to be optimised without compromising the reliability of the prediction.

2.4 Recovery methods for ILTS

The numerical recovery of interlaminar tensile stresses (ILTS) in curved composite laminates arises from the practical and theoretical need to reconstruct out-of-plane quantities that are not primary variables in common shell elements. In real design, laminated shells are often modeled with equivalent single-layer (ESL) theories and plate/shell degrees of freedom: these formulations reproduce membrane and flexural states with excellent efficiency, but do not directly provide the normal stresses to the thickness, i.e., the σ_{zz} across the interfaces, which govern the initiation of delamination. Post-processing methods bridge the gap between an "economical" shell model and the three-dimensional information needed for dimensioning, integrating, regularizing, or "enriching" the FEM results to recover the ILTS with engineering accuracy even in the presence of curvature. This section outlines the principles, the most authoritative variants, and the known limitations of recovery methods, with specific reference to singly and doubly curved configurations.

The common foundation is three-dimensional equilibrium. In Cartesian coordinates, local equilibrium requires that

$$\begin{aligned}
\frac{\partial \sigma_{xx}}{\partial x} + \frac{\partial \sigma_{xy}}{\partial y} + \frac{\partial \sigma_{xz}}{\partial z} &= 0, \\
\frac{\partial \sigma_{yx}}{\partial x} + \frac{\partial \sigma_{yy}}{\partial y} + \frac{\partial \sigma_{yz}}{\partial z} &= 0, \\
\frac{\partial \sigma_{zx}}{\partial x} + \frac{\partial \sigma_{zy}}{\partial y} + \frac{\partial \sigma_{zz}}{\partial z} &= 0.
\end{aligned}$$

From the latter, integrating along the thickness, a "weak" reconstruction of σ_{zz} is obtained starting from the plane derivatives of the shear stresses:

$$\sigma_{zz}(z) = \sigma_{zz}(z_0) - \int_{z_0}^{z} \left(\frac{\partial \sigma_{zx}}{\partial x} + \frac{\partial \sigma_{zy}}{\partial y} \right) \mathrm{d}z'.$$

The boundary condition

$$\sigma_{zz}\big(z = \pm h/2\big) = t_z$$

(tension applied to the faces) closes the problem; in the absence of external pressures, typically

$$\sigma_{zz}\left(\pm\frac{h}{2}\right) = 0.$$

This idea—integrating equilibrium using the in-plane fields of the shell model as "drivers"—is the basis of derivative methods: the accuracy of the recovery depends on the quality of the membrane stresses and average cross-sections provided by the shell and on the numerical regularity with which the spatial derivatives are calculated. In curved shells, kinematics introduces additional geometric terms: for example, in cylindrical coordinates for an axisymmetric state, the radial equilibrium takes the form

$$\frac{\partial \sigma_{rr}}{\partial r} + \frac{\sigma_{rr} - \sigma_{\theta\theta}}{r} + \frac{\partial \tau_{rz}}{\partial z} = 0,$$

which highlights the curvature effect through the term

$$\frac{\sigma_{rr} - \sigma_{\theta\theta}}{r}.$$

Integrating this equation along z allows the INS/ILTS to be reconstructed in singly curved configurations as a function of in-plane and shear fields calculated by the shell model; correctly including curvature contributions is crucial to avoid systematic underestimations of σ_{zz}. The contributions of Kress–Roos–Barbezat and the subsequent refinements of Roos–Kress–Ermanni are along these lines, having formalized post-processing procedures for moderately thick laminates in singly and doubly curved geometries: the first model derives the interlaminar radial stresses by imposing equilibrium across the thickness and using shell deformations/results as input; the "enhanced" model introduces the role of interlaminar shear and curvature

terms in a consistent form, improving the prediction of peaks and the shape of the profile across the thickness, while the extension to doubly curved shells generalizes the procedure in surface coordinates, maintaining the non-intrusive philosophy and reduced cost compared to full 3D. In all cases, the operating assumption is clear: if the shell provides reliable global fields, the three-dimensional equilibrium "stitches" the missing information together with typically small errors for moderate h/R and regular geometries.

Alongside derivative methods, a second approach leverages smoothing/patch recovery techniques to regularize fields before applying equilibrium. Since the calculation of spatial derivatives amplifies numerical noise, many authors adopt local windows (patches) and least squares approximations to "smooth" σ_{xx}, σ_{yy}, τ_{xy}, and the average cuts of the shell, then apply integration in z. In practice, an anisotropic version of the classic Superconvergent Patch Recovery is implemented, oriented towards out-of-plane reconstruction. In curved shells, smoothing is combined with metric terms (such as 1/r) to maintain equilibrium in curvilinear form; more recent works have proposed unified procedures for arbitrarily curved shells, integrating the equilibrium in surface coordinates: these are lightweight post-processors which, given the displacements and results of the shell, return σ_{zz} and interlaminar with accuracy surprisingly close to solid models in the most common industrial thickness range.

The bottleneck is not only theoretical but also numerical. In curved shells, ILTSs have boundary layers and peaks located at free edges, fillets, radius changes, ply drops, and discontinuities; these are regions where spatial derivatives "see" discontinuities or strong gradients and where a shell that is too coarse can provide irregular starting fields. To overcome this, many computational flows adopt global–local strategies: a global analysis with shells defines the average fields, then a 3D zoom is performed on critical curved subdomains to calibrate or verify the recovery; fi-

nally, the local results inform the global post-processor (e.g., with correction factors or smoothing parameters). The family of refined global-local methods allows this exchange in an iterative and controlled manner, keeping the computational burden sustainable: it is a natural bridge between an efficient shell and the necessary three-dimensional resolution where curvature imposes non-negligible out-of-plane fields.

An often overlooked point is the constitutive consistency between the shell theory used and the recovery. CLT/FSDT theories provide N, M, and, if applicable, average Q results consistent with a certain shear profile across the thickness; post-processing must be compatible with this profile, otherwise systematic balance errors will be introduced. Enhanced formulations for curved laminates explicitly include the effect of shear in thickness in the equilibrium relation that leads to σ_{zz}(z), avoiding the typical error of models that only integrate divergence in the plane. Furthermore, in doubly curved shells, post-processing must respect the covariant derivatives on the surface, including Christoffel terms or, alternatively, derivations in a local tangent system—implementation choices with the same purpose: to preserve equilibrium in the correct geometry. The literature shows that these precautions reduce deviations from solid benchmark models and that residual errors shift to a percentage scale in the typical industry validity region (moderate thicknesses, non-extreme radii, regular lay-ups).

On an operational level, users of industrial FEM codes follow a well-established sequence. Shell analysis is performed with a calibrated mesh to capture curvatures and gradients; displacements, deformations/resultants, and average cuts are extracted; derivative-smoothing post-processing is applied, in singly or doubly curved versions depending on the geometry, imposing tensile boundary conditions on the faces and integrating the curvilinear equilibrium in thickness. When the component has “extreme” regions (very small radius, increasing thicknesses, strong discontinuities), a global-local campaign is added or verified locally with a 3D solid;

experience shows that consistency between the three levels—shell, recovery, local verification—produces reliable ILTS maps without the prohibitive cost of 3D on the entire component.

For completeness, note that the entire framework is consistent with the fundamentals of layered plate/shell theories. The classical and first-order formulations with shear (CLT/FSDT) establish the global kinematics and results; the enhanced layerwise or higher-order methods provide high-fidelity references and, above all, inspire the "target" profiles used in smoothing to reconstruct σ_{zz}(z). From an educational point of view, recovery can be thought of as a three-dimensional "projection" consistent with the equilibrium and kinematics of the shell: in the plane, ESL quantities are used, through the thickness, integration and regularization are performed, and in curvature, the correct geometric terms are introduced. The contribution of work on curved shells—from singly curved modeling to doubly curved generalization—is precisely that of having made this projection robust and efficient for real geometries.

The figure 2.4 analyses the distribution of interlaminar stresses in the presence of a hole. The 'exact' curve represents a high-fidelity reference solution, while the 'coarse mesh' and 'refine mesh' curves show the impact of mesh resolution on the accuracy of ILTS reconstruction. This is a paradigmatic example of how the quality of the numerical field in the plane directly affects the recovery results, even before considering curvature.

Moreover, Fig. 2.4 illustrates the distribution of interlaminar shear stresses in a curved laminate, as obtained from refined finite element models and compared with analytical references. The results highlight how curvature amplifies the through-thickness stress field, producing non-negligible peaks even in regions far from boundaries. This behaviour is in sharp contrast with flat laminates, where interlaminar stresses are typically confined to localized boundary layers near free edges or geo-

metric discontinuities. The comparison underlines the need for recovery strategies specifically tailored to curved configurations, since shell-based FEM models alone are unable to capture these out-of-plane quantities with sufficient accuracy.

The graph reports the distribution of interlaminar shear stresses (τ), representative of the out-of-plane stress state in curved laminates. These stresses, although not directly provided by shell FEM formulations, are critical for predicting delamination initiation and growth.

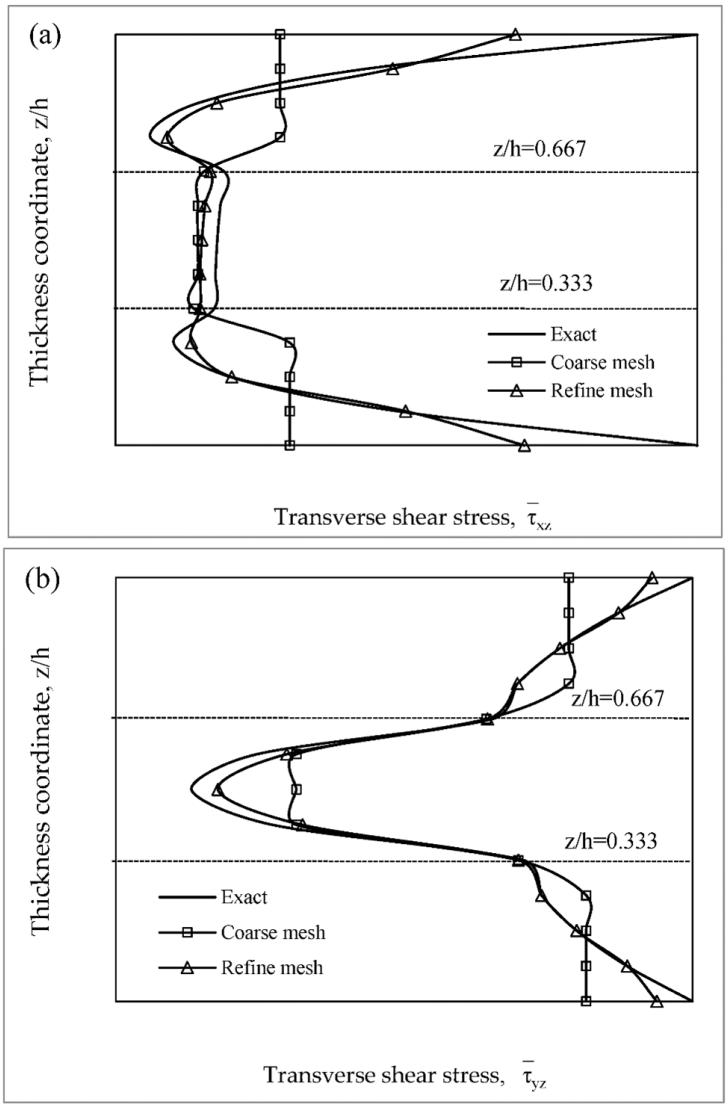

Figure 2.4: Nondimensionalized distribution of interlaminar shear stress (τ_{xz}) through the thickness of an open-hole laminate, comparing the "exact" solution with conforming meshes (coarse vs refined).

Fig. 2.5 shows the profile of interlaminar stress σ_{zz} near a free edge and along a specific interface in an angled laminate.

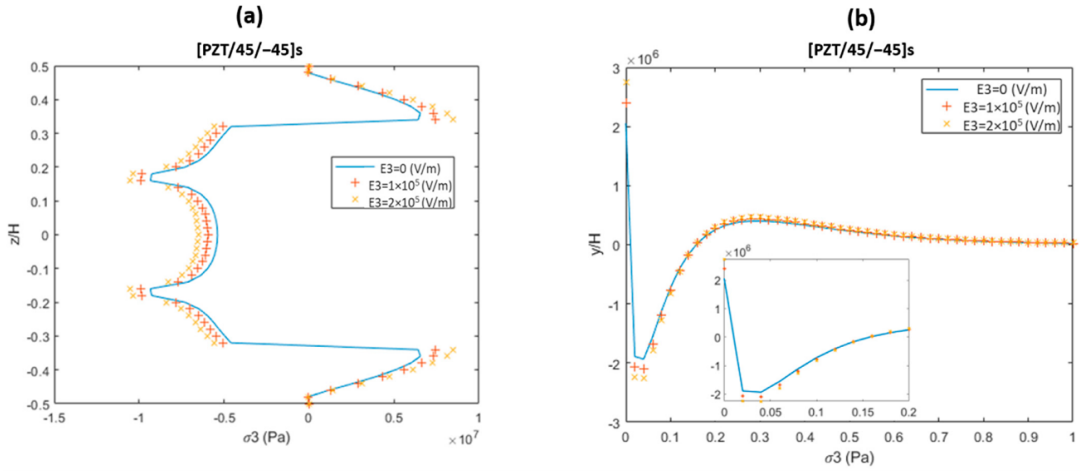

Figure 2.5: Distribution of the interlaminar normal stress σ_{zz} at the free edge and at the PZT/45 interface in an angle-ply laminate; development of series solutions.

2.4.1 Comparative summary of ILTS recovery methods

In the literature, several strategies have been proposed to recover interlaminar tensile stresses (ILTS) from shell-based finite element models. Although their underlying principles differ, they all aim at bridging the gap between the efficiency of equivalent single layer models and the need for accurate through-thickness stress prediction. The most representative families of methods can be grouped into derivative-based procedures, smoothing/patch recovery approaches, enhanced equilibrium formulations, and global–local strategies. Each method presents specific strengths and weaknesses in terms of accuracy, computational demand, and applicability. Table 2.2 summarizes these aspects in a comparative form, providing a useful reference for selecting the most appropriate recovery strategy depending on the context.

Recovery method	**Accuracy**	**Computational cost**	**Main limitations**
Derivative-based	Moderate to high, depending on mesh quality	Low	Sensitive to numerical noise; poor performance near discontinuities and free edges
Smoothing / Patch recovery	Improved accuracy compared to pure derivatives; good representation of average profiles	Low to medium	Requires careful definition of smoothing domains; still limited near strong gradients
Enhanced formulations	High accuracy, especially in curved laminates; captures curvature and shear contributions consistently	Medium	More complex implementation; still dependent on shell kinematics and assumptions
Global–local approaches	Very high, close to 3D solid reference in critical regions	High (local refinement + coupling with global model)	Increased modeling effort; higher computational demand compared to pure shell recovery

Table 2.2: Comparative summary of ILTS recovery methods.

Chapter 3

Theoretical Background

3.1 Fundamentals of laminate theory

The theory of laminates arises from the need to model a layered set of thin orthotropic sheets as an equivalent continuum capable of reproducing, with engineering fidelity, the overall response in terms of forces, moments and deformations. In a classic flat laminate, each layer is assumed to be homogeneous and orthotropic in its own material reference system, while the overall laminate is obtained by stacking layers with different orientations with respect to the median plane. The key idea is to compress the three-dimensional complexity into a two-dimensional description in the median plane, introducing resultants (forces and moments per unit length) and linking them to the deformations and curvatures of the plane itself. Classical Laminate Theory (CLT), an evolution of Kirchhoff–Love plate theory, provides the most widely used framework: assuming flat sections that remain flat and negligible cross-section, the kinematics are reduced to displacements of the median plane and rotations associated with curvatures, and the statics are expressed in terms of constitutive relationships between resultants and generalised kinematic quantities. Reference texts such as Reddy[21] and Jones[22] have consolidated this formalisation

[21] Reddy, J. N. (2003). *Mechanics of laminated composite plates and shells: Theory and analysis* (2nd ed.).*Boca Raton, FL: CRC Press.*

[22] Jones, R. M. (2018). *Mechanics of composite materials* (2nd ed.).*Boca Raton, FL: CRC Press.*

and the standard notation of laminate stiffness matrices.

In CLT formalism, the membrane resultants $\mathbf{N} = \{N_{xx},\, N_{yy},\, N_{xy}\}^{\mathsf{T}}$ and the bending moments $\mathbf{M} = \{M_{xx},\, M_{yy},\, M_{xy}\}^{\mathsf{T}}$ are introduced, while the kinematics of the middle plane are described by the strains $\boldsymbol{\varepsilon}^0 = \{\varepsilon^0_{xx},\, \varepsilon^0_{yy},\, \gamma^0_{xy}\}^{\mathsf{T}}$ and the curvatures $\boldsymbol{\kappa} = \{\kappa_{xx},\, \kappa_{yy},\, \kappa_{xy}\}^{\mathsf{T}}$.

The constitutive relationship at the laminate level is written in compact form

$$\begin{bmatrix} \mathbf{N} \\ \mathbf{M} \end{bmatrix} = \begin{bmatrix} \mathbf{A} & \mathbf{B} \\ \mathbf{B} & \mathbf{D} \end{bmatrix} \begin{bmatrix} \boldsymbol{\varepsilon}^0 \\ \boldsymbol{\kappa} \end{bmatrix}$$

where $\mathbf{A}$ is the membrane stiffness matrix, $\mathbf{D}$ is the bending (flexural) stiffness matrix, and $\mathbf{B}$ is the membrane–bending coupling matrix (zero for symmetric stacks). The matrices $\mathbf{A}$, $\mathbf{B}$, and $\mathbf{D}$ are obtained by integrating through the thickness the reduced stiffnesses of each ply transformed to the global coordinate system. Denoting by $\overline{\mathbf{Q}}^{(k)}$ the transformed reduced-stiffness matrix of the k-th ply and by z_{k-1}, z_k its lower and upper thickness coordinates, the well-known triplet reads:

$$\mathbf{A} = \sum_k \overline{\mathbf{Q}}^{(k)} \big(z_k - z_{k-1}\big),$$

$$\mathbf{B} = \tfrac{1}{2} \sum_k \overline{\mathbf{Q}}^{(k)} \big(z_k^2 - z_{k-1}^2\big),$$

$$\mathbf{D} = \tfrac{1}{3} \sum_k \overline{\mathbf{Q}}^{(k)} \big(z_k^3 - z_{k-1}^3\big).$$

This construction makes it clear how the distribution of anisotropic properties throughout the thickness—through the orientations and thicknesses of the layers—determines the overall response of the laminate. The transformation of the in-plane stiffnesses of the individual layers from the local system (1–2) to the global system (x–y) maintains the orthotropic nature but rotates the principal directions, generating in-plane couplings and transferring them, via integration, to the A, B,

and D matrices. CLT, despite its simplicity, naturally explains phenomena such as membrane-bending coupling in asymmetric laminates, the equivalent stiffnesses of balanced or quasi-isotropic stacks, and the role of the layer sequence in the response to in-plane and bending actions.

The kinematics assumed by CLT derives from the hypothesis of fibres normal to the midplane that remain straight and normal after deformation. In coordinates (x, y, z), for small displacements, a typical pattern is

$$u(x, y, z) = u_0(x, y) - z\,\frac{\partial w}{\partial x},$$
$$v(x, y, z) = v_0(x, y) - z\,\frac{\partial w}{\partial y},$$
$$w(x, y, z) = w_0(x, y).$$

which leads to zero transverse shear strains γ_{xz}=γ_{yz}=0. This assumption is adequate for very thin plates, but tends to underestimate transverse strains and shear stresses when the h/L ratio is not negligible. For this reason, First-Order Shear Deformation Theory (FSDT) extensions and higher-order models consistently reintroduce the effect of shear in the thickness, often using shear correctors to ensure energy equivalence with three-dimensional behaviour. The classic contribution by Whitney–Pagano[23] on the role of shear deformations in anisotropic plates provides an essential theoretical reference and explains why, even at the plate level, the Kirchhoff–Love assumptions are too restrictive for orthotropic laminates of moderate thickness.

From an energy perspective, CLT is justified by imposing equilibrium and compatibility in a two-dimensional context, assuming that the energy associated with out-of-plane deformations is not significant: in practice, 3D reality is projected onto a midsurface model in which the primary variables are the deformations and cur-

[23]Whitney, J. M., & Pagano, N. J. (1970). *Shear deformation in heterogeneous anisotropic plates. Journal of Applied Mechanics*, 37(4), 1031–1036. https://doi.org/10.1115/1.3408654

vatures of the midplane. This allows for a huge reduction in degrees of freedom compared to three-dimensional discretisation, which is why shell or plate models are the industry standard for large composite structures. However, the price to pay is the absence, among the primary unknowns, of interlaminar stresses σ_{zz}, τ_{xz}, τ_{yz}, which become derived quantities. In areas with rapid gradients (free edges, discontinuities, holes) or in curved geometries, boundary layers are formed in which interlaminar stresses play a decisive role in damage mechanisms. Laminate theory provides the platform for correctly evaluating the overall results, but reliable estimation of out-of-plane stresses requires kinematic extensions (FSDT, higher-order theories, zig-zag) or post-processing techniques consistent with three-dimensional equilibrium. Carrera's systematic reviews[24] of multilayer and zig-zag theories provide a historical and comparative overview of these extensions, comparing Equivalent Single Layer (ESL) and Layerwise (LW) models, and discussing interlaminar stress continuity and thickness profile accuracy.

The construction of matrices **A**, **B**, and **D** is based on the transformation of the in-plane stiffnesses of a ply. In the local ply system, the in-plane stress–strain law is $\sigma_{12} = \mathbf{Q}\,\varepsilon_{12}$, where Q depends on the moduli E_1, E_2, G_{12} and on Poisson's ratio ν_{12}. By rotating the ply by an angle θ with respect to the global axes, the transformed matrix $\overline{Q}(\theta)$ is obtained via the standard transformation operator; using $\overline{Q}^{(k)}$ for each layer allows **A**, **B**, and **D** of the whole laminate to be computed. This procedure naturally captures the lay-up architecture: balanced sequences cancel spurious couplings and reduce **B**; quasi-isotropic sequences mimic an isotropic in-plane response even with anisotropic material at the ply scale. From an analytical viewpoint, CLT thus provides a map from the lay-up design to the global response, with minimal computational cost and a physical clarity that makes it the basis for any refinement—from FSDT to higher-order models to layerwise formulations that

[24]Carrera, E. (2003). *Historical review of zig-zag theories for multilayered plates and shells. Applied Mechanics Reviews*, 56(3), 287–308. `https://doi.org/10.1115/1.1557614`

assign kinematic variables per layer. The classic texts remain the most authoritative source for the full derivation and the discussion of validity limits.

Higher-order extensions modify the kinematics by allowing non-zero shear deformations and more realistic thickness profiles, thus better reproducing the stress distribution and ensuring the continuity of shear stresses between layers. Alternatively, layerwise approaches assign each layer its own kinematic variables, allowing direct reconstruction of the interlaminar fields already in the two-dimensional solution. The choice between ESL, higher-order and LW depends on the thickness/span ratio, the presence of local gradients and the objectives of the analysis; for thin structures and light loads, CLT remains adequate, while as thickness or curvature increases, shear effects and out-of-plane stresses require richer models. Carrera's reviews show, with examples and benchmarks, how the different families are positioned along a complexity vs. accuracy diagram, providing practical criteria for model selection depending on the problem.

Finally, an essential aspect is the link between theory and numerical implementation. Finite element formulations of plates/shells inherit the ABD structure and the assumed kinematics: the quality of the solution depends on the consistency between kinematic assumptions, interpolations and differential operators; problems known as shear locking or thickness locking arise when the discretisation does not respect the delicate relationships between deformations and results. The texts and reviews cited report procedures to avoid such numerical pathologies (e.g., selective reduction of integration or elements with enriched shape functions) and, above all, highlight how the estimation of interlaminar stresses—not being primary variables in ESL theories—requires specific attention during the design phase, both through theories with shear and through post-processing consistent with three-dimensional equilibrium. This point represents a natural bridge to the topics that will be developed in the following paragraphs, dedicated to the theory of interlaminar stresses in

the presence of curvature and the FEM implications.

3.2 Constitutive equations for orthotropic laminates

The constitutive description of orthotropic laminates forms the mathematical core of composite materials theory. Each elementary layer, when considered in a local reference system coinciding with the main fibre directions, can be assumed to be orthotropic and flat, i.e. characterised by two elastic moduli E_1 and E_2, a shear modulus G_{12} and a Poisson's ratio ν_{12}. In this system, the stress-strain relationship takes the form of a matrix[25]

$$\begin{bmatrix} \sigma_1 \\ \sigma_2 \\ \tau_{12} \end{bmatrix} = \begin{bmatrix} Q_{11} & Q_{12} & 0 \\ Q_{12} & Q_{22} & 0 \\ 0 & 0 & Q_{66} \end{bmatrix} \begin{bmatrix} \varepsilon_1 \\ \varepsilon_2 \\ \gamma_{12} \end{bmatrix}$$

where the coefficients Q_{ij} represent the reduced stiffness matrix of the orthotropic material. They depend on the elastic constants of the laminate through the following relationships:

$$Q_{11} = \frac{E_1}{1 - \nu_{12}\nu_{21}},$$

$$Q_{22} = \frac{E_2}{1 - \nu_{12}\nu_{21}},$$

$$Q_{12} = \frac{\nu_{12}E_2}{1 - \nu_{12}\nu_{21}},$$

$$Q_{66} = G_{12}.$$

It should be noted that elastic symmetry implies $\dfrac{\nu_{12}}{E_1} = \dfrac{\nu_{21}}{E_2}$.

When the laminate is rotated by an angle θ with respect to the global system (x, y), the strain and stress components must be transformed using the classical tensor transformation laws. The constitutive matrix thus becomes $\overline{\mathbf{Q}}(\theta)$, which also contains coupled off-diagonal terms, reflecting the loss of orthotropy with respect

[25]Reddy, J. N. (2003). *Mechanics of laminated composite plates and shells: Theory and analysis* (2nd ed.).*Boca Raton, FL: CRC Press.*

to the global axes. This procedure accounts for the effect of fiber orientation in computing the laminate-level stiffness matrices **A**, **B**, **D**, which are then obtained by integrating $\overline{\mathbf{Q}}$ through the thickness over all layers.

The correct definition of the constitutive equations for orthotropic laminates is fundamental to understanding how variations in orientation and sequence of the layers influence the equivalent stiffness of the structure. Furthermore, these formulations form the basis for extension to higher-order theories in order to capture non-negligible shear deformations or three-dimensional effects. The robustness of the orthotropic constitutive description is confirmed both by applications in the aeronautical and naval fields, where the prediction of stiffness and strength is crucial, and in research applications, where it serves as a reference for evaluating new multilayer or layerwise theories.[26]

3.3 Curved laminates and interlaminar stress theory

The analysis of curved laminates introduces a complexity that goes well beyond the classical theory of flat laminates, since geometric curvature directly influences stress distribution and damage mechanisms. In flat laminates, stresses can be separated into membrane and flexural components, with interlaminar stresses emerging mainly near free edges or discontinuities. In curved laminates, on the other hand, the geometry of the structure itself induces three-dimensional stress fields even under apparently simple loading conditions, accentuating the importance of out-of-plane stresses. In particular, interlaminar tensile stresses (ILTS) become critical quantities as they are concentrated in the connection regions or along the free edges, contributing significantly to the initiation of delamination and the progressive degradation of the mechanical properties of the component.

The theory of interlaminar stresses in curved laminates is based on the recognition that the assumptions of Classical Laminate Theory, which are effective in

[26] Jones, R. M. (2018). *Mechanics of composite materials* (2nd ed.).*Boca Raton, FL: CRC Press.*

flat cases, are no longer sufficient when curvature generates non-linear couplings between membrane and bending deformations. The geometric effect results in an amplification of normal and tangential stresses to the thickness, which cannot be neglected or represented as secondary derived quantities. The most advanced models have shown that curvature alters not only the amplitude of ILTS, but also their distribution along the thickness, with localised peaks that vary depending on the lamination sequence and constraint conditions.

Recent literature[27] has emphasised that these phenomena must be addressed using dedicated modelling and post-processing techniques. Specific studies have highlighted that curved laminates, unlike flat ones, are more sensitive to design parameters such as fibre orientation and layer thickness, factors that directly affect the stability of the structure and its long-term resistance. In this sense, the theory of interlaminar stresses in laminated shells provides the conceptual tools to explain the relationship between geometry, stratification and stress distribution, laying the foundations for more accurate and safer design strategies.

3.4 Membrane vs bending stresses

In composite laminates, distinguishing between membrane stresses and bending stresses is essential to understanding overall mechanical behaviour. Membrane stresses are those that develop when the laminate is subjected to in-plane loads, such as tension or compression, and tend to distribute deformations evenly throughout the thickness. In this condition, each layer contributes proportionally according to its orientation and orthotropic properties, determining the overall stiffness of the laminate. In contrast, bending stresses arise when the laminate is subjected to out-of-plane moments or loads that induce curvature. In this case, the distribution of stresses across the thickness becomes non-uniform and varies from layer to layer,

[27] Roos, R., Kress, G., & Ermanni, P. (2007). *A post-processing method for interlaminar normal stresses in doubly curved laminates. Composite Structures*, 81(3), 463–470. https://doi.org/10.1016/j.compstruct.2006.09.016

with the position and orientation of the fibres playing a decisive role.[28]

The difference between the two contributions is particularly evident in curved laminates, where the geometric curvature amplifies the coupling between membrane and bending. This means that even predominantly in-plane loads can generate bending stress components, and vice versa, emphasising the importance of correct theoretical modelling. This interaction explains why the distribution of stresses in laminated shells cannot be interpreted simply by separating the two effects, but requires an integrated approach capable of capturing the coupling phenomena. Furthermore, the presence of localised flexural stresses is often the cause of critical interlaminar stresses that lead to delamination phenomena, while membrane contributions determine the laminate's ability to withstand global loads without loss of stiffness.

A proper understanding of the balance between membrane and flexural stresses is therefore crucial during the design phase. A symmetrical lamination sequence reduces or eliminates unwanted coupling, ensuring a more predictable response, while asymmetrical laminations can be used strategically when particular deformability or strength characteristics are desired. In both cases, conceptual distinction and accurate evaluation of the two contributions remain essential to ensure reliable performance in aerospace and automotive applications, where composite laminates find their most critical uses.

3.5 Finite Element implications

The application of laminate theory within the finite element method has a number of practical implications that affect the accuracy and reliability of numerical analyses. The choice between shell elements and solid elements is crucial: the former guarantee computational efficiency and are widely used in industrial design, but do not directly

[28]Reddy, J. N. (2003). *Mechanics of laminated composite plates and shells: Theory and analysis* (2nd ed.).*Boca Raton, FL: CRC Press*.https://doi.org/10.1201/9781420040586

provide interlaminar stresses, which must be reconstructed through post-processing procedures. Solid elements, on the other hand, allow for a complete distribution of stresses across the thickness, but the computational cost limits their use to local portions of the structure.[29]

In curved laminates, these considerations become even more relevant, as curvature introduces couplings between membrane and flexural stresses that must be correctly represented by the chosen finite element. Inadequate modelling can lead to underestimation of out-of-plane stresses, with the consequent risk of not correctly predicting delamination phenomena. For this reason, hybrid approaches have been developed in recent years that combine global analysis with shells and local analysis with solid models, so as to balance efficiency and accuracy.

A further aspect concerns the numerical difficulties associated with the kinematic assumptions of shell theory, which can lead to shear locking or thickness locking phenomena. These problems have been addressed with the development of enriched elements and selective integration reduction techniques, which improve the representation of laminate behaviour without excessively increasing computational costs. Ultimately, the implications of the finite element method for composite laminates show that theory must always be translated into informed numerical practices in order to ensure robust results in the most complex applications.

3.5.1 Practical risks without ILTS recovery

A critical aspect to be emphasized is the practical risk of relying solely on shell results without performing a proper recovery of interlaminar tensile stresses. In curved laminates, especially in shells with small radii of curvature, the out-of-plane stresses predicted directly by shell elements can be significantly underestimated. Several studies have reported discrepancies in the order of 30–50% compared to

[29] Carrera, E., Cinefra, M., Petrolo, M., & Zappino, E. (2014). *Finite element analysis of structures through unified formulation.Chichester: Wiley.*https://doi.org/10.1002/9781118536646

reference 3D solid models, particularly in regions close to free edges, ply drops, or geometric discontinuities. Such an underestimation can lead to non-conservative design choices, as the actual interlaminar stresses may exceed the delamination threshold much earlier than predicted. The consequence is a premature onset of damage mechanisms such as crack initiation and delamination growth, which directly compromise structural integrity and service life. For this reason, incorporating ILTS recovery techniques into the finite element workflow is not merely a theoretical refinement, but a necessary step to ensure reliable and safe structural design in aerospace and automotive applications.

Chapter 4

Numerical Implementation

4.1 Scope, assumptions, and notation

This chapter presents the numerical strategy for the *recovery of Interlaminar Tensile Stresses (ILTS)* in curved laminated shells starting from shell-model results. The formulation follows the kinematics of laminated shells in curvilinear coordinates and classical orthotropic ply constitutive relations, consistently with Reddy (Chap. 8), providing the theoretical foundations developed with `Maxima` symbolic codes and the corresponding numerical implementation carried out using `Octave` software. For completeness and reproducibility, all the symbolic `Maxima` scripts are reported in Appendix A, while the full `Octave` implementations are collected in Appendix B at the end of the thesis.

The present approach can be interpreted as a shell-based formulation enriched with through-thickness kinematic corrections, bridging classical FSDT shell models and full three-dimensional descriptions for the purpose of interlaminar stress recovery.

Aim:

To set a coherent set of assumptions and symbols to (i) describe the laminated shell in the neighbourhood of the *midsurface*, (ii) introduce kinematic and constitutive quantities in a curvilinear system, and (iii) fix the notation used later for ILTS

post-processing.

Working assumptions

The analysis adopts the following standard hypotheses for linear laminated shells:

- **Mechanical regime:** small strains and small displacements (linear elasticity).
- **Shell kinematics:** regular midsurface parameterised by curvilinear coordinates; first-order transverse-shear shell kinematics (FSDT) consistent with Reddy, Chap. 8.
- **Material:** each ply is linearly orthotropic; the laminate is a stacking of plies with given thicknesses and orientations; extension–bending coupling ($B \neq 0$) is allowed.
- **Geometry:** singly or doubly curved surface with finite principal radii (the plate limit is obtained for $R_i \to \infty$).
- **Through-thickness boundary conditions:** free top and bottom surfaces, $\sigma_{zz} = \tau_{1z} = \tau_{2z} = 0$ at $z = \pm h/2$.
- **Scope of validity:** no damage/cohesive failure; no pre-existing delamination; ply–ply interfaces treated as perfect ties.

Notation and reference systems

As in the following Fig. 4.1, let $\mathcal{S}$ be the shell midsurface, parameterised by two curvilinear coordinates (ξ_1, ξ_2) chosen, without loss of generality, along the principal curvature directions. The through-thickness coordinate is z, measured along the normal to the midsurface, with $z = 0$ on the midsurface and $z \in [-h/2,\ h/2]$ at the outer faces of the laminate of total thickness h.

Let R_1 and R_2 denote the principal radii of curvature, and define

$$c_1 \;=\; \frac{1}{R_1}, \qquad c_2 \;=\; \frac{1}{R_2}$$

as the principal curvatures (signs follow the adopted convention). Kinematics and area/volume measures in curvilinear coordinates induce z-dependent metric factors which, for a shell with straight fibres through the thickness (principal curvatures constant along z), take the form

$$J(\xi_1, \xi_2, z) \;=\; (1 + z\, c_1)\,(1 + z\, c_2)\; a_1(\xi_1, \xi_2)\, a_2(\xi_1, \xi_2),$$

where $a_\alpha(\xi_1, \xi_2) = \|\mathbf{g}_\alpha(\xi_1, \xi_2)\|$ are the midsurface scale factors ($\mathbf{g}_\alpha$ are the covariant basis vectors on the surface). In particular, the volume element[30] is

$$dV \;=\; (1 + z\, c_1)\,(1 + z\, c_2)\; a_1 a_2\; d\xi_1\, d\xi_2\, dz. \tag{4.1}$$

In the local shell system we use indices $1, 2$ for the tangential directions (ξ_1, ξ_2) and index 3 for the through-thickness direction z. The 3D stress components are therefore

$$\sigma_{11},\ \sigma_{22},\ \sigma_{12} = \sigma_{21} \quad \text{(in-plane)}, \qquad \tau_{1z} = \sigma_{13},\ \tau_{2z} = \sigma_{23},\ \sigma_{zz} = \sigma_{33} \quad \text{(ILTS and ILSS)}.$$

In shell models, $\sigma_{11}, \sigma_{22}, \sigma_{12}$ are obtained indirectly via stress resultants N and M, whereas ILTS $(\sigma_{zz}, \tau_{1z}, \tau_{2z})$ are not primary outputs and will be recovered by post-processing through-thickness equilibrium (Sec. 4.2–4.3).

Plate limit:

For $c_1 = c_2 = 0$ (infinite radii), one has $J = (a_1 a_2)$ and the volume element (equation 4.4) reduces to the planar case; kinematic and constitutive relations collapse to

[30] For clarity in post-processing we will often use local patches with normalisation $a_1 = a_2 = 1$, leaving explicit only the factors $(1 + z\, c_1)(1 + z\, c_2)$ that carry the through-thickness dependence.

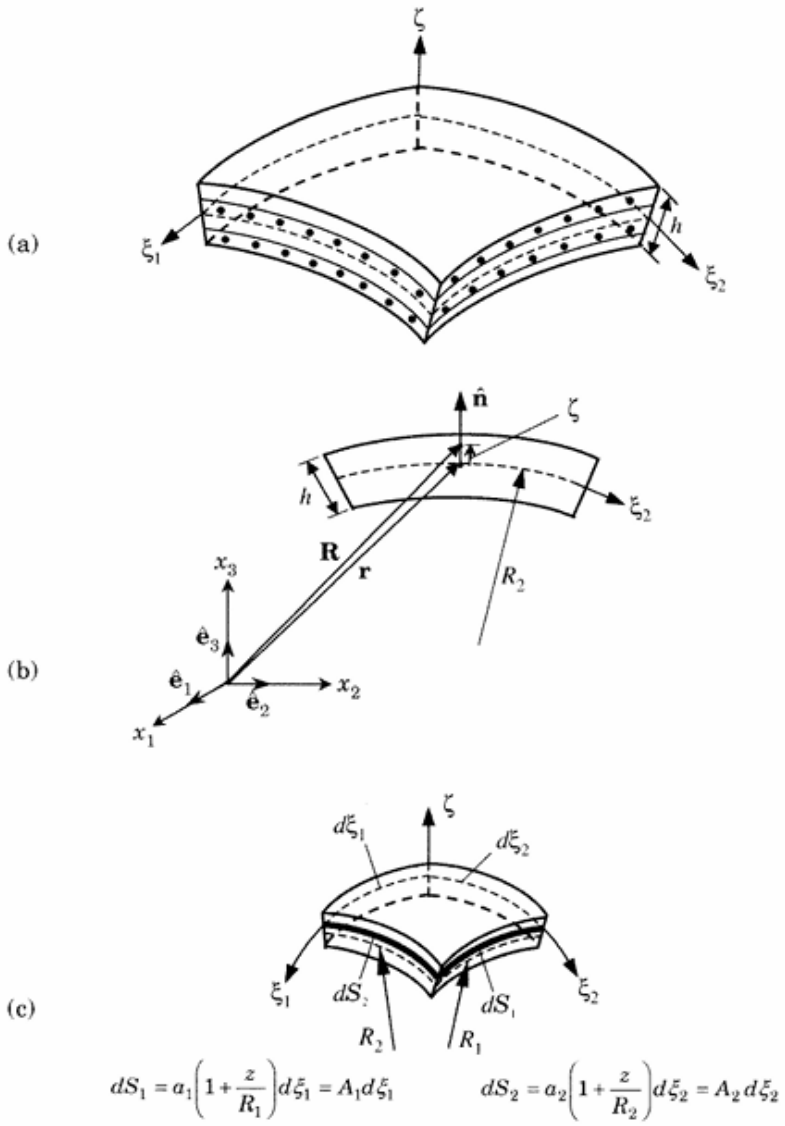

Figure 4.1: Geometry of a doubly-curved laminated shell. (a) Shell geometry. (b) Position vectors of points on the midsurface and above the midsurface. (c) A differential element of the shell (dS_1, dS_2 denote the arc lengths).

the corresponding plate relations, as expected.

Units: N–mm–MPa system for consistency with the FE models: elastic moduli in MPa, lengths in mm, forces in N. Conversions are indicated where needed.

Aspect	**Assumption / Note**
Mechanical regime	Linear elasticity; small displacements/strains.
Shell kinematics	FSDT on the midsurface; curvilinear coordinates aligned with principal directions.
Ply material	Linear orthotropy; stacking with ply thicknesses h_k and angles θ_k.
Geometry	Single or double curvature; finite R_1, R_2 (plate limit: $R_i \to \infty$).
Through-thickness BC	Free faces: $\sigma_{zz} = \tau_{1z} = \tau_{2z} = 0$ at $z = \pm h/2$.
Excluded phenomena	Damage, delamination, plasticity, non-perfect interfaces.

Table 4.1: Summary of assumptions.

Symbol	**Meaning**	**Units**
(ξ_1, ξ_2)	Curvilinear coordinates on the midsurface	mm
$z \in [-h/2,\, h/2]$	Through-thickness coordinate (normal to S)	mm
$R_1,\, R_2$	Principal radii of curvature	mm
$c_1,\, c_2$	Principal curvatures ($c_i = 1/R_i$)	mm^{-1}
$a_1,\, a_2$	Midsurface scale factors	–
$\mathrm{d}V$	Volume element $(1 + zc_1)(1 + zc_2)\, a_1 a_2\, \mathrm{d}\xi_1\, \mathrm{d}\xi_2\, \mathrm{d}z$	mm^3
$\sigma_{11},\, \sigma_{22},\, \sigma_{12}$	In-plane stresses (shell system)	MPa
$\tau_{1z},\, \tau_{2z},\, \sigma_{zz}$	ILTS (through-thickness)	MPa
h	Laminate thickness	mm

Table 4.2: Main notation and units (N–mm–MPa convention).

4.2 Theoretical and symbolic foundations

In this thesis the curvilinear-shell setting of Reddy (Chap. 8) is adopted and it is represented in Fig. 4.2.

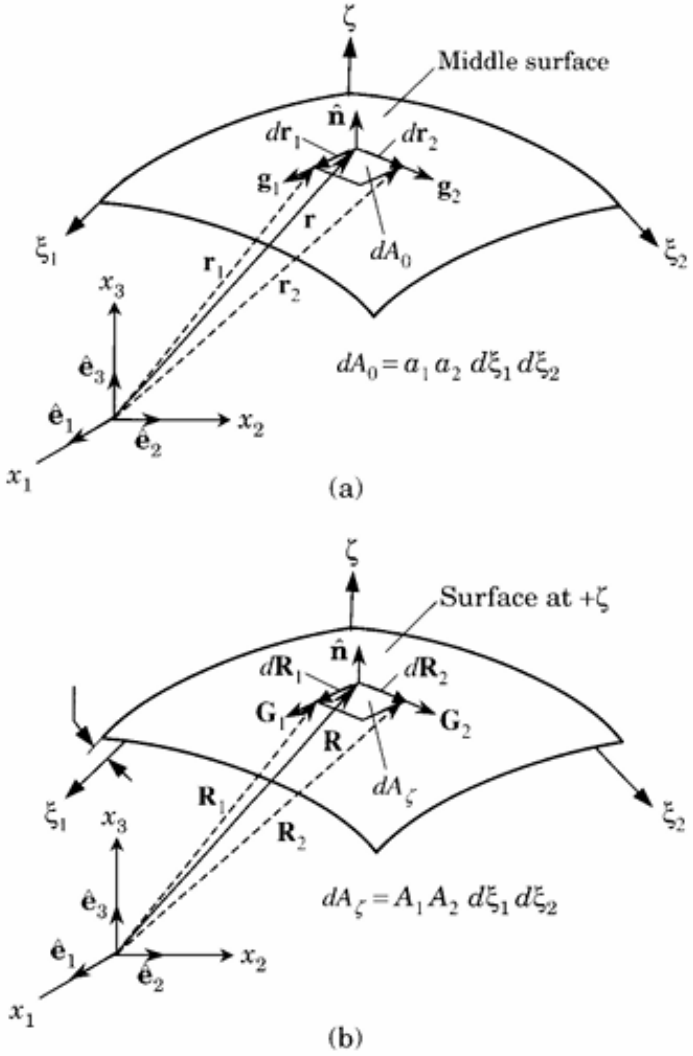

Figure 4.2: Surface area elements of a doubly-curved shell. (a) Area element on the midsurface. (b) Area element on a surface at $+\xi$.

The laminate is described in a neighbourhood of the midsurface $\mathcal{S}$ by two in-surface coordinates (ξ_1, ξ_2), chosen along principal curvature directions, and by the through-thickness coordinate z measured along the normal to $\mathcal{S}$. All metric identities

used later (Lamé coefficients and Jacobian) were also derived and checked in `Maxima`; see Appendix A1.

4.2.1 Local metric on a curved surface

Midsurface parametrisation and covariant bases.

Let the midsurface be parameterised by a smooth map

$$\mathbf{r}_0(\xi_1, \xi_2) \in \mathbb{R}^3, \qquad \mathbf{g}_\alpha = \frac{\partial \mathbf{r}_0}{\partial \xi_\alpha} \ (\alpha = 1, 2),$$

with $\mathbf{g}_\alpha$ the covariant basis vectors on $\mathcal{S}$. Their magnitudes

$$a_\alpha(\xi_1, \xi_2) = \|\mathbf{g}_\alpha(\xi_1, \xi_2)\|$$

are the midsurface scale factors (Lamé coefficients *on* $\mathcal{S}$); the unit tangents are $\mathbf{t}_\alpha = \mathbf{g}_\alpha / a_\alpha$ and the unit normal is

$$\mathbf{n} = \frac{\mathbf{g}_1 \times \mathbf{g}_2}{\|\mathbf{g}_1 \times \mathbf{g}_2\|}.$$

Since (ξ_1, ξ_2) are aligned with principal curvature lines, the midsurface metric is diagonal:

$$g_{\alpha\beta} = \mathbf{g}_\alpha \cdot \mathbf{g}_\beta = \begin{bmatrix} a_1^2 & 0 \\ 0 & a_2^2 \end{bmatrix}.$$

Offset surfaces and Lamé coefficients away from the midsurface (Reddy).

A point at distance z from $\mathcal{S}$ along the normal is

$$\mathbf{r}(\xi_1, \xi_2, z) = \mathbf{r}_0(\xi_1, \xi_2) + z\, \mathbf{n}(\xi_1, \xi_2).$$

Differentiating and using Weingarten relations along principal directions gives the covariant bases of the offset surface at z:

$$\mathbf{G}_1(z) = \frac{\partial \mathbf{r}}{\partial \xi_1} = (1 + z\, c_1)\, \mathbf{g}_1, \qquad \mathbf{G}_2(z) = \frac{\partial \mathbf{r}}{\partial \xi_2} = (1 + z\, c_2)\, \mathbf{g}_2,$$

with principal curvatures $c_\alpha = 1/R_\alpha$. Hence the Lamé coefficients at distance z are

$$A_1 = a_1\left(1 + \frac{z}{R_1}\right) = a_1(1 + z\, c_1), \qquad A_2 = a_2\left(1 + \frac{z}{R_2}\right) = a_2(1 + z\, c_2). \tag{4.2}$$

Area and volume elements.

The area of the surface at z and the shell volume element are

$$dA(z) = A_1 A_2\, d\xi_1\, d\xi_2, \tag{4.3}$$

$$dV = dA(z)\, dz = A_1 A_2\, d\xi_1\, d\xi_2\, dz. \tag{4.4}$$

Equivalently, using $c_\alpha = 1/R_\alpha$ and the midsurface factors a_α,

$$dV = (1 + z\, c_1)(1 + z\, c_2)\, a_1 a_2\, d\xi_1\, d\xi_2\, dz,$$

which is the exact form implemented in our through–thickness integration.

Arc-length coordinates (optional re-scaling).

Reparameterising the midsurface by arc-length,

$$s_1(\xi_1) = \int a_1\, d\xi_1, \qquad s_2(\xi_2) = \int a_2\, d\xi_2,$$

sets $ds_\alpha = a_\alpha\, d\xi_\alpha$; on small patches we use $a_1 = a_2 \simeq 1$ so that $A_\alpha \simeq 1 + z\, c_\alpha$ and the $(1 + z\, c_1)(1 + z\, c_2)$ dependence is explicit.

Maxima verification (what is proved in the script `riprovo_curvature.wxmx`).

On a local Monge patch

$$\mathbf{r}(u,v) = (u,\ v,\ z(u,v)), \qquad z(u,v) = A_{uu}u^2 + A_{uv}uv + A_{vv}v^2 + \mathcal{O}(\|(u,v)\|^3),$$

the in-plane axes is rotated by θ to the principal directions (mixed term $A'_{uv} = 0$) using

$$\tan 2\theta = \frac{2A_{uv}}{A_{uu} - A_{vv}}, \qquad c_1 = 2A'_{uu}, \quad c_2 = 2A'_{vv}.$$

The midsurface scale factors admit the second-order Taylor expansions at the base point

$$a_1(\chi_1,\chi_2) = 1 + \tfrac{1}{2}\big(2A_{uu}\chi_1 + A_{uv}\chi_2\big)^2 + \mathcal{O}(\|\boldsymbol{\chi}\|^3),$$
$$a_2(\chi_1,\chi_2) = 1 + \tfrac{1}{2}\big(A_{uv}\chi_1 + 2A_{vv}\chi_2\big)^2 + \mathcal{O}(\|\boldsymbol{\chi}\|^3),$$

so $a_1, a_2 = 1 + \mathcal{O}(\|\boldsymbol{\chi}\|^2)$ and the metric is locally diagonal at leading order. This justifies the arc–length normalisation on small patches and confirms that the Jacobian used in Reddy's measures is $A_1 A_2$.

Symbol	**Meaning**
$r_0(\xi_1,\xi_2)$	Midsurface parametrisation
$g_\alpha \ \ (\alpha = 1,2)$	Covariant bases on the midsurface: $g_\alpha = \dfrac{\partial r_0}{\partial \xi_\alpha}$
a_α	Midsurface Lamé (scale) factors: $a_\alpha = \|g_\alpha\|$
n	Unit normal to S: $n = \dfrac{g_1 \times g_2}{\|g_1 \times g_2\|}$
$R_\alpha,\ c_\alpha$	Principal radii and curvatures with $c_\alpha = 1/R_\alpha$
$G_\alpha(z)$	Covariant bases at distance z (offset surface)
A_α	Lamé coefficients at z (Reddy): $A_\alpha = a_\alpha(1 + z\,c_\alpha)$
$dA(z)$	Area element at z: $dA(z) = A_1 A_2\, d\xi_1\, d\xi_2$
dV	Shell volume element: $dV = A_1 A_2\, d\xi_1\, d\xi_2\, dz$

Table 4.3: Symbols used in §5.1.1.

4.2.2 Kinetics of the shell

Consider a laminated shell of uniform thickness h described by orthogonal curvilinear coordinates (ξ_1, ξ_2, ζ), with ξ_1, ξ_2 aligned with the principal curvature lines of the midsurface and $\zeta \in [-h/2, h/2]$ measured along the surface normal. The Lamé (scale) factors along the tangential directions are

$$A_1(\zeta) = a_1\big(1 + \zeta/R_1\big), \qquad A_2(\zeta) = a_2\big(1 + \zeta/R_2\big),$$

with R_α the principal radii; the area/volume elements are $dA = A_1 A_2\, d\xi_1 d\xi_2$ and $dV = A_1 A_2\, d\xi_1 d\xi_2\, d\zeta$.

The in-plane normal and shear *stress resultants* (Fig. 4.3) per unit length on the midsurface edges are defined by thickness integrals that include the geometric factors $(1 + \zeta/R_\alpha)$. In particular (notation $\sigma_1 = \sigma_{11}$, $\sigma_2 = \sigma_{22}$, $\tau_{12} = \sigma_{12}$, $\tau_{13} = \sigma_{13}$, $\tau_{23} = \sigma_{23}$),

$$N_{11} = \int_{-h/2}^{h/2} \sigma_{11}\Big(1 + \frac{\zeta}{R_2}\Big)\, d\zeta, \qquad M_{11} = \int_{-h/2}^{h/2} \sigma_{11}\Big(1 + \frac{\zeta}{R_2}\Big)\zeta\, d\zeta, \tag{4.5}$$

$$N_{22} = \int_{-h/2}^{h/2} \sigma_{22}\Big(1 + \frac{\zeta}{R_1}\Big)\, d\zeta, \qquad M_{22} = \int_{-h/2}^{h/2} \sigma_{22}\Big(1 + \frac{\zeta}{R_1}\Big)\zeta\, d\zeta, \tag{4.6}$$

$$N_{12} = \int_{-h/2}^{h/2} \tau_{12}\, d\zeta, \qquad M_{12} = \int_{-h/2}^{h/2} \tau_{12}\, \zeta\, d\zeta, \tag{4.7}$$

and the transverse shear resultants

$$Q_1 = K_s \int_{-h/2}^{h/2} \tau_{13}\Big(1 + \frac{\zeta}{R_2}\Big)\, d\zeta, \qquad Q_2 = K_s \int_{-h/2}^{h/2} \tau_{23}\Big(1 + \frac{\zeta}{R_1}\Big)\, d\zeta, \tag{4.8}$$

where K_s is the shear-correction factor.

For shallow shells one may take $\zeta/R_\alpha \to 0$, which yields $N_{12} = N_{21}$ and $M_{12} = M_{21}$ as in plate theory.

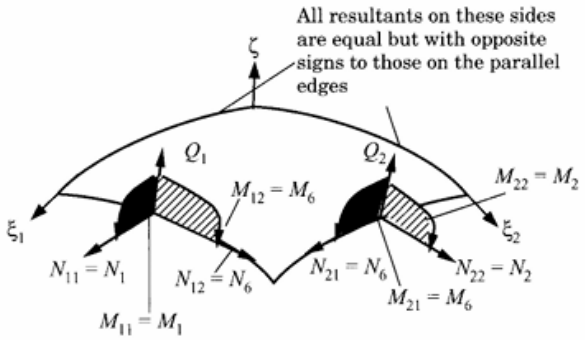

Figure 4.3: Stress resultants on a shell element.

4.2.3 Kinematics of the shell

Let $\mathbf{u} = (u_1, u_2, w)$ denote the displacement field along the local curvilinear directions (ξ_1, ξ_2, ζ), with $w = u_3$ the transverse deflection. The orthogonal curvilinear system has Lamé coefficients

$$A_1(\zeta) = a_1\Big(1 + \frac{\zeta}{R_1}\Big), \qquad A_2(\zeta) = a_2\Big(1 + \frac{\zeta}{R_2}\Big), \qquad A_3 = 1,$$

where R_α are the principal radii of curvature.

Strain components.

The linear normal and engineering shear strains in this system are

$$\varepsilon_{11}(\zeta) = \frac{1}{A_1}\frac{\partial u_1}{\partial \xi_1} + \frac{w}{R_1}, \tag{4.9}$$

$$\varepsilon_{22}(\zeta) = \frac{1}{A_2}\frac{\partial u_2}{\partial \xi_2} + \frac{w}{R_2}, \tag{4.10}$$

$$\gamma_{12}(\zeta) = \frac{1}{A_2}\frac{\partial u_1}{\partial \xi_2} + \frac{1}{A_1}\frac{\partial u_2}{\partial \xi_1}, \tag{4.11}$$

$$\gamma_{13}(\zeta) = \frac{1}{A_1}\frac{\partial w}{\partial \xi_1} + \frac{\partial u_1}{\partial \zeta}, \tag{4.12}$$

$$\gamma_{23}(\zeta) = \frac{1}{A_2}\frac{\partial w}{\partial \xi_2} + \frac{\partial u_2}{\partial \zeta}. \tag{4.13}$$

First–order shear deformation hypothesis.

Adopting the Reissner–Mindlin kinematics, the displacement field is written as

$$u_1(\xi_1, \xi_2, \zeta) = u_1^0(\xi_1, \xi_2) + \zeta\, \varphi_1(\xi_1, \xi_2),$$
$$u_2(\xi_1, \xi_2, \zeta) = u_2^0(\xi_1, \xi_2) + \zeta\, \varphi_2(\xi_1, \xi_2),$$
$$w(\xi_1, \xi_2, \zeta) = w^0(\xi_1, \xi_2),$$

where φ_α are the rotations of the transverse normal.

Substituting into the shear strains gives the compact and commonly used forms

$$\gamma_{13} = \frac{1}{A_1}\frac{\partial w^0}{\partial \xi_1} + \varphi_1, \tag{4.14}$$
$$\gamma_{23} = \frac{1}{A_2}\frac{\partial w^0}{\partial \xi_2} + \varphi_2. \tag{4.15}$$

Remarks.

Equations (4.14)–(4.15) make explicit that: (i) the transverse shear strains are directly expressed in terms of the midsurface deflection w^0 and the rotations φ_α; (ii) the geometric factors $1/A_\alpha = 1/[a_\alpha(1 + \zeta/R_\alpha)]$ introduce the curvature scaling through the thickness; (iii) for flat plates ($R_\alpha \to \infty$) one recovers the standard FSDT relations $\gamma_{13} = w_{,1} + \varphi_1$, $\gamma_{23} = w_{,2} + \varphi_2$.

4.2.4 Link between theory and the `Maxima` code

The symbolic implementation contained in `riprovo_formulazione.wxmx` (appendix A.2) operationalises the curvilinear shell relations presented above. The midsurface coordinates (ξ_1, ξ_2) are aligned with the principal curvature directions, and the through–thickness coordinate is denoted by ζ (measured along the normal). Away

from the midsurface, the Lamé factors are

$$A_1(\zeta) = a_1\left(1 + \frac{\zeta}{R_1}\right) = a_1(1 + \zeta\, c_1), \qquad A_2(\zeta) = a_2\left(1 + \frac{\zeta}{R_2}\right) = a_2(1 + \zeta\, c_2), \tag{4.16}$$

with $c_\alpha = 1/R_\alpha$. These factors appear explicitly in the code and produce the curvilinear weights $\left(1 + \zeta/R_\alpha\right)^{-1}$ in the pointwise strains, as dictated by the geometry.

Stress resultants and couples.

Following §8.2.2, the code defines the differential contributions to the in–plane forces, bending moments and transverse shears as

$$\begin{aligned}
&dN_{11} = \sigma_{11}\left(1 + \frac{\zeta}{R_2}\right)d\zeta, \quad dN_{22} = \sigma_{22}\left(1 + \frac{\zeta}{R_1}\right)d\zeta, \quad dN_{12} = dN_{21} = \sigma_{12}\, d\zeta,\\
&dM_{11} = \zeta\, dN_{11}, \qquad dM_{22} = \zeta\, dN_{22}, \qquad dM_{12} = dM_{21} = \zeta\, \sigma_{12}\, d\zeta,\\
&Q_1 = K_s \int \tau_{13}\left(1 + \frac{\zeta}{R_2}\right) d\zeta, \qquad Q_2 = K_s \int \tau_{23}\left(1 + \frac{\zeta}{R_1}\right) d\zeta,
\end{aligned}$$

where K_s is the shear–correction factor. In the file, these appear in the blocks `[dN11,dN22,dN12,dN21]`, `[dM11,dM22,dM12,dM21]` and `[Q1,Q2]`.

3D kinematics in principal coordinates.

Consistently with §8.2.3, the 3D linear kinematics is written by combining the plate variables (membrane, bending, and transverse shear), two local torsional (*drilling*) variables ψ_0, ψ_1, and three through–thickness corrective displacements $p(\zeta), q(\zeta), g(\zeta)$. These three functions are uniform in (ξ_1, ξ_2) and depend on ζ only; they enrich the out–of–plane field and enable a consistent recovery of interlaminar quantities in curved geometry.

$$\varepsilon = \{\varepsilon_{11}, \varepsilon_{22}, \varepsilon_{33}, \gamma_{2\zeta}, \gamma_{1\zeta}, \gamma_{12}\}^T, \qquad d = \{e_x, e_y, \gamma_{xy}, \kappa_x, \kappa_y, \kappa_{xy}, \gamma_{zx}, \gamma_{zy}, \psi_0, \psi_1, p, q, g, p', q', g'\}^T.$$

The code constructs the linear operator $\mathbf{L}_{\varepsilon\leftarrow d}(\zeta)$ such that

$$\varepsilon(\zeta) = \mathbf{L}_{\varepsilon\leftarrow d}(\zeta)\, d, \tag{4.17}$$

with the characteristic curvilinear denominators $1/(1+\zeta/R_\alpha)$ and the thickness derivatives $p'(\zeta), q'(\zeta), g'(\zeta)$ entering the shear and normal components. In explicit form, the six components used in the file read

$$\varepsilon_{11} = \frac{\varepsilon_{01} + \zeta\,\varepsilon_{11}}{1+\zeta/R_1}, \qquad \varepsilon_{22} = \frac{\varepsilon_{02} + \zeta\,\varepsilon_{12}}{1+\zeta/R_2}, \qquad \varepsilon_{33} = g'(\zeta),$$
$$\gamma_{2\zeta} = \frac{\omega_{01} + \zeta\,\omega_{11}}{1+\zeta/R_2} + q'(\zeta), \qquad \gamma_{1\zeta} = \frac{\omega_{02} + \zeta\,\omega_{12}}{1+\zeta/R_1} + p'(\zeta),$$
$$\gamma_{12} = \text{linear combination of } \gamma_{xy},\ \kappa_{xy} \text{ and rotations, with curvilinear weights,}$$

where $\varepsilon_{0\bullet}$, $\varepsilon_{1\bullet}$, $\omega_{0\bullet}$, $\omega_{1\bullet}$ are linear in $\{e_x, e_y, \gamma_{xy}, \kappa_x, \kappa_y, \kappa_{xy}, \gamma_{zx}, \gamma_{zy}, \psi_0, \psi_1\}$ and are obtained in the code via `linsolve` (block "displacements/rotations").

Constitutive law and symbolic operator.

Using `coefmatrix`/`augcoefmatrix`, the file assembles $\mathbf{L}_{\varepsilon\leftarrow d}(\zeta)$. For each lamina k, the orthotropic Hooke matrix $\mathbf{D}^{(k)}$ (rotated to the ply axes) yields

$$\sigma^{(k)}(\zeta) = \mathbf{D}^{(k)}\,\varepsilon^{(k)}(\zeta) = \mathbf{D}^{(k)}\,\mathbf{L}^{(k)}_{\varepsilon\leftarrow d}(\zeta)\, d, \tag{4.18}$$

and the resultants are obtained by integrating through the thickness with the curvilinear weights of §8.2.2.

Zero–energy modes.

Setting $c_1 = c_2 = 0$ and using `coefmatrix` produces the linear system associated with Reddy's energetic condition. The solution highlights the null–energy subspace (rigid–body plus *drilling* modes), which is subsequently exploited in the static condensation/reduction.

1D through–thickness discretisation.

For numerical integration, p, q, g are approximated in each sublayer by a two–node 1D element in ζ:

$$\zeta(\xi) = \frac{\zeta_a(1-\xi) + \zeta_b(1+\xi)}{2}, \quad p(\zeta) = N_a(\xi)p_a + N_b(\xi)p_b, \quad p'(\zeta) = \frac{p_b - p_a}{\zeta_b - \zeta_a},$$

with $N_a = (1-\xi)/2$, $N_b = (1+\xi)/2$ (analogously for q and g). Substitution into (4.17) and recomputation of `coefmatrix` deliver the discretised operator used in quadrature.

Operational summary.

The `Maxima` file provides: (i) the symbolic operator $\mathbf{L}_{\varepsilon \leftarrow d}(\zeta)$ consistent with Reddy's curvilinear kinematics; (ii) the through–thickness integration formulas for the resultants with the correct geometrical weights; (iii) the identification of the energetic kernel; and (iv) the 1D discretisation in ζ for the corrective functions. These components are then translated to the numerical code (Octave) to build the **DL** products, integrate over plies and quadrature points, and recover the ILTS in post–processing at a computational cost much lower than full 3D models

4.2.5 Laminate constitutive relations

In laminated shells, the constitutive relations must be derived by combining the behavior of each lamina into equivalent stiffness matrices for the whole stacking sequence. Following Reddy, we assume a shell composed of N orthotropic laminae of uniform thickness. The k-th lamina is oriented at an angle θ_k with respect to the shell x-axis. The local lamina stiffnesses are first defined in the principal material coordinates and then transformed to the global shell coordinates.

Stress–strain relations for a lamina.

For the k-th orthotropic lamina under a state of plane stress, the constitutive relations in the shell coordinate system take the form

$$\begin{Bmatrix} \sigma_{xx} \\ \sigma_{yy} \\ \sigma_{zz} \\ \sigma_{yz} \\ \sigma_{xz} \\ \sigma_{xy} \end{Bmatrix} = \begin{bmatrix} Q_{11} & Q_{12} & 0 & 0 & Q_{16} & e_{31}H \\ Q_{12} & Q_{22} & 0 & 0 & Q_{26} & e_{32}H \\ 0 & 0 & Q_{33} & Q_{34} & 0 & e_{33}H \\ 0 & 0 & Q_{34} & Q_{44} & 0 & 0 \\ Q_{16} & Q_{26} & 0 & 0 & Q_{66} & e_{36}H \end{bmatrix} \begin{Bmatrix} \varepsilon_{xx} \\ \varepsilon_{yy} \\ \varepsilon_{zz} \\ \gamma_{yz} \\ \gamma_{xz} \\ \gamma_{xy} \end{Bmatrix}, \tag{4.19}$$

where Q_{ij} are the transformed reduced stiffnesses, e_{3i} are the electro- or magnetostrictive material coefficients, and H denotes the intensity of the electric or magnetic field when actuating/sensing layers are considered.

Transformation of stiffnesses.

The transformed coefficients Q_{ij} are related to the reduced stiffnesses in the principal material axes $(1, 2)$ of the lamina by the well-known transformation relations:

$$Q_{11} = Q_{11}^m \cos^4\theta + 2(Q_{12}^m + 2Q_{66}^m)\sin^2\theta\cos^2\theta + Q_{22}^m \sin^4\theta, \tag{4.20}$$

$$Q_{22} = Q_{11}^m \sin^4\theta + 2(Q_{12}^m + 2Q_{66}^m)\sin^2\theta\cos^2\theta + Q_{22}^m \cos^4\theta, \tag{4.21}$$

$$Q_{12} = (Q_{11}^m + Q_{22}^m - 4Q_{66}^m)\sin^2\theta\cos^2\theta + Q_{12}^m(\sin^4\theta + \cos^4\theta), \tag{4.22}$$

$$Q_{16} = (Q_{11}^m - Q_{12}^m - 2Q_{66}^m)\cos^3\theta\sin\theta + (Q_{12}^m - Q_{22}^m + 2Q_{66}^m)\sin^3\theta\cos\theta, \tag{4.23}$$

$$Q_{26} = (Q_{11}^m - Q_{12}^m - 2Q_{66}^m)\sin^3\theta\cos\theta + (Q_{12}^m - Q_{22}^m + 2Q_{66}^m)\cos^3\theta\sin\theta, \tag{4.24}$$

$$Q_{66} = (Q_{11}^m + Q_{22}^m - 2Q_{12}^m - 2Q_{66}^m)\sin^2\theta\cos^2\theta + Q_{66}^m(\sin^4\theta + \cos^4\theta). \tag{4.25}$$

Here, the superscript m refers to quantities in the lamina principal material coordinates. The explicit forms of Q_{ij}^m depend on the engineering constants E_1, E_2, G_{12}, and ν_{12}.

Remarks.

The laminate constitutive relations summarized above establish the direct link between lamina properties and global laminate stiffnesses. They form the basis for the governing equations of motion and stability analysis in laminated shells. The presence of piezoelectric or magnetostrictive layers modifies the coupling through the additional terms in Eq. (4.19), while thermal effects can be incorporated by extending the strain measures to include hygrothermal strains.

4.2.6 Equations of motion for doubly–curved shells

In this section we present the governing equations of motion for laminated doubly-curved shallow shells following the formulation of Reddy [**?**]. The derivation is obtained by simplifying the general three-dimensional description under the assumption of constant radii of curvature and neglecting higher-order terms of the type z/R. This allows the stress resultants to be expressed in a compact laminate form.

Constitutive relations.

For thin shallow shells, the in-plane force resultants $\{N\}$ and the bending moments $\{M\}$ are related to the corresponding strains by the standard laminate constitutive equations:

$$\begin{Bmatrix} \{N\} \\ \{M\} \end{Bmatrix} = \begin{bmatrix} [A] & [B] \\ [B] & [D] \end{bmatrix} \begin{Bmatrix} \{\varepsilon^0\} \\ \{\kappa\} \end{Bmatrix}, \qquad \{Q\} = [A^*]\{\gamma\}, \tag{4.26}$$

where $[A]$, $[B]$, and $[D]$ are the extensional, coupling, and bending stiffness matrices of the laminate, respectively, and $[A^*]$ represents the transverse shear stiffness. The strain vectors are composed of the mid-surface strains $\{\varepsilon^0\}$, the changes of curvature

$\{\kappa\}$, and the transverse shear strains $\{\gamma\}$.

The stiffness coefficients are obtained from the integration of the transformed reduced stiffnesses Q_{ij}^k of the individual laminae through the thickness:

$$A_{ij} = \sum_{k=1}^{N} Q_{ij}^{(k)} \, (z_k - z_{k-1}), \qquad i,j = 1,2,6, \tag{4.27}$$

$$B_{ij} = \tfrac{1}{2} \sum_{k=1}^{N} Q_{ij}^{(k)} \, (z_k^2 - z_{k-1}^2), \tag{4.28}$$

$$D_{ij} = \tfrac{1}{3} \sum_{k=1}^{N} Q_{ij}^{(k)} \, (z_k^3 - z_{k-1}^3). \tag{4.29}$$

Strain-displacement relations.

The in-plane strains of the mid-surface are given by

$$\{\varepsilon^0\}^T = \left\{ \begin{array}{ccc} \varepsilon_{xx}^0 & \varepsilon_{yy}^0 & \gamma_{xy}^0 \end{array} \right\} = \left\{ \begin{array}{ccc} u_{,x} & v_{,y} & u_{,y} + v_{,x} \end{array} \right\}, \tag{4.30}$$

while the changes in curvature read

$$\{\kappa\}^T = \left\{ \begin{array}{ccc} \kappa_{xx} & \kappa_{yy} & \kappa_{xy} \end{array} \right\} = \left\{ \begin{array}{ccc} -\theta_{x,x} & -\theta_{y,y} & -(\theta_{x,y} + \theta_{y,x}) \end{array} \right\}, \tag{4.31}$$

where (u, v, w) are the displacements of the mid-surface and (θ_x, θ_y) the rotations of the normal.

Equations of motion.

The equilibrium of a shell element yields the coupled system of partial differential equations for the unknown fields $u, v, w, \theta_x, \theta_y$. In Cartesian coordinates (x, y) the

equations can be expressed as:

$$\frac{\partial N_{xx}}{\partial x} + \frac{\partial N_{xy}}{\partial y} = \rho h\, \ddot{u}, \tag{4.32}$$

$$\frac{\partial N_{yy}}{\partial y} + \frac{\partial N_{xy}}{\partial x} = \rho h\, \ddot{v}, \tag{4.33}$$

$$\frac{\partial Q_x}{\partial x} + \frac{\partial Q_y}{\partial y} + q(x,y,t) = \rho h\, \ddot{w}, \tag{4.34}$$

$$\frac{\partial M_{xx}}{\partial x} + \frac{\partial M_{xy}}{\partial y} - Q_x = I\ddot{\theta}_x, \tag{4.35}$$

$$\frac{\partial M_{yy}}{\partial y} + \frac{\partial M_{xy}}{\partial x} - Q_y = I\ddot{\theta}_y, \tag{4.36}$$

where ρ is the mass density, h the thickness, $I = \rho h^3/12$ the rotary inertia per unit area, and $q(x, y, t)$ the distributed transverse load.

Remarks.

Equations (4.32)–(4.36) constitute the governing system of the first-order shear deformation shell theory specialized to doubly-curved laminated composites. They naturally reduce to the classical laminated plate theory (CLPT) if shear effects are neglected ($\gamma = 0$) and the radii of curvature are taken to be infinite ($1/R \to 0$). This framework provides the basis for both analytical and finite element formulations of shallow shell structures.

4.3 From symbolic formulation to numerical implementation

This chapter documents the transition from the symbolic shell formulation developed in `Maxima` to its complete numerical realisation in `Octave`, as implemented in the script `prova_reddy_FEM`. The purpose of this section is to present, in a unified and coherent manner, the full computational pipeline that enables the reconstruction of three–dimensional stress fields and the recovery of interlaminar stresses starting from shell–level kinematic quantities.

The numerical implementation strictly follows the symbolic derivation presented in Chapter 3. All kinematic, constitutive and energetic operators are implemented

in closed form, and no additional modelling assumptions are introduced. The only sources of approximation are associated with numerical integration through the thickness and with the regularisation of zero–energy modes inherent to shell kinematics.

4.3.1 General structure and laminate representation

All numerical quantities are stored in a single global data structure `o`, representing the curved laminated shell. The laminate is described through layerwise lists, possibly after subdivision into numerical sublayers:

$$\{h_k\}, \quad \{m_k\}, \quad \{\theta_k\}, \qquad z_0 = z_{\text{inf}}, \quad z_j = z_{j-1} + h_j, \quad j = 1, \ldots, n,$$

with $z_{\text{sup}} = z_n$.

Here, h_k denotes the thickness of the k-th layer or sublayer, m_k the associated material identifier, and θ_k the ply orientation angle with respect to the shell reference directions. All through–thickness coordinates are measured with respect to the reference position z_{inf}, which corresponds to the lower surface of the laminate.

For each material m, the full three–dimensional orthotropic constitutive matrix

$$\mathbf{D}^{(m)} \in \mathbb{R}^{6\times 6}$$

is stored in the array `o.Dlist(:,:,m)`. These matrices are constructed from engineering constants (E_i, ν_{ij}, G_{ij}) by inversion of the corresponding compliance matrix and represent the complete three–dimensional elastic response of each constituent. When ply orientations are present, the constitutive matrices are rotated into the shell reference frame, ensuring consistency between material anisotropy and shell kinematics.

The shell geometry is characterised by the principal curvatures c_1 and c_2, stored as `o.c1` and `o.c2`. These curvature parameters enter explicitly both the kinematic

relations and the energetic formulation and play a central role in the through–thickness integration measure.

4.3.2 Through–thickness integration and geometric measure

All layerwise quantities are integrated along the thickness using a one–point Gauss rule on the reference interval $\xi \in [-1, 1]$. For a layer spanning the physical interval $[z_a, z_b]$, the mapping between reference and physical coordinates is defined as

$$z(\xi) = \frac{z_a(1-\xi) + z_b(1+\xi)}{2}, \qquad dz = z_b - z_a.$$

The differential volume element follows directly from the curvilinear shell geometry derived symbolically:

$$dV = (1 + z\,c_1)(1 + z\,c_2)\,dz.$$

This geometric weight accounts for curvature effects and multiplies all layerwise contributions to the energetic matrices and stress resultants. Its explicit retention ensures that curvature–induced couplings are consistently preserved at the numerical level.

Normalised and physical through–thickness coordinates are stored during assembly and later employed for post–processing and graphical reconstruction of stress distributions.

4.3.3 Layerwise kinematic and constitutive operators

The symbolic strain–displacement relation derived in Chapter 3,

$$\boldsymbol{\varepsilon}(z) = \mathbf{L}_{\varepsilon \leftarrow d}(z)\,\mathbf{d},$$

is implemented numerically through the closed–form routine `L_epsi_dj_strato`. This routine returns the operator

$$\mathbf{L}_{\varepsilon \leftarrow d}(z) \in \mathbb{R}^{6 \times N_d},$$

which maps the global vector of generalised degrees of freedom $\mathbf{d}$ to the three–dimensional strain components at a given through–thickness position.

The operator includes membrane strains, bending curvatures, transverse shear terms, curvature–induced couplings and the corrective through–thickness fields introduced in the symbolic formulation. For each layer and integration point, the corresponding operator is stored explicitly, constituting the direct numerical counterpart of the symbolic expressions obtained in `Maxima`.

The constitutive relation is enforced through the linear elastic law

$$\boldsymbol{\sigma}(z) = \mathbf{D}^{(l)}\, \boldsymbol{\varepsilon}(z),$$

leading to the stress operator

$$\mathbf{L}_{\sigma \leftarrow d}(z) = \mathbf{D}^{(l)}\, \mathbf{L}_{\varepsilon \leftarrow d}(z).$$

This operator is likewise stored layerwise and later employed for stress reconstruction and post–processing.

4.3.4 Energetic formulation and global assembly

The elastic strain energy per unit midsurface area is expressed as

$$U(\mathbf{d}) = \frac{1}{2} \int \boldsymbol{\varepsilon}^T \mathbf{D} \boldsymbol{\varepsilon}\, dV = \frac{1}{2}\, \mathbf{d}^T \mathbf{H}_{U \leftarrow d}\, \mathbf{d}.$$

The energetic Hessian $\mathbf{H}_{U \leftarrow d}$ is assembled by summing all layerwise and through–

thickness contributions:

$$\mathbf{H}_{U\leftarrow d} = \sum_{l} \sum_{ip} \mathbf{L}^{T}_{\sigma\leftarrow d} \mathbf{L}_{\varepsilon\leftarrow d}\, dV.$$

In parallel, the linear map relating generalised degrees of freedom to stress resultants is accumulated, enabling direct stress evaluation once the full kinematic vector $\mathbf{d}$ is reconstructed.

Due to numerical round–off errors, the assembled energetic matrix may exhibit minor asymmetries. Symmetry is therefore enforced explicitly a posteriori by averaging the matrix with its transpose.

4.3.5 Kernel identification and regularisation

The energetic Hessian $\mathbf{H}_{U\leftarrow d}$ is singular by construction, owing to rigid–body–like mechanisms and drilling–type kinematic redundancies inherent to shell formulations.

Rather than enforcing analytical constraints on individual degrees of freedom, an automatic kernel identification strategy is adopted. The numerical nullspace of $\mathbf{H}_{U\leftarrow d}$ is extracted using the routine `tosymmpd`, which identifies zero–energy modes on the basis of the spectral properties of the matrix.

The extracted kernel is used to construct a compensated stiffness matrix

$$\mathbf{K} = \mathbf{H}_{U\leftarrow d} + \lambda_{\min}\, \mathbf{P}_{\ker},$$

where $\mathbf{P}_{\ker}$ denotes the projector onto the kernel and $\lambda_{\min}$ is a stabilising parameter derived from the smallest finite eigenvalue. The resulting matrix is symmetric positive definite and suitable for inversion and static condensation.

Residual checks of the form $\|\mathbf{H}_{U\leftarrow d}\mathbf{v}\|$ are used to verify that the extracted kernel vectors correspond to genuine zero–energy modes.

4.3.6 Static condensation and master variables

The vector of generalised degrees of freedom is partitioned as

$$\mathbf{d} = \begin{bmatrix} \mathbf{d}_c \\ \mathbf{d}_f \end{bmatrix},$$

where $\mathbf{d}_c$ denotes a set of physically meaningful master variables and $\mathbf{d}_f$ collects all remaining kinematic and corrective degrees of freedom.

In the present formulation, the master set is chosen as

$$\mathbf{d}_c \equiv \mathbf{m} = \{\varepsilon_{11}, \varepsilon_{22}, \gamma_{12}, \kappa_{11}, \kappa_{22}, \kappa_{12}\},$$

namely the membrane strains and changes of curvature of the shell midsurface. These quantities provide a compact and physically interpretable description of the global deformation state.

Assuming quasi–static equilibrium of the free degrees of freedom, the classical Guyan condensation yields

$$\mathbf{d}_f = -\mathbf{K}_{ff}^{-1}\mathbf{K}_{fc}\,\mathbf{d}_c,$$

leading to the affine reconstruction

$$\mathbf{d} = \mathbf{L}_{d\leftarrow m}\,\mathbf{m}.$$

The corresponding reduced stiffness matrix

$$\mathbf{K}^{(r)} = \mathbf{L}_{d\leftarrow m}^{T}\mathbf{H}_{U\leftarrow d}\mathbf{L}_{d\leftarrow m}$$

represents an equivalent laminate stiffness expressed in terms of the master variables, while fully retaining the influence of the three–dimensional through–thickness kinematics.

4.3.7 Field reconstruction and interlaminar stress recovery

Once the master vector $\mathbf{m}$ is prescribed, the complete set of generalised degrees of freedom is reconstructed as

$$\mathbf{d} = \mathbf{L}_{d\leftarrow m}\,\mathbf{m}.$$

The three–dimensional stress field is then obtained locally as

$$\boldsymbol{\sigma}(z) = \mathbf{L}_{\sigma\leftarrow d}(z)\,\mathbf{d}.$$

In particular, the transverse normal stress component $\sigma_{33}(z)$ is extracted directly from the reconstructed stress vector at each layer and through–thickness position. Unlike classical shell theories, where σ_{33} is identically zero or recovered indirectly from equilibrium equations, the present formulation retains ε_{33} as an explicit kinematic quantity. As a result, interlaminar stresses emerge naturally from the constitutive law and are consistent with the underlying shell kinematics, curvature effects and laminate stacking sequence.

4.3.8 Symbolic–to–numerical mapping

Table 4.4 summarises the correspondence between the symbolic formulation developed in `Maxima` and its numerical implementation in `Octave`. The purpose of this mapping is to make explicit how each theoretical quantity, operator and energetic contribution derived in closed form is translated into a concrete numerical construct within the computational pipeline.

The left column reports the main symbolic expressions introduced in the analytical derivation, including curvilinear geometric factors, layerwise strain–displacement relations, constitutive laws, energetic quantities and static condensation operators. The right column documents their exact numerical counterparts, expressed in terms of data structures, operators and assembly procedures adopted in the `Octave` im-

plementation.

This table highlights that the numerical formulation does not introduce any additional modelling assumptions with respect to the symbolic theory. All kinematic, constitutive and energetic operators are implemented in closed form and evaluated numerically only through through–thickness quadrature and kernel regularisation. In particular, curvature effects are retained explicitly via the geometric weight in the differential volume element, and interlaminar stress components are recovered directly from the three–dimensional constitutive response.

The mapping therefore provides a transparent link between theory and implementation and serves as a reference for interpreting the numerical results presented in the subsequent chapters, as well as for validating the consistency of the computational procedure with the underlying shell formulation.

Symbolic formulation (Maxima)	**Numerical implementation (Octave)**
Curvilinear Lamé factors $A_\alpha(\zeta) = a_\alpha(1+\zeta/R_\alpha)$	Implemented via the geometric weight $(1 + z\,c_\alpha)$ in the differential volume element; curvature parameters $c_\alpha = 1/R_\alpha$ stored as `o.c1`, `o.c2`.
Layerwise strains $\boldsymbol{\varepsilon} = \mathbf{L}_{\varepsilon\leftarrow d}(z)\,\mathbf{d}$	Closed–form operator `L_epsi_dj_strato(...)` assembled into `o.L_epsi_dg(:,:,l,ipk)` for each layer and integration point.
Constitutive law $\boldsymbol{\sigma} = \mathbf{D}\,\boldsymbol{\varepsilon}$	Stress operator `o.L_sigmai_dg(:,:,l,ipk) = o.Dlist(:,:,o.mlist(l)) * o.L_epsi_dg(:,:,l,ipk)`.
Differential volume element $dV = A_1 A_2\,dz$	Numerical weight `(1+z*c1)*(1+z*c2)*dz` with local normalisation $a_1 = a_2 = 1$.
Generalised resultants $s = \int \boldsymbol{\sigma}\,dV$	Accumulated linear map `o.L_si_dg += o.L_sigmai_dg * dV`.
Elastic energy $\frac{1}{2}\int \boldsymbol{\varepsilon}^T\mathbf{D}\boldsymbol{\varepsilon}\,dV$	Energetic Hessian assembled as `o.H_U_dg += L_sigma' * L_epsi * dV`, symmetrised a posteriori.
Nullspace of the energetic Hessian	Automatic kernel extraction via `[Kmat,kern,lmin] = tosymmpd(o.H_U_dg,...)`.
Static condensation (Guyan)	Partition of constrained and free DOFs; construction of the map `o.L_dg_dm` and reduced stiffness `o.rKmat = L_dg_dm' * H_U_dg * L_dg_dm`.
Stress reconstruction $\boldsymbol{\sigma}(z) = \mathbf{L}_{\sigma\leftarrow d}(z)\,\mathbf{d}$	Post–processing via `sig_vec = o.L_sigmai_dg(:,:,l,ipk) * dg`, with extraction of $\sigma_{33}(z)$.

Table 4.4: Mapping between symbolic quantities (`Maxima`) and numerical constructs (`Octave`).

4.3.9 Concluding remarks

This chapter has presented a fully consistent computational pipeline that connects symbolic shell theory to numerical implementation, energetic formulation, static condensation and three–dimensional stress reconstruction. All numerical operations represent direct counterparts of the symbolic expressions derived in `Maxima`, with no additional modelling assumptions introduced at the implementation level.

Details of the numerical implementation and selected code listings are reported in the appendices.

Codes summary

For clarity, the numerical pipeline relies on **three complementary codes**: two symbolic notebooks developed in `Maxima` (Appendix A) and one numerical script implemented in `Octave` (Appendix B). Their roles are distinct and non–overlapping.

`riprovo_curvature.wxmx` **(*Maxima*, geometry)** Derives and verifies the curvilinear shell geometry in the vicinity of the midsurface. This notebook establishes the Lamé coefficients, curvature–dependent area and volume measures, and geometric identities required for consistent through–thickness integration.

`riprovo_formulazione.wxmx` **(*Maxima*, kinematics and operators)** Constructs the symbolic strain–displacement operator $\mathbf{L}_{\varepsilon \leftarrow d}(z)$ for the shell model enriched with through–thickness corrective fields and drilling–related rotations. The notebook also derives the associated stress operators, energy density, and identifies the theoretical nullspace of the energetic formulation. The resulting closed–form expressions constitute the analytical backbone of the numerical implementation.

`prova_reddy_FEM.m` **(*Octave*, numerical implementation)** Implements the complete numerical pipeline: laminate definition and sublayering, construction of layerwise strain and stress operators, energetic assembly with curvilinear measures, automatic kernel extraction and regularisation, static condensation to a reduced set of master variables, and post–processing of three–dimensional stress fields. The script produces through–thickness reconstructions of interlaminar stresses and associated graphical outputs.

Together, the *Maxima* notebooks provide analytical validation and generate the closed–form operators, while the *Octave* script realises the full numerical workflow required for interlaminar stress recovery in curved laminated shells.

Chapter 5

Validation and Results

The objective of this chapter is twofold. First, it provides a rigorous validation of the interlaminar tensile stress (ILTS) recovery methodology developed in Chapter 4. Second, it presents and discusses the numerical results obtained for a set of representative reference configurations.

The validation is conceived not as a single comparison, but as a structured and progressive assessment carried out across different modelling levels, ranging from full three–dimensional solid finite element models to shell formulations. This strategy allows the proposed method to be evaluated both in terms of numerical accuracy and modelling consistency, ultimately demonstrating its applicability to shell–based analyses where interlaminar stresses are not directly available.

In particular, the proposed ILTS recovery procedure is validated by:

- direct comparison with three–dimensional solid finite element results, where interlaminar stresses are explicitly resolved;
- comparison with independent reference results available in the literature;
- application to shell finite element models, which represent the final target use case of the developed methodology.

This chapter therefore constitutes the link between the theoretical–numerical

framework introduced previously and its practical use for the recovery of interlaminar stresses in curved laminated structures.

5.1 Scope and validation strategy

The validation of an interlaminar stress recovery methodology poses specific challenges, since the quantities of interest are not primary variables of shell theories and cannot be obtained directly from shell finite element solutions. For this reason, a careful and multi–level validation strategy is required in order to assess both the correctness of the recovered stresses and the internal consistency of the proposed formulation.

The validation strategy adopted in this work is based on the concept of *increasing levels of modelling abstraction*. The same physical problem is analysed using different numerical models, each characterised by a different degree of kinematic and geometric detail. The recovered interlaminar stresses are then compared across these models, under equivalent loading and deformation conditions.

Rationale for validation.

The ILTS recovery method developed in Chapter 4 relies on:

- shell kinematics enriched with through–thickness corrective fields;
- energetic consistency and static condensation;
- post–processing reconstruction of three–dimensional stress components.

While this formulation is theoretically consistent, its numerical reliability must be demonstrated by comparison with reference solutions in which the interlaminar stresses are directly computed.

In particular, validation is required to verify that:

- the recovered transverse normal stress σ_{33} satisfies equilibrium through the thickness;

- the magnitude and distribution of ILTS are correctly reproduced;
- curvature effects and laminate heterogeneity are properly captured.

Need for multiple validation levels.

A single validation approach is not sufficient to fully assess the proposed method. Direct comparison with a three–dimensional finite element model provides a reliable reference, but does not guarantee generality. Conversely, validation against literature data ensures independence but may involve different geometries or modelling assumptions.

For this reason, the validation is carried out using three complementary tools:

- **3D solid finite element models (HEX elements):** these models resolve the full three–dimensional stress field and provide a direct reference for interlaminar stresses;
- **reference results from literature:** independent numerical studies are used to verify the correctness of the recovered stresses under different laminate configurations;
- **shell finite element models:** shell models represent the final application of the proposed method and allow its effectiveness to be assessed in a realistic engineering context, where ILTS are not directly available.

Progressive abstraction and consistency.

The validation is structured as a progressive transition from high–fidelity models to reduced–order formulations. In particular:

- the three–dimensional solid model is used to establish a reference interlaminar stress field;
- equivalent curvature measures are extracted from the 3D model and used as input (master variables) for the ILTS recovery procedure;

- shell models are loaded in an equivalent manner, and ILTS are recovered using the methodology developed in Chapter 4.

This approach allows the proposed method to be assessed not only in terms of numerical accuracy, but also in terms of its ability to consistently transfer information between different modelling frameworks.

Key validation principle.

In summary, the validation activity is organised as a progressive comparison across different modelling levels, ranging from full three–dimensional solid finite element analyses to shell formulations. This approach allows the proposed interlaminar stress recovery method to be assessed both in terms of numerical accuracy and modelling consistency, while clearly identifying its domain of applicability and its limitations.

The results presented in the following sections should therefore be interpreted within this hierarchical validation framework, where each modelling level provides complementary information on the behaviour of the recovered interlaminar stresses.

5.2 Reference three–dimensional finite element model

The validation of the proposed interlaminar stress recovery strategy is first carried out against a high-fidelity three-dimensional finite element model, which is assumed as the reference solution throughout this chapter. The use of a full three-dimensional solid formulation allows direct and unambiguous access to the through–thickness stress component σ_{33}, which is not available in classical shell formulations and therefore represents the most appropriate benchmark for validating the proposed ILTS recovery procedure.

The reference model is deliberately chosen to be geometrically curved, laminated through the thickness, and subjected to a pure bending state. This configuration is particularly demanding from the point of view of interlaminar stress recovery, since curvature effects, material anisotropy, and bending-induced stress gradients coexist and interact.

5.2.1 Geometry and coordinate system

The reference structure is a curved laminated beam with annular geometry, characterized by a circular cross-section and a finite angular opening. The geometry corresponds to a cylindrical ring segment with a missing portion, as illustrated in Fig. 5.1 and Fig. 5.2.

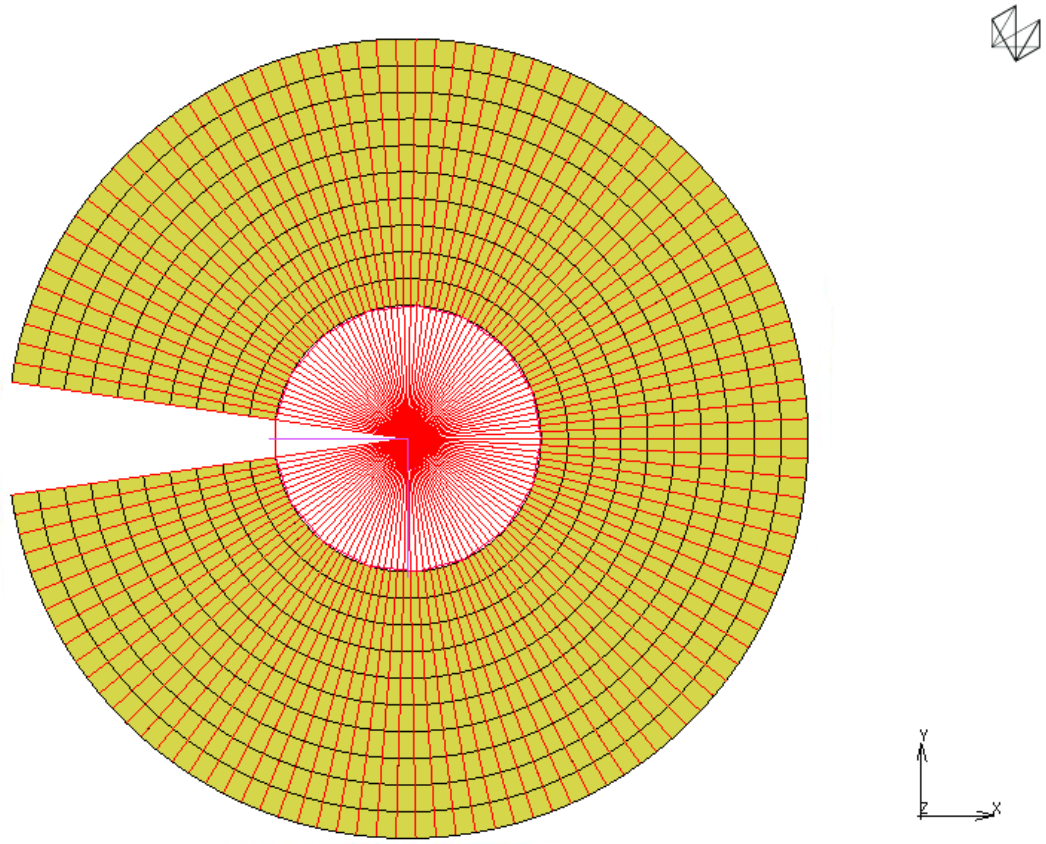

Figure 5.1: Lateral view of the annular beam showing the angular opening and the circumferential discretisation.

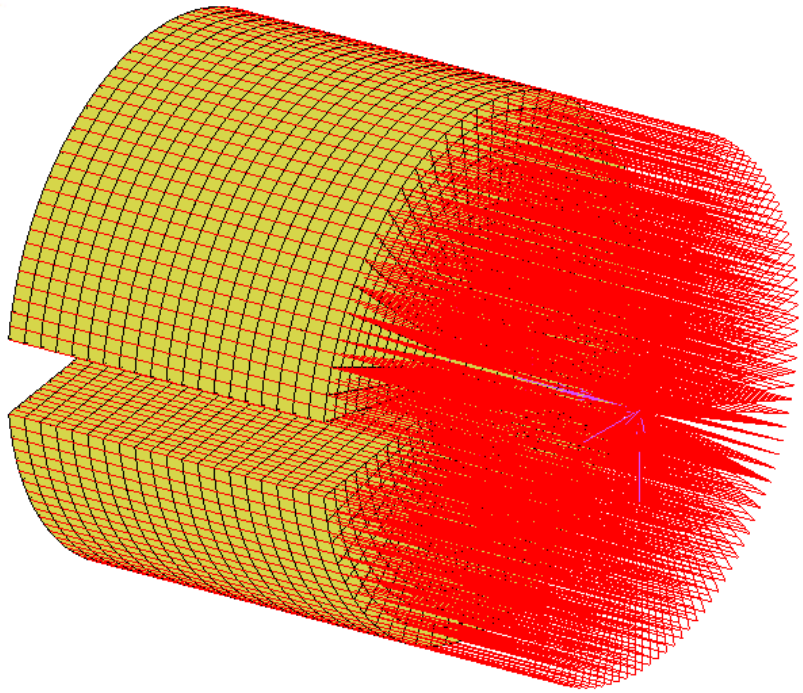

Figure 5.2: Isometric view of the 3D solid model highlighting the curved geometry and through–thickness mesh.

The geometric parameters are summarised as follows:

- inner radius: $r_i = 0.5$ mm,
- outer radius: $r_o = 1.5$ mm,
- radial thickness: $t = r_o - r_i = 1.0$ mm,
- axial length: $L = 2.0$ mm,
- angular opening: $\Delta\theta = 0.283191$ rad.

The laminate is composed of $N = 10$ layers of equal thickness, each ply having a thickness of 0.1 mm. The layers are stacked along the radial direction, which coincides with the through–thickness direction of the equivalent shell model. This choice ensures direct correspondence between the layerwise stress distributions obtained from the 3D model and those reconstructed by the shell-based ILTS recovery procedure.

A global Cartesian coordinate system is adopted with the following physical interpretation. The global coordinate system is defined as follows:

- the global y–axis coincides with the *circumferential* direction of the ring, i.e. tangent to the circular midline, and is identified with direction 2;
- the global z–axis corresponds to the *axial* direction of the beam, i.e. the direction parallel to the cylinder axis, and is identified with direction 1 of the shell model;
- the global x–axis represents the *radial* direction, normal to the midsurface and pointing through the laminate thickness, and is identified with direction 3, along which interlaminar stresses are evaluated.

With this convention, the transverse normal stress component extracted from the 3D solid model, σ_{xx}, corresponds to the radial stress component and is therefore directly comparable with the σ_{33} component recovered by the shell-based formulation developed in Chapter 4.

5.2.2 Material configurations

Four different material configurations are considered in order to assess the robustness and generality of the proposed ILTS recovery method.

Isotropic aluminium laminate.

In the first configuration, all layers are assigned an isotropic aluminium material with identical properties and zero orientation angle. The material behaviour is linear elastic, characterised by Young's modulus $E = 70\,000$ MPa and Poisson's ratio $\nu = 0.3$.

This configuration provides a baseline validation case, in which material anisotropy and coupling effects are absent. As a result, the interlaminar stress distribution is

governed primarily by geometric curvature and bending effects, allowing a clear assessment of the consistency of the recovery procedure in a relatively simple setting.

Composite CFRP laminate.

In the second configuration, the structure consists of a laminated carbon fibre reinforced polymer (CFRP) composite made of orthotropic plies. The stacking sequence, defined starting from the innermost layer, is

$$[0-90/0-90/\pm 45/\pm 45/0-90/0-90/\pm 45/\pm 45/0-90/0-90]$$

which is practically symmetric with respect to the laminate mid–thickness.

Each ply is modelled as a linearly elastic orthotropic lamina. The elastic properties adopted for the CFRP material correspond to those implemented in the finite element model and are representative of a quasi–isotropic carbon/epoxy laminate commonly used in structural applications. The material parameters are defined as:

$$\begin{aligned} E_1 &= E_2 = 70\,000 \text{ MPa}, \\ E_3 &= 15\,000 \text{ MPa}, \\ \nu_{12} &= 0.28, \qquad \nu_{23} = 0.30, \qquad \nu_{31} = 0.28, \\ G_{12} &= 27\,000 \text{ MPa}, \\ G_{23} &= 6\,000 \text{ MPa}, \\ G_{31} &= 6\,000 \text{ MPa}. \end{aligned}$$

The orthotropic material axes of each ply are rotated according to the prescribed orientation angle with respect to the global shell reference system. As a consequence, the laminate response results from the combined effect of ply orthotropy and stacking sequence.

Although each individual ply is orthotropic, the selected symmetric layup leads to an approximately quasi–isotropic in–plane structural behaviour. Nevertheless,

the through–thickness stress state remains strongly affected by the local anisotropy of the plies and by the stiffness mismatch between layers with different orientations.

Compared to the isotropic aluminium case, this configuration introduces additional complexity in the interlaminar stress field. In particular, the recovery of the transverse normal stress σ_{33} is influenced by orientation–dependent bending stiffness and nonuniform strain distributions across the thickness.

For these reasons, the present CFRP laminate represents a more challenging and physically realistic validation case for the proposed interlaminar stress recovery method, allowing its effectiveness to be assessed beyond the isotropic material assumption.

Aluminium–foam–aluminium sandwich laminate.

In the third configuration, a sandwich–type laminate is considered in order to investigate the performance of the recovery method in the presence of strong stiffness contrasts across the thickness. The outermost layers (layers 1 and 10) are modelled as isotropic aluminium skins, with material properties identical to those adopted in the aluminium configuration described above.

The internal layers are instead assigned a low–stiffness polyurethane foam material, representative of structural core materials commonly used in lightweight sandwich constructions. The foam is modelled as a linear elastic isotropic material, characterised by a Young's modulus $E = 50$ MPa and Poisson's ratio $\nu = 0.3$, as implemented in the finite element model.

This configuration introduces a pronounced stiffness discontinuity between the aluminium skins and the compliant core. As a result, bending deformation is primarily carried by the outer aluminium layers, while the foam core mainly contributes to shear transfer and thickness stability.

From the point of view of interlaminar stress recovery, this represents a highly demanding test case, as the transverse normal stress σ_{33} is strongly influenced by the mismatch in elastic properties between adjacent layers. The ability of the proposed

method to accurately capture stress peaks at the skin–core interfaces is therefore critically assessed through this configuration.

Foam–aluminium–foam laminate.

A fourth configuration is also analysed, consisting of a laminate in which the material distribution is intentionally inverted with respect to conventional sandwich design. In this case, the innermost layers (layers 5 and 6) are assigned the isotropic aluminium material, while the outer layers (layers 1–4 and 7–10) are modelled using the same polyurethane foam described above.

Although such a configuration has limited practical relevance from a structural design perspective, it provides a valuable numerical test case for the recovery framework. In particular, it allows the sensitivity of the method to the location of stiff and compliant layers to be investigated in a controlled manner.

The presence of stiff metallic layers embedded within a compliant matrix leads to a markedly different curvature and stress distribution compared to classical sandwich layouts. This configuration therefore serves as a stress–reversal and robustness test, highlighting the capability of the proposed recovery procedure to handle unconventional stiffness distributions without introducing numerical artefacts or loss of accuracy.

Together with the previous material configurations, this case further demonstrates the generality of the proposed ILTS recovery method and its applicability to a wide range of layered structural concepts, including both conventional and nonstandard laminate architectures.

5.2.3 Finite element discretisation

The reference model is discretised using second-order hexahedral solid elements (HEX20). Each element is characterised by 20 nodes and quadratic interpolation of the displacement field, which allows accurate representation of bending deformation modes and through–thickness stress gradients. Each node possesses three transla-

tional degrees of freedom (u_x, u_y, u_z), resulting in a total of 60 degrees of freedom per element.

The mesh is structured in the radial, circumferential, and axial directions, with a layerwise discretisation that ensures at least one solid element per ply through the thickness. This choice enables direct evaluation of stress components at each ply interface and ensures sufficient resolution of the interlaminar stress field.

The adoption of higher-order solid elements is essential for the present validation, as first-order elements would lead to poor representation of bending-induced stress gradients and reduced accuracy in the evaluation of σ_{33}. Mesh convergence studies were performed to verify that the extracted through–thickness stress profiles are insensitive to further refinement, confirming the adequacy of the adopted discretisation.

5.2.4 Multi-point constraints and periodicity treatment

The model includes rigid multi-point constraint elements (RBE2), visible as radial constraint links converging towards a central master node. These elements enforce kinematic coupling among selected nodes and play a crucial role in the correct transmission of bending actions across the curved geometry.

From a numerical standpoint, the RBE2 constraints ensure:

- uniform distribution of the applied bending moment,
- suppression of spurious rigid-body modes,
- consistent deformation of the curved cross-section.

From a physical perspective, the use of RBE2 elements can be interpreted as a way to emulate the behaviour of a periodic segment extracted from a complete circular ring. This approach allows the local stress state within the analysed segment to be representative of a continuously curved structure, while avoiding the computational cost associated with modelling the full ring.

5.2.5 Loading conditions: butterfly bending load

A pure bending state is induced by applying a distributed load on the two faces delimiting the angular opening of the ring segment. The load is defined as a spatially varying pressure, commonly referred to as a *butterfly* bending load.

The conceptual meaning of the butterfly bending load is to reproduce a pure bending state by imposing opposite bending moments at the two ends of the angular opening, with a continuous and linear transition between them. The antisymmetric distribution of the applied pressure generates equal and opposite bending actions, resulting in zero bending moment at the mid–span and no net axial force or transverse shear.

The conceptual definition of the butterfly bending scheme and its numerical implementation in the present study are illustrated in Fig. 5.3.

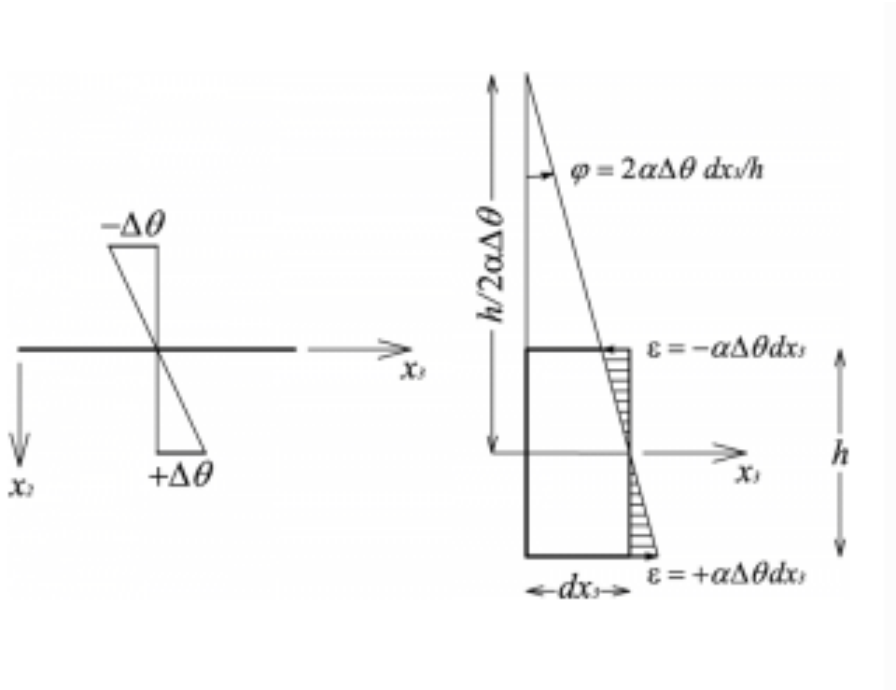

Figure 5.3: Conceptual representation of a butterfly bending load imposed through antisymmetric end rotations, leading to a pure bending state with constant curvature and a linear axial strain distribution across the thickness.

The pressure distribution is prescribed through a tabulated field according to

the relation

$$p(v_1, v_2) = p_0 \left(\sqrt{v_1^2 + v_2^2} - 1\right) 2,$$

where v_1 and v_2 are local in–plane coordinates on the loaded faces and $p_0 = 1000$ is the reference load magnitude.

This loading scheme generates a linearly varying bending moment along the circumferential direction, characterised by:

- a positive bending moment of $+1000$ at one end of the opening,
- a negative bending moment of -1000 at the opposite end,
- zero bending moment at the mid–span of the ring segment.

As a result, the structure is subjected to a purely flexural deformation, with no net axial force or transverse shear. This loading condition is particularly suitable for the present study, as it isolates bending–induced curvature effects and allows the resulting interlaminar stresses to be directly related to the applied bending moment.

5.2.6 Available outputs and reference quantities

The 3D solid formulation provides direct access to:

- the full three-dimensional strain field,
- the transverse normal stress component σ_{33} across the laminate thickness,
- stress distributions at individual ply interfaces.

In particular, the through–thickness stress component σ_{33} extracted from this model is adopted as the reference interlaminar stress distribution. All subsequent validation activities presented in this chapter are based on direct comparison between this reference solution and the stresses recovered using the shell-based approach developed in Chapter 4.

5.3 Extraction of master variables from the 3D model

This section describes the procedure adopted to extract the master variables required by the interlaminar stress recovery method from the reference three–dimensional finite element model.

As discussed in Chapter 4, the post–processing formulation requires as input a set of six master variables,

$$\{\varepsilon_{11}, \varepsilon_{22}, \gamma_{12}, \kappa_{11}, \kappa_{22}, \kappa_{12}\},$$

together with the geometric and material data defining the laminate. These quantities are not imposed *a priori* in the present validation framework, but are instead obtained directly from finite element results.

In particular, both three–dimensional solid and two–dimensional shell finite element models provide access to in–plane strain fields from which the required master variables can be consistently reconstructed. Among them, the circumferential curvature κ_{22} plays a central role in the present study, as it governs the bending state responsible for the generation of interlaminar normal stresses.

For all validation tests reported in this chapter, the curvature κ_{22} is extracted from the three–dimensional strain field and used as input master variable for the ILTS recovery procedure described in Chapter 4.

5.3.1 Strain–based evaluation of curvature

The evaluation of the curvature κ_{22} is performed following a strain–based approach, relying on the circumferential strain component ε_{22} extracted at the inner and outer surfaces of the laminate.

For a curved beam or shell subjected to pure bending, the kinematic relation

between strain and curvature can be expressed, in its simplest form, as

$$\varepsilon_{22}(z) = \varepsilon_{22}^{0} + z\,\kappa_{22},$$

where z denotes the through–thickness coordinate measured from a reference surface and ε_{22}^{0} is the membrane strain component.

Under the butterfly bending load described in Section 5.2.5, the resulting deformation state is dominated by bending effects, and the membrane contribution is negligible. As a consequence, the curvature can be directly estimated from the difference between the circumferential strains measured at the two laminate surfaces:

$$\kappa_{22} = \frac{\varepsilon_{22}^{\text{top}} - \varepsilon_{22}^{\text{bottom}}}{h},$$

where h is the total laminate thickness.

In the present work, the surface strains are extracted from the three–dimensional finite element model at:

- the innermost ply (layer 1), corresponding to the minimum radial coordinate and exhibiting the maximum compressive or tensile strain, and
- the outermost ply (layer 10), corresponding to the maximum radial coordinate and exhibiting the opposite extreme strain.

This choice ensures that the curvature evaluation fully captures the bending deformation across the entire laminate thickness and is consistent with classical curved beam kinematics.

5.3.2 Curvature Evaluation Based on the Winkler–Bach Approach (according to Strozzi)

For curved beams with finite thickness, a more refined interpretation of the strain–curvature relationship can be obtained by accounting for the actual geometry of the

cross–section. In particular, following the approach discussed by Strozzi, the bending curvature can be evaluated by relating the differential rotation of circumferential fibers to their corresponding arc lengths.

The kinematic interpretation underlying this procedure is illustrated in Fig. 5.4, where the differential rotation between circumferential fibers and the definition of the neutral radius are shown.

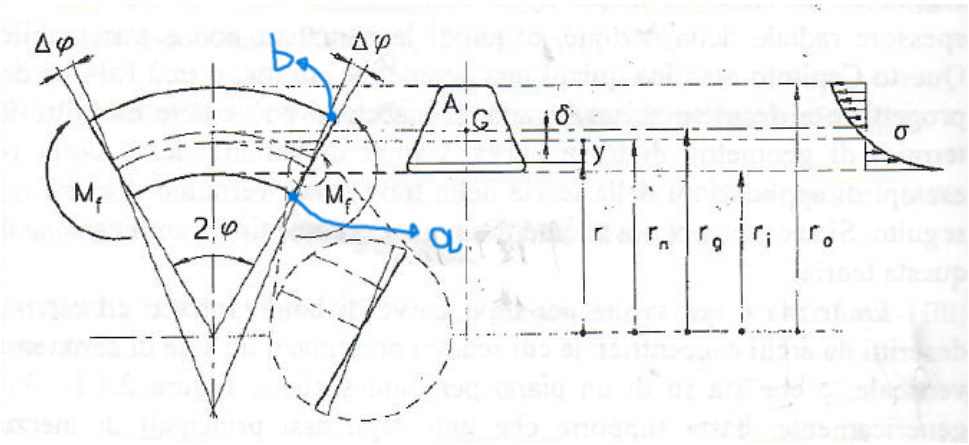

Figure 5.4: Kinematic interpretation of bending in a curved beam according to Strozzi's approach. The figure illustrates the differential rotation $\Delta\phi$ between inner and outer circumferential fibers, the definition of the neutral radius r_n, and the corresponding stress distribution across the thickness.

Let $\varepsilon_{22}^{\text{int}}$ and $\varepsilon_{22}^{\text{ext}}$ denote the circumferential strains measured at the inner and outer radii, r_{int} and r_{ext}, respectively. The corresponding fiber elongations over the angular span ϕ are given by

$$a = \varepsilon_{22}^{\text{int}}\, r_{\text{int}}\, \phi, \qquad b = \varepsilon_{22}^{\text{ext}}\, r_{\text{ext}}\, \phi.$$

The differential rotation between the two fibers is then expressed as

$$\Delta\phi = \frac{b - a}{t},$$

where $t = r_{\text{ext}} - r_{\text{int}}$ is the laminate thickness.

In accordance with curved beam theory, the neutral radius r_n is evaluated using

the Winkler–Bach relation,

$$r_n = \frac{r_{\text{ext}} - r_{\text{int}}}{\ln(r_{\text{ext}}/r_{\text{int}})}.$$

Finally, the resulting bending curvature is computed as

$$\kappa_{22} = \frac{\Delta\phi}{r_n\,\phi}.$$

This procedure has been implemented in a dedicated post–processing script, allowing κ_{22} to be consistently extracted from the three–dimensional finite element strain field for all validation cases.

5.3.3 Choice of reference radius for curvature evaluation

It is worth noting that the post–processing formulation described in Chapter 4 formally interprets the master curvature κ_{22} as defined at a reference surface associated with the shell midsurface, often approximated by the geometric mean radius.

In the present validation study, however, the curvature evaluated at the neutral radius r_n has been adopted as input for the ILTS recovery procedure. This choice has been guided by numerical evidence: when the curvature is computed at the neutral radius, the interlaminar normal stress profiles recovered by the proposed method exhibit an excellent agreement with the reference three–dimensional finite element results.

Conversely, the use of a curvature evaluated at the geometric mid–radius leads to noticeable discrepancies in the recovered σ_{33} distribution. This observation highlights the sensitivity of interlaminar stress recovery to the precise definition of the bending curvature in curved laminates and confirms the suitability of the neutral–axis–based evaluation for the present geometry.

The curvature κ_{22} extracted through this procedure is therefore used as master input variable in all subsequent validation analyses presented in this chapter.

The curvature κ_{22} obtained from the three–dimensional strain field thus pro-

vides the direct link between the reference FEM solution and the interlaminar stress recovery procedure described in Chapter 4.

5.4 Validation against 3D FEM interlaminar stresses

The validation of the proposed interlaminar stress recovery (ILTS) procedure is carried out by direct comparison with results obtained from the three–dimensional solid finite element model, which is assumed as reference solution.

The validation strategy follows a clear and unambiguous workflow:

- the master curvature component κ_{22} is extracted from the 3D FEM strain field, following the procedure described in Section 5.3.2;
- the extracted curvature is used as input to the ILTS recovery procedure developed in Chapter 4;
- the resulting through–thickness stress distribution $\sigma_{33}(z)$ is compared against the corresponding stress directly obtained from the 3D FEM model.

This approach allows the accuracy of the proposed method to be assessed independently of any shell formulation, since the comparison is performed against a full three–dimensional stress field.

Four validation cases are considered, characterised by progressively increasing material heterogeneity and structural complexity:

1. an isotropic aluminium laminate, used as baseline case;
2. a quasi–isotropic CFRP laminate with multiple ply orientations;
3. a classical sandwich laminate with stiff aluminium facesheets and a compliant polymeric core;
4. an anti–sandwich laminate, characterised by stiff aluminium layers located in the central region and compliant outer layers.

This selection allows the proposed recovery procedure to be assessed over a wide range of structural behaviours, from homogeneous bending–dominated configurations to highly heterogeneous laminates where strong three–dimensional effects may arise.

In the following, results for the isotropic aluminium configuration are presented and discussed first, followed by the CFRP, sandwich and anti–sandwich cases.

5.4.1 Isotropic aluminium laminate

The first validation case corresponds to the isotropic aluminium laminate described in Section 5.2.2. The material isotropy and uniform ply orientation provide a clean baseline for assessing the accuracy of the ILTS recovery method, without additional effects due to anisotropy or coupling.

From the 3D FEM simulation, the circumferential strain component ε_{22} is extracted at the innermost and outermost layers of the laminate. As expected under pure bending conditions, the maximum and minimum values of ε_{22} occur at the inner and outer surfaces, respectively.

In order to verify the consistency of the extracted strain field with curved beam theory, a *path plot* of the circumferential strain component ε_{22} along the thickness direction was generated in MarcMentat. The strain values were sampled along a radial path crossing the laminate thickness in the region of maximum bending moment.

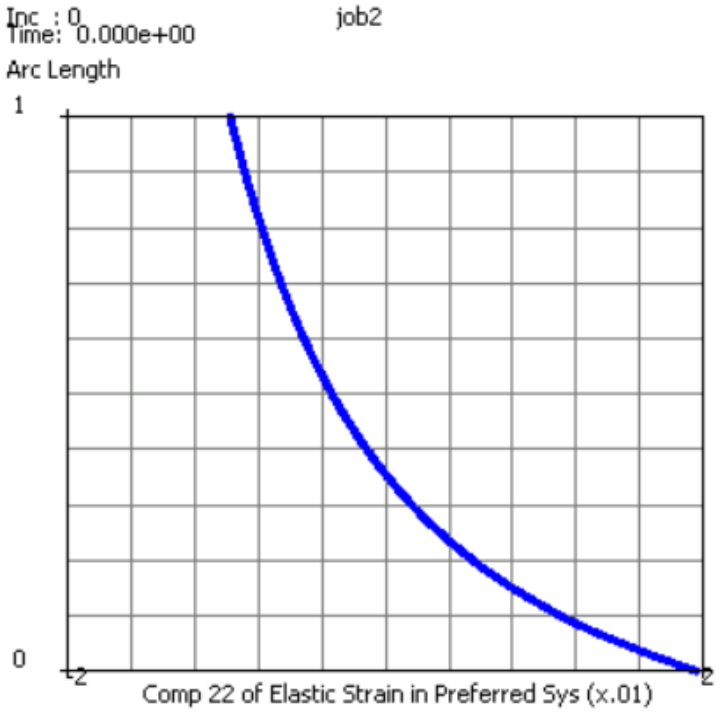

Figure 5.5: Path plot of the circumferential elastic strain component ε_{22} along the laminate thickness, obtained from the 3D solid FEM model under butterfly bending loading.

As shown in Fig. 5.5, the circumferential strain distribution exhibits a clear monotonic variation across the thickness, transitioning from positive values at the inner radius to negative values at the outer radius.

This behaviour is fully consistent with classical bending theory for curved beams. Under butterfly bending loading, the inner fibres of the laminate are subjected to tensile circumferential strains, while the outer fibres experience compressive strains. The change of sign of ε_{22} identifies the position of the neutral axis, where the circumferential strain vanishes.

The nearly linear trend of ε_{22} with respect to the through–thickness coordinate confirms that the deformation state is dominated by bending, with negligible membrane contribution. Such linearity is expected for an isotropic homogeneous laminate under pure bending conditions, where the strain distribution follows

$$\varepsilon_{22}(z) = -\kappa_{22}\, z,$$

with κ_{22} denoting the circumferential curvature and z measuring the distance from the neutral surface.

The smooth and regular variation observed in the FEM results further indicates that the mesh resolution across the thickness is sufficient to accurately capture the bending kinematics. No spurious oscillations or local irregularities are present, confirming that the extracted strain values can be reliably used for curvature evaluation.

The sign convention adopted in the present work leads to positive ε_{22} at the inner radius and negative values at the outer radius, which is consistent with the opening deformation associated with the imposed butterfly bending load. The symmetry of the strain distribution around the neutral axis further confirms that the deformation state is predominantly flexural.

This preliminary verification is essential, as the curvature κ_{22} employed in the ILTS recovery procedure is directly derived from the differential strain between the inner and outer fibres. The coherence of the ε_{22} profile with theoretical expectations therefore validates the kinematic basis of the subsequent post–processing step.

For the present case, the extracted strain values are:

$$\varepsilon_{22}^{\text{int}} = 1.979 \times 10^{-2}, \qquad \varepsilon_{22}^{\text{ext}} = -9.818 \times 10^{-3}.$$

where the strain components are dimensionless quantities.

These values are consistent with a bending–dominated deformation state, with tensile strain at the inner radius and compressive strain at the outer radius.

Following the curved beam approach proposed by Strozzi and discussed in Section 5.3.2, the circumferential curvature κ_{22} is evaluated from the differential rotation of circumferential fibres.

For the present aluminium configuration, the resulting curvature is

$$\kappa_{22} = -2.705 \times 10^{-2}\ \mathrm{mm}^{-1}.$$

The negative sign follows the adopted sign convention and indicates an opening deformation of the curved beam. This curvature value is used as master input for the ILTS recovery procedure.

Using the extracted curvature κ_{22} as input, the interlaminar stress distribution $\sigma_{33}(z)$ is reconstructed using the procedure described in Chapter 4.

The resulting through–thickness stress profile is shown in Fig. 5.6.

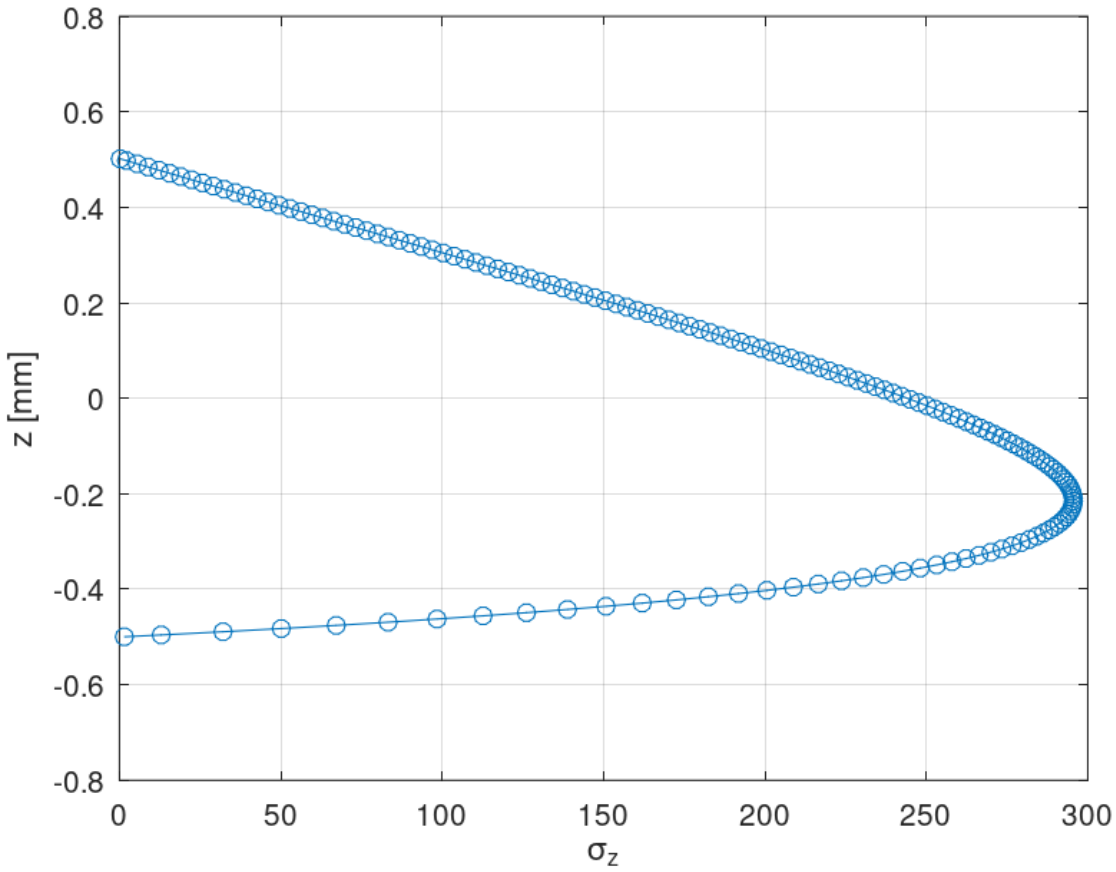

Figure 5.6: Through–thickness distribution of the interlaminar normal stress σ_{33} obtained from the proposed ILTS recovery method for the isotropic aluminum laminate.

The discrete markers along the curve correspond to the numerical sublayer dis-

cretisation adopted in the post–processing, while the continuous line represents the reconstructed stress field.

The recovered σ_{33} distribution exhibits a pronounced peak in the vicinity of the neutral radius, with a maximum absolute value close to 300 MPa, precisely a peak of 298 MPa. This behaviour is consistent with curved beam theory, where interlaminar normal stresses arise from the nonuniform bending–induced strain field across the thickness.

For comparison, the interlaminar stress component σ_{33} obtained directly from the 3D FEM model is shown in Fig. 5.7.

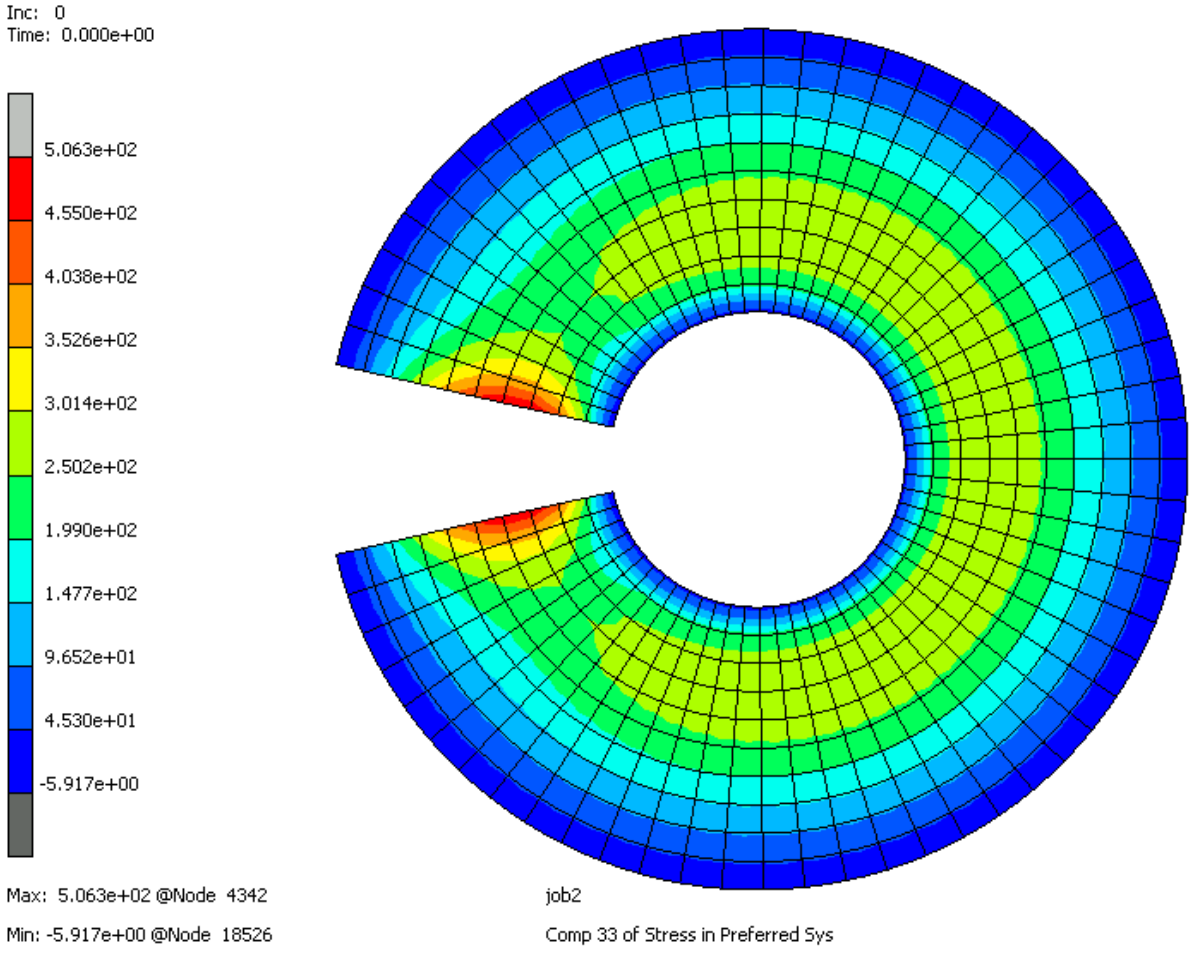

Figure 5.7: Contour plot of the interlaminar normal stress component σ_{33} obtained from the reference 3D solid finite element model under butterfly bending loading (aluminium model).

The FEM results indicate a maximum stress level of approximately 300 MPa,

located close to the neutral radius of the cross–section (light green path).

In order to extract the through–thickness distribution of the interlaminar normal stress from the 3D solid model, a dedicated *path plot* procedure was employed. A straight sampling path was defined across the thickness in the region of maximum stress concentration, as highlighted by the red line in Fig. 5.8. Using the *sample points* option, the σ_{33} values along this line were exported and subsequently used to reconstruct the FEM reference profile for comparison with the proposed recovery method.

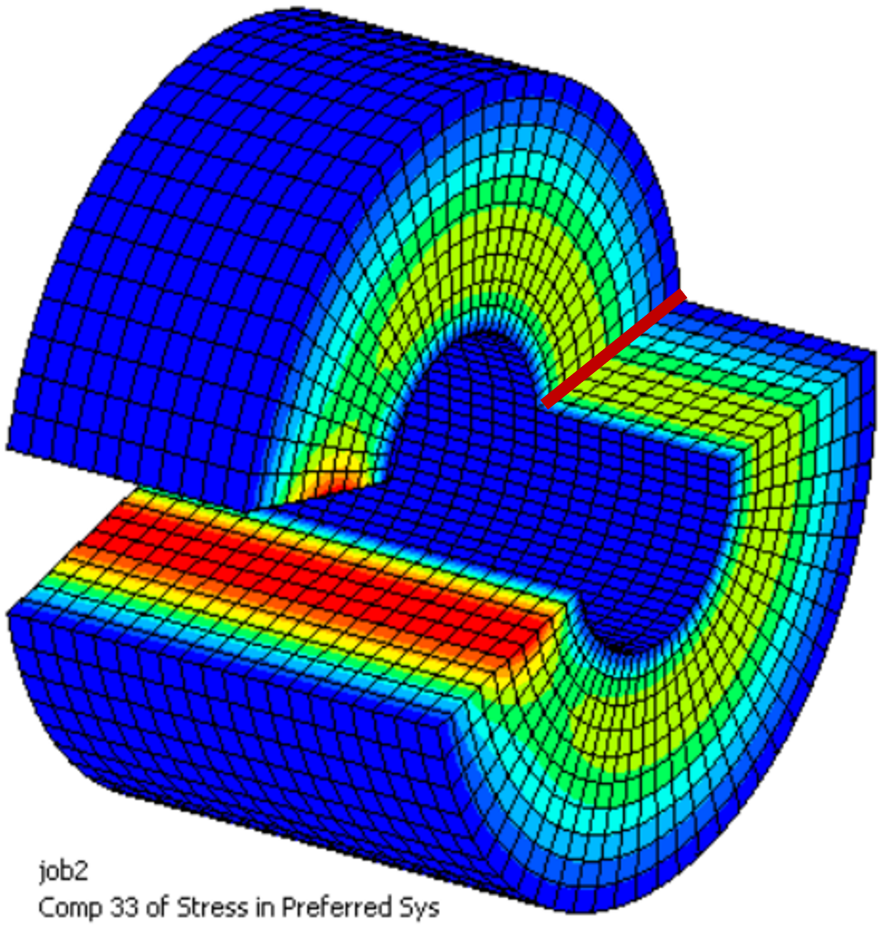

Figure 5.8: Extraction of the interlaminar normal stress σ_{33} from the 3D FEM model using a through–thickness path plot. The red line indicates the sampling path employed to obtain the σ_{33} distribution used for quantitative comparison.

A direct comparison between the recovered ILTS profile and the FEM reference solution is presented in Fig. 5.9.

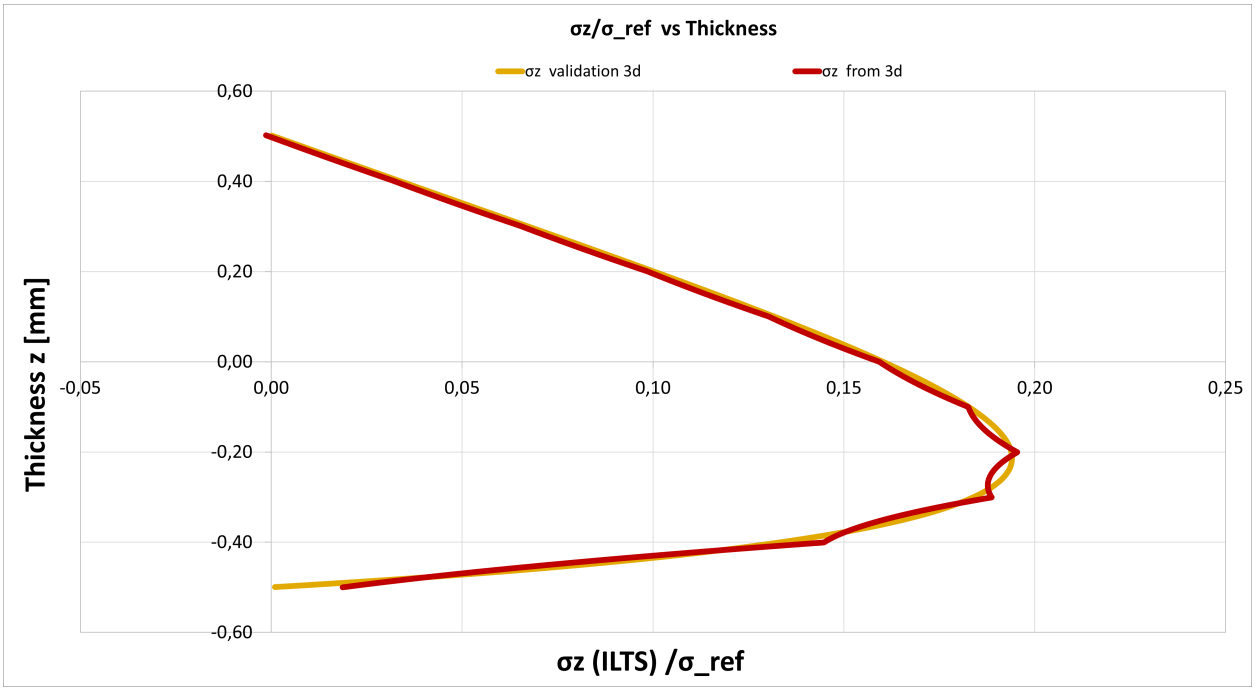

Figure 5.9: Through–thickness distribution of the interlaminar normal stress σ_{33} for the aluminium laminate under butterfly bending load, normalised by the reference circumferential stress σ_{22}. Comparison between the 3D FEM results and the stresses reconstructed through the proposed ILTS recovery procedure.

In the present comparison, the interlaminar normal stress σ_{33} obtained from both the 3D FEM model and from the proposed recovery procedure is normalised with respect to the maximum circumferential stress σ_{22}, precisely $1522,87$ MPa. It is important to remark that this normalisation is not part of the recovery algorithm itself, which provides the absolute through–thickness distribution of σ_{33}. The scaling by σ_{22} is introduced here as an additional post–processing step, using circumferential stresses directly extracted from the 3D FEM solution.

The stress component σ_{22} represents the dominant in–plane bending stress associated with the applied butterfly load and therefore constitutes a physically meaningful reference quantity. Normalising σ_{33} by σ_{22} allows the comparison to focus on the relative magnitude and distribution of interlaminar stresses with respect to the driving bending stress, independently of the absolute load level.

As shown in Fig. 5.9, the normalised stress profiles obtained from the recovery procedure and from the 3D FEM model are almost perfectly superposed over the

entire thickness. The agreement is observed both in the vicinity of the maximum stress and away from it, indicating that the recovered $\sigma_{33}(z)$ correctly scales with the reference circumferential stress.

It can be observed that the FEM profile is not perfectly linear, but exhibits small local oscillations along the thickness. These fluctuations are not related to any physical effect, but arise from the finite discretisation of the solid elements through the thickness and from the interpolation procedure adopted within the 3D finite element formulation. In particular, the limited number of elements and the path–sampling operation contribute to slight numerical irregularities in the extracted stress distribution.

This result provides further confirmation that the proposed recovery procedure accurately captures the mechanical link between bending–induced circumferential stresses and the resulting interlaminar normal stress field. Although the normalisation is performed externally, the excellent overlap between the two curves demonstrates that the recovered stress distribution is fully consistent with the three–dimensional reference solution in a relative sense.

However, considering the peaks of the ILTS from the FEM model and from the post-processing method, the relative error is given by

$$\varepsilon_{\mathrm{rel}} = \frac{|\sigma_{33}^{\mathrm{ILTS}} - \sigma_{33}^{\mathrm{FEM}}|}{\sigma_{33}^{\mathrm{FEM}}} = \frac{|298 - 300|}{300} = 6.67 \times 10^{-3},$$

corresponding to a relative error of approximately 0.67%, confirming the high accuracy of the recovery method for isotropic materials.

5.4.2 Quasi–isotropic CFRP laminate

The second validation case considers a quasi–isotropic carbon fibre reinforced polymer (CFRP) laminate, whose material properties and constitutive assumptions have already been introduced in Section 5.2.2.

Unlike the isotropic aluminium configuration discussed in Section 5.4.1, the present case introduces ply–level orthotropy and orientation effects, while preserving an approximately quasi–isotropic in–plane structural response. This allows the robustness of the proposed interlaminar stress recovery procedure to be assessed beyond the isotropic material assumption.

The laminate stacking sequence is defined as

$$[0/0/+45/-45/90]_{\mathrm{s}},$$

resulting in a symmetric layup with respect to the mid–thickness. Such configurations are commonly adopted in engineering applications where balanced in–plane stiffness is required together with the mechanical advantages of carbon fibre composites.

The orthotropic elastic properties of the unidirectional carbon/epoxy plies are summarised in Section 5.2.2. These parameters are representative of typical structural CFRP systems and introduce significant stiffness contrasts between fibre and transverse directions, which directly influence the through–thickness stress state and the resulting interlaminar normal stresses.

As for the aluminium case, the validation is performed by first analysing the full three–dimensional solid finite element model under butterfly bending loading. The circumferential strain component ε_{22} is extracted at the innermost and outermost plies of the laminate, which correspond to the locations of maximum tensile and compressive strain, respectively.

To further verify the bending kinematics in the composite case, a path plot of the circumferential elastic strain component ε_{22} across the laminate thickness was extracted from the 3D FEM model.

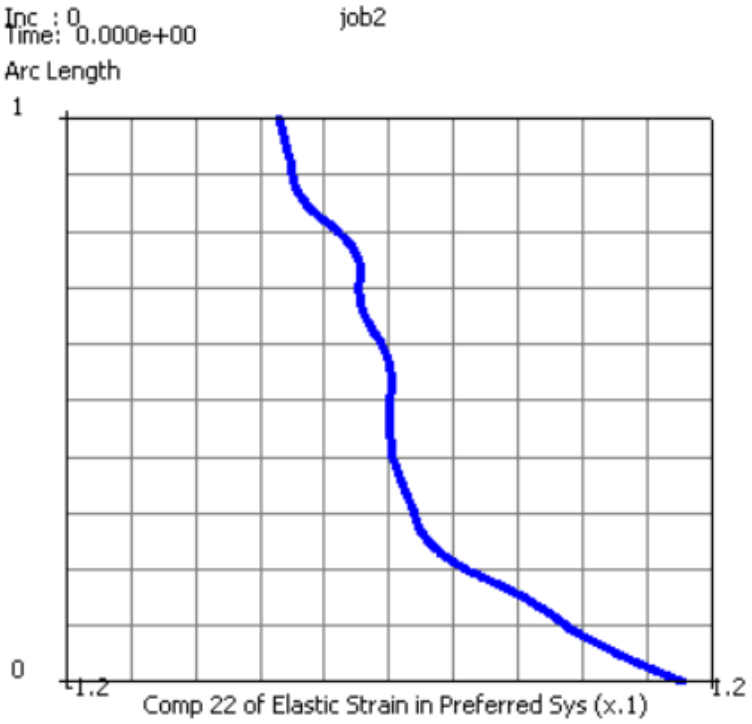

Figure 5.10: Path plot of the circumferential elastic strain component ε_{22} along the laminate thickness for the quasi–isotropic CFRP laminate under butterfly bending loading.

As shown in Fig. 5.10, the strain distribution varies monotonically across the thickness, transitioning from positive values at the inner radius to negative values at the outer radius. The zero crossing identifies the neutral axis of the section.

Although slight local deviations from perfect linearity are visible, these are attributed to ply–level orthotropy and stiffness contrasts between differently oriented layers. The overall trend remains clearly bending–dominated and fully consistent with curved beam behaviour under butterfly loading.

This confirms that the extracted strain values provide a reliable basis for the subsequent evaluation of the circumferential curvature κ_{22}.

For the quasi–isotropic CFRP configuration, the extracted strain values are

$$\varepsilon_{22}^{\text{int}} = 2.006 \times 10^{-2}, \qquad \varepsilon_{22}^{\text{ext}} = -1.284 \times 10^{-2},$$

where strains are dimensionless quantities.

Following the curved beam formulation proposed by Strozzi and consistently applied throughout this work, the circumferential curvature κ_{22} is evaluated from the differential rotation of circumferential fibres. For the present CFRP laminate, the resulting curvature is

$$\kappa_{22} = -3.217835 \times 10^{-2}\ \mathrm{mm}^{-1}.$$

The negative sign again reflects the adopted sign convention and indicates an opening deformation of the curved laminate.

The curvature value κ_{22} is subsequently employed as master input for the ILTS recovery procedure described in Chapter 4. The reconstructed through–thickness distribution of the interlaminar normal stress $\sigma_{33}(z)$ is shown in Fig. 5.11.

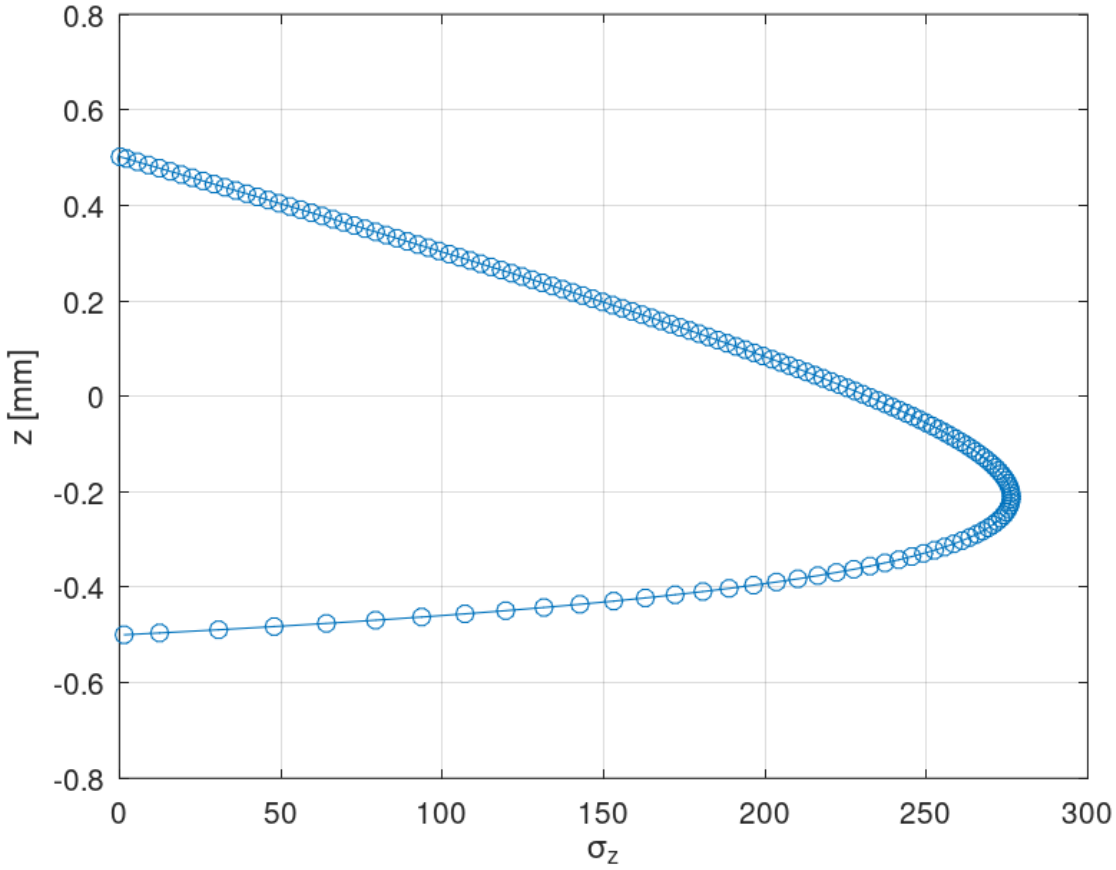

Figure 5.11: Through–thickness distribution of the interlaminar normal stress σ_{33} obtained from the proposed ILTS recovery method for the CFRP laminate.

The recovered stress profile exhibits a smooth, approximately parabolic distribution across the thickness, with a pronounced peak located close to the neutral radius of the laminate. The maximum interlaminar stress predicted by the recovery procedure is approximately

$$\sigma_{33,\max}^{\mathrm{ILTS}} \approx 277 \text{ MPa}.$$

Such behaviour is fully consistent with curved beam theory and confirms that the dominant interlaminar stress mechanism is driven by bending–induced strain gradients rather than local ply effects.

For reference, the interlaminar normal stress component σ_{33} obtained directly from the 3D FEM model reaches a maximum value of approximately

$$\sigma_{33,\max}^{\mathrm{FEM}} \approx 281 \text{ MPa},$$

located near the neutral radius of the curved section, as it is possible to observe in Fig. 5.12 (orange line).

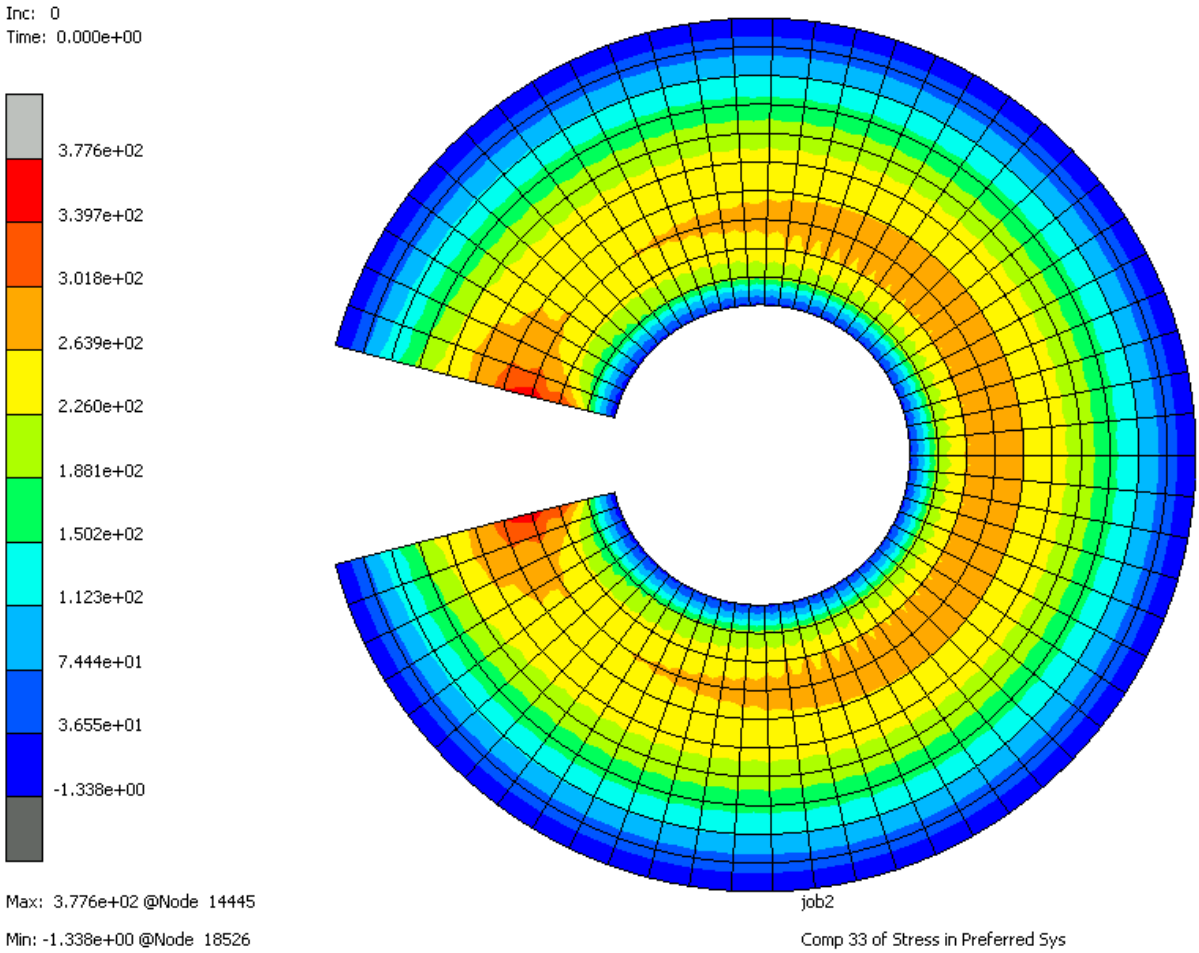

Figure 5.12: Contour plot of the interlaminar normal stress component σ_{33} obtained from the reference 3D solid finite element model under butterfly bending loading (CFRP model).

A direct comparison between the recovered ILTS profile and the 3D FEM reference solution is presented in Fig. 5.13.

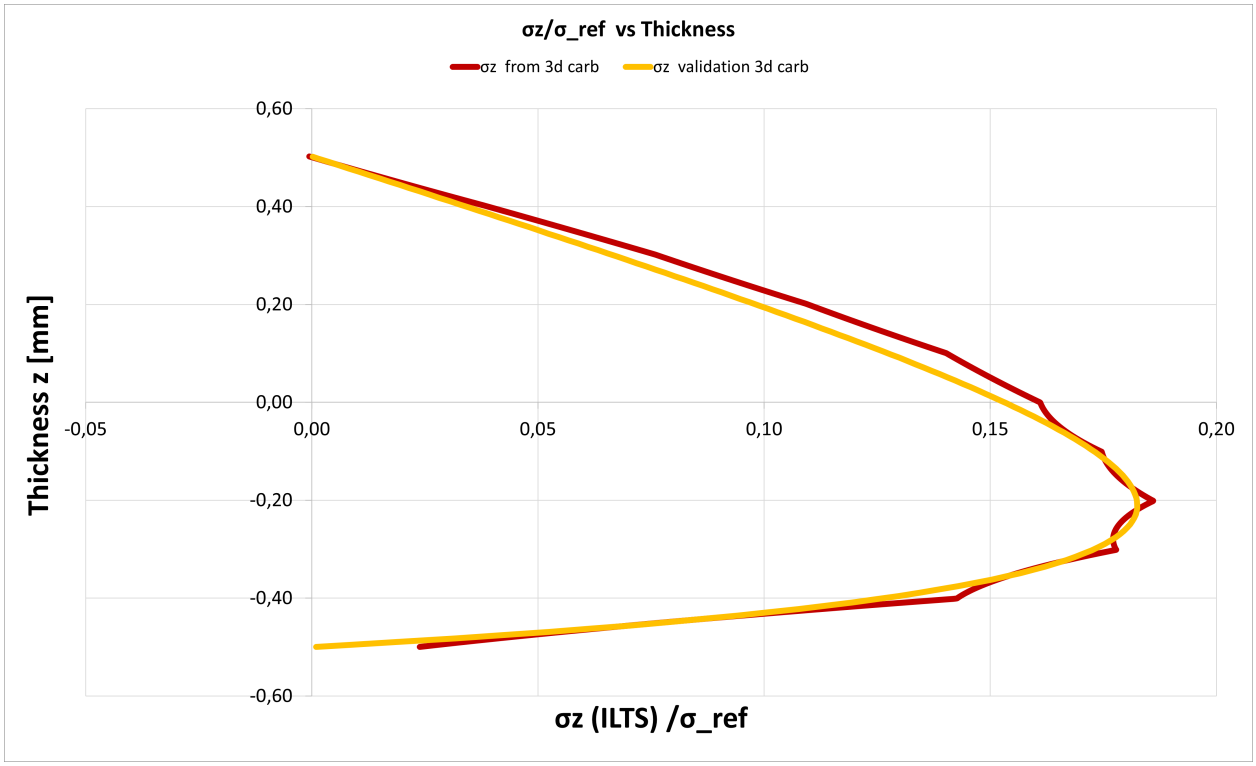

Figure 5.13: Through–thickness distribution of the interlaminar normal stress σ_{33} for the quasi–isotropic CFRP laminate under butterfly bending load, normalised by the reference circumferential stress σ_{22}. Comparison between the 3D FEM results and the stresses reconstructed through the proposed ILTS recovery procedure.

In the present comparison, the interlaminar normal stress σ_{33} obtained from both the three–dimensional FEM model and from the proposed recovery procedure is normalised with respect to the maximum circumferential stress σ_{22} of $1514,07$ MPa. As in the isotropic aluminium case, it is important to emphasise that this normalisation is not part of the recovery algorithm itself, which provides the absolute through–thickness distribution of σ_{33}. The scaling by σ_{22} is introduced here exclusively as a post–processing step, using circumferential stresses directly extracted from the 3D FEM solution.

For the CFRP laminate, the stress component σ_{22} represents the dominant in–plane bending stress associated with the applied butterfly load, even in the presence of ply–level orthotropy and orientation effects. Normalising σ_{33} by σ_{22} therefore allows the comparison to focus on the relative magnitude and distribution of inter-

laminar stresses with respect to the bending stress that drives the global deformation of the laminate.

As shown in Fig. 5.13, the normalised stress profiles obtained from the recovery procedure and from the 3D FEM model exhibit a very close overlap over the entire thickness. The agreement is particularly evident in the region surrounding the maximum interlaminar stress, indicating that the recovered $\sigma_{33}(z)$ correctly scales with the reference circumferential stress despite the increased material complexity.

Small deviations between the two curves can be observed locally. These differences are attributed to the intrinsic orthotropy of the individual plies and to the associated three–dimensional stress redistributions occurring at the ply interfaces, which are naturally captured by the solid FEM model but are described in an averaged sense by the curvature–driven recovery procedure.

Nevertheless, the normalised comparison clearly demonstrates that these local effects have a limited influence on the global interlaminar stress mechanism. The recovered stress profile remains fully consistent with the FEM reference solution in relative terms, confirming that the dominant coupling between bending–induced circumferential stresses and interlaminar normal stresses is correctly captured.

Considering the peak values of the interlaminar normal stress obtained from the two approaches, the relative error is given by

$$\varepsilon_{\mathrm{rel}} = \frac{|\sigma_{33,\max}^{\mathrm{ILTS}} - \sigma_{33,\max}^{\mathrm{FEM}}|}{\sigma_{33,\max}^{\mathrm{FEM}}} = \frac{|277 - 281|}{281} \approx 1.4\%.$$

Although slightly higher than in the isotropic aluminium case, this error remains very small and is fully acceptable in view of the increased material anisotropy and ply–level heterogeneity of the CFRP laminate. The excellent agreement observed in the normalised stress profiles further confirms the robustness of the proposed ILTS recovery framework when applied to quasi–isotropic composite laminates.

5.4.3 Sandwich laminate

The third validation case considers a curved sandwich laminate composed of stiff aluminium facesheets and a compliant polymeric core, whose material configuration has been previously introduced in Section 5.2.2. Compared to the homogeneous aluminium and quasi–isotropic CFRP laminates discussed in Sections 5.4.1 and 5.4.2, respectively, this configuration introduces a very pronounced stiffness contrast across the thickness.

Due to the extremely high stiffness contrast between the aluminium facesheets and the compliant polymeric core, the sandwich configuration exhibits a bending response that differs significantly from the homogeneous aluminium and quasi–isotropic CFRP laminates. For this reason, both the intensity and the distribution of the applied butterfly bending load must be carefully calibrated in order to ensure a physically meaningful deformation state.

First, in order to maintain realistic stress levels for sandwich structures, the maximum butterfly load intensity is reduced to $q_0 = 200$, instead of $q_0 = 1000$ adopted in the previous configurations. This choice avoids unrealistically large curvatures in the low–stiffness core and reflects typical loading conditions encountered in sandwich applications.

In addition, a specific calibration procedure is introduced to account for the large differences in Young's modulus between aluminium and polyurethane layers. The adopted strategy enforces *moment equivalence* between the reference antisymmetric butterfly load and the material–dependent load distribution applied to the laminate.

A reference antisymmetric butterfly load $q_{\text{ref}}(z)$ is first defined as

$$q_{\text{ref}}(z) = q_0 \,\text{sign}(z),$$

leading to a reference bending moment

$$M_{\mathrm{ref}} = \sum_k q_{\mathrm{ref}}(z_k)\, z_k\, t_k,$$

where z_k and t_k denote the through–thickness coordinate and thickness of the k–th layer, respectively.

Uncalibrated material–dependent butterfly loads are then defined for aluminium and polyurethane layers as

$$q_k^{\mathrm{base}} = E_k\, \mathrm{sign}(z_k),$$

where E_k is the Young's modulus of the corresponding layer. This choice naturally amplifies the contribution of the stiff aluminium facesheets while preserving the antisymmetric bending character of the load.

A single global scaling factor β is finally introduced in order to enforce moment equivalence,

$$\beta = \frac{M_{\mathrm{ref}}}{M_{\mathrm{base}}}, \qquad M_{\mathrm{base}} = \sum_k q_k^{\mathrm{base}}\, z_k\, t_k,$$

leading to the calibrated butterfly load

$$q_k = \beta\, q_k^{\mathrm{base}}.$$

This procedure guarantees that the total bending moment applied to the sandwich laminate is identical to the reference one, while consistently accounting for the large stiffness mismatch between facesheets and core. As a result, the induced curvature is physically meaningful and can be directly related to the bending stiffness of the laminate through

$$\kappa_{22} = \frac{M_{\mathrm{ref}}}{D_{22}}, \qquad D_{22} = \sum_k E_k\, z_k^2\, t_k,$$

which is subsequently used as master input for the ILTS recovery procedure.

As for the other validation cases, the analysis starts from the three–dimensional solid finite element model. The circumferential strain component ε_{22} is extracted at the innermost and outermost aluminium layers, and the corresponding circumferential curvature κ_{22} is evaluated using the Strozzi's approach. The resulting curvature is then employed as input for the interlaminar stress recovery code developed in Chapter 4.

The comparison between the reconstructed interlaminar stress distribution and the reference three–dimensional FEM solution, normalised by the reference circumferential stress σ_{22}, is shown in Fig. 5.14.

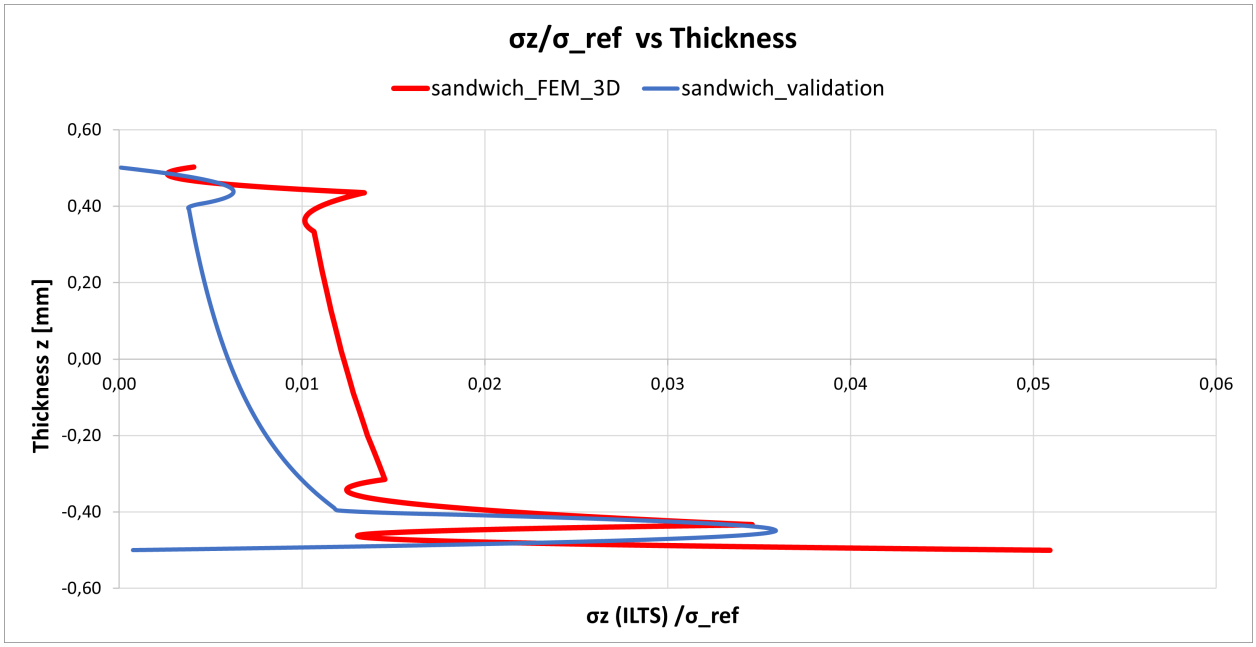

Figure 5.14: Through–thickness distribution of the interlaminar normal stress σ_{33} for the sandwich laminate with polyurethane core under butterfly bending load, normalised by the reference circumferential stress σ_{22}. Comparison between the 3D FEM results and the stresses reconstructed through the proposed ILTS recovery procedure.

A comparison with the reference 3D FEM solution reveals a noticeable discrepancy between the two normalised stress profiles.

In particular, the interlaminar stresses reconstructed within the polyurethane core are systematically lower than those obtained directly from the three–dimensional model, as highlighted by the deviation between the recovered curve and the FEM

reference.

To better understand the origin of this mismatch, the circumferential strain field ε_{22} obtained from the 3D FEM model was analysed in detail across the laminate thickness. The corresponding strain distribution is shown in Fig. 5.15.

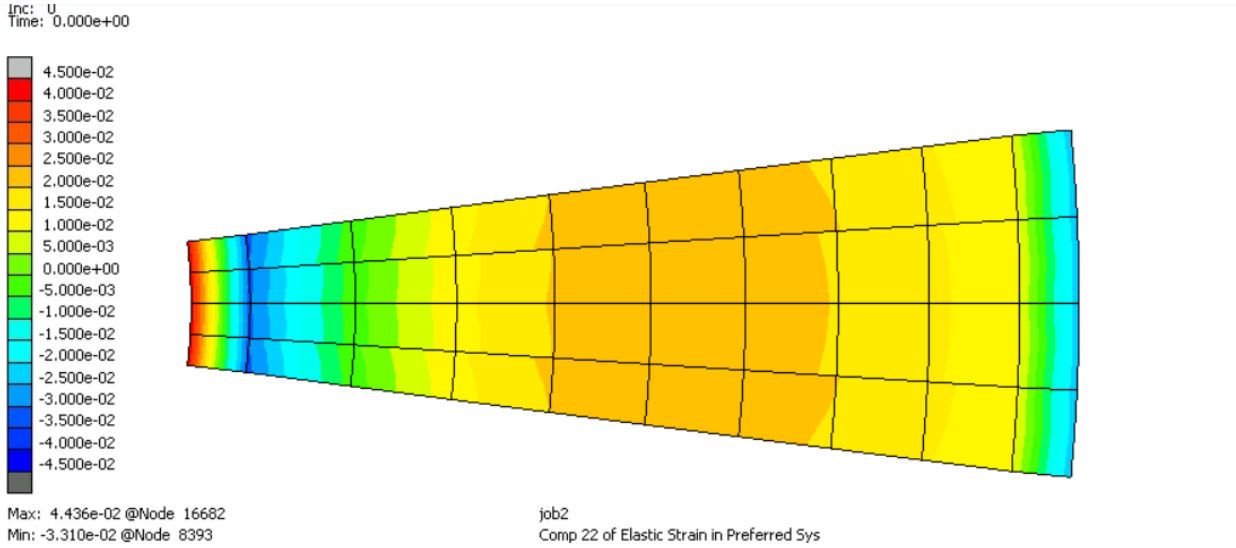

Figure 5.15: Distribution of the circumferential strain component ε_{22} across the sandwich laminate thickness. Multiple zero–strain locations can be observed within the core region, indicating the presence of more than one effective neutral axis.

Unlike the previous validation cases, the strain ε_{22} does not vanish at a single through–thickness location. Instead, three distinct zero–strain points can be identified, suggesting the presence of multiple effective neutral axes. This behaviour is fundamentally different from the classical bending response assumed in curved beam and shell theories, where a single neutral axis characterises the deformation.

In order to further investigate the anomalous strain distribution observed in the sandwich configuration, additional numerical tests were performed. Three different configurations were analysed through dedicated through–thickness path plots of the circumferential strain component ε_{22}:

1. the original open–face sandwich configuration;

2. a modified model in which thin aluminium plates were added to close the open faces of the foam core;

3. a further configuration in which the closing plates were assigned an artificially high Young's modulus ($E = 10^7$ MPa) in order to enforce an almost rigid constraint and promote a more uniform load transfer.

The corresponding strain distributions are reported in Fig. 5.16.

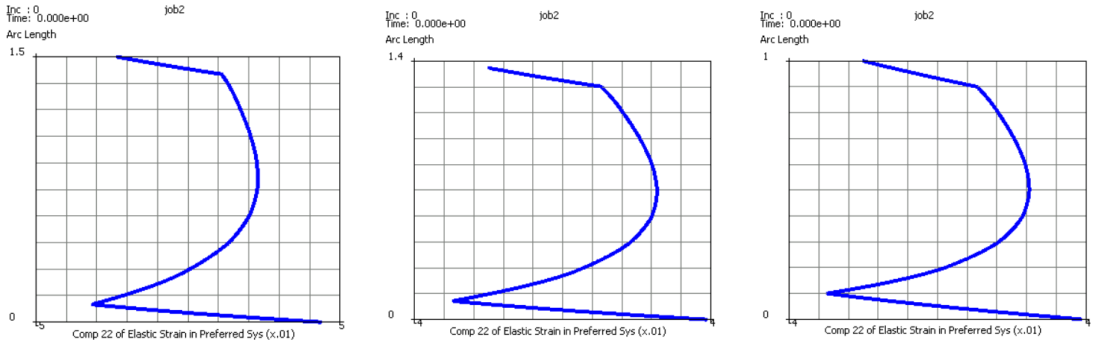

Figure 5.16: Through–thickness path plots of the circumferential strain component ε_{22} for the sandwich laminate under butterfly bending loading: (left) original open–face configuration; (centre) configuration with aluminium closing plates; (right) configuration with artificially stiff closing plates ($E = 10^7$ MPa).

Remarkably, all three configurations exhibit the same qualitative behaviour. The strain field does not follow the classical linear through–thickness variation predicted by laminate and curved beam theory. Instead, the distributions display pronounced curvature changes and multiple zero–strain crossings, indicating the presence of several effective neutral axes within the core region.

The persistence of this behaviour, even when rigid closing plates are introduced, demonstrates that the anomaly is not caused by boundary conditions or load application details. Rather, it is an intrinsic consequence of the extreme stiffness mismatch between the aluminium facesheets and the highly compliant polyurethane core.

From a theoretical standpoint, such a strain pattern is incompatible with the fundamental assumption of a single global curvature κ_{22} governing the bending response. Since the proposed ILTS recovery framework is curvature–driven, its validity relies on the existence of a well–defined neutral axis and an approximately linear bending strain distribution.

The sandwich configuration therefore violates the core kinematic hypotheses underlying classical laminate and shell theory. For this reason, this case falls outside the intended applicability range of the present recovery framework and is not considered suitable for further quantitative discussion within this thesis.

Nevertheless, this analysis is highly instructive, as it clearly identifies the physical limits of curvature–based interlaminar stress recovery methods when applied to structures characterised by extreme through–thickness stiffness heterogeneity.

The observed strain pattern is a direct consequence of the extreme stiffness mismatch between the aluminum facesheets and the compliant polyurethane core, combined with the nearly closed circumferential geometry of the structure. Under butterfly bending loading, the soft core is unable to enforce a uniform circumferential extension or contraction, allowing the inner and outer facesheets to deform in a partially decoupled manner. As a result, local bending and shear deformation modes develop within the core, leading to a nonclassical strain distribution.

From a theoretical standpoint, this behaviour violates one of the key assumptions underlying the proposed recovery framework, namely the existence of a single effective curvature κ_{22} describing the bending state of the laminate. While the curvature extracted via the Strozzi approach provides a global, averaged measure of bending, it is no longer sufficient to fully describe the actual three–dimensional deformation state of the sandwich structure.

Consequently, the recovered interlaminar stress distribution, although qualitatively consistent with bending–dominated behaviour, cannot quantitatively reproduce the stress levels observed in the 3D FEM solution. The discrepancy observed in this case therefore does not indicate a limitation of the numerical implementation, but rather highlights the theoretical limits of curvature–based shell recovery methods when applied to highly heterogeneous sandwich structures.

This validation case is particularly instructive, as it clearly identifies the conditions under which classical shell and curved beam assumptions cease to be applica-

ble. In the presence of very compliant cores and strong through–thickness stiffness gradients, a full three–dimensional analysis or enhanced higher–order kinematic descriptions may be required to accurately capture the interlaminar stress state.

5.4.4 Anti–sandwich laminate

The last validation case considers an *anti–sandwich* laminate configuration, whose material layout has been introduced in Section 5.2.2. In this configuration, the stiff aluminium layers are located in the central part of the laminate, while the outer and inner layers are composed of a compliant polyurethane foam. Although such a stacking sequence has limited practical relevance for structural applications, it represents a valuable benchmark for assessing the limits and robustness of the proposed ILTS recovery procedure under extreme stiffness heterogeneity.

As for the sandwich configuration discussed previously, the applied butterfly bending load is limited to a maximum intensity of 200 N/mm. This choice is motivated by the large contrast between the elastic moduli of aluminium and polyurethane, which would otherwise lead to unrealistic deformation levels and numerical artefacts. The butterfly loading is calibrated following the same moment–equivalence procedure adopted for the sandwich laminate, ensuring that the total bending moment transmitted to the structure is consistent with the reference three–dimensional model.

The extraction of the circumferential strain components ε_{22} from the 3D FEM model, the evaluation of the curvature κ_{22} via the Strozzi approach, and the subsequent post–processing for the recovery of σ_{33} are performed following exactly the same steps described for the previous validation cases. For this reason, the discussion is focused directly on the resulting stress distributions.

For completeness, the circumferential strain distribution across the thickness was also inspected through a dedicated path plot extracted from the 3D FEM model.

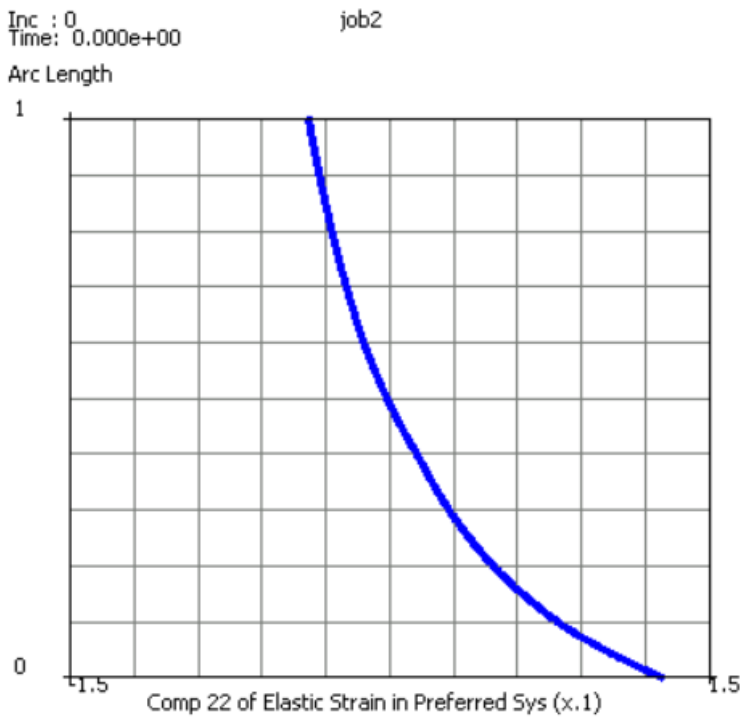

Figure 5.17: Path plot of the circumferential elastic strain component ε_{22} along the laminate thickness for the anti–sandwich configuration under butterfly bending loading.

As shown in Fig. 5.17, the strain profile remains globally monotonic, transitioning from tensile values at the inner radius to compressive values at the outer radius and crossing the neutral axis within the thickness.

The overall trend clearly reflects a bending–dominated deformation state, confirming the physical consistency of the extracted ε_{22} field and the reliability of the curvature evaluation employed in the subsequent ILTS recovery.

The reconstructed through–thickness distribution of the interlaminar normal stress $\sigma_{33}(z)$ is shown in Fig. 5.18.

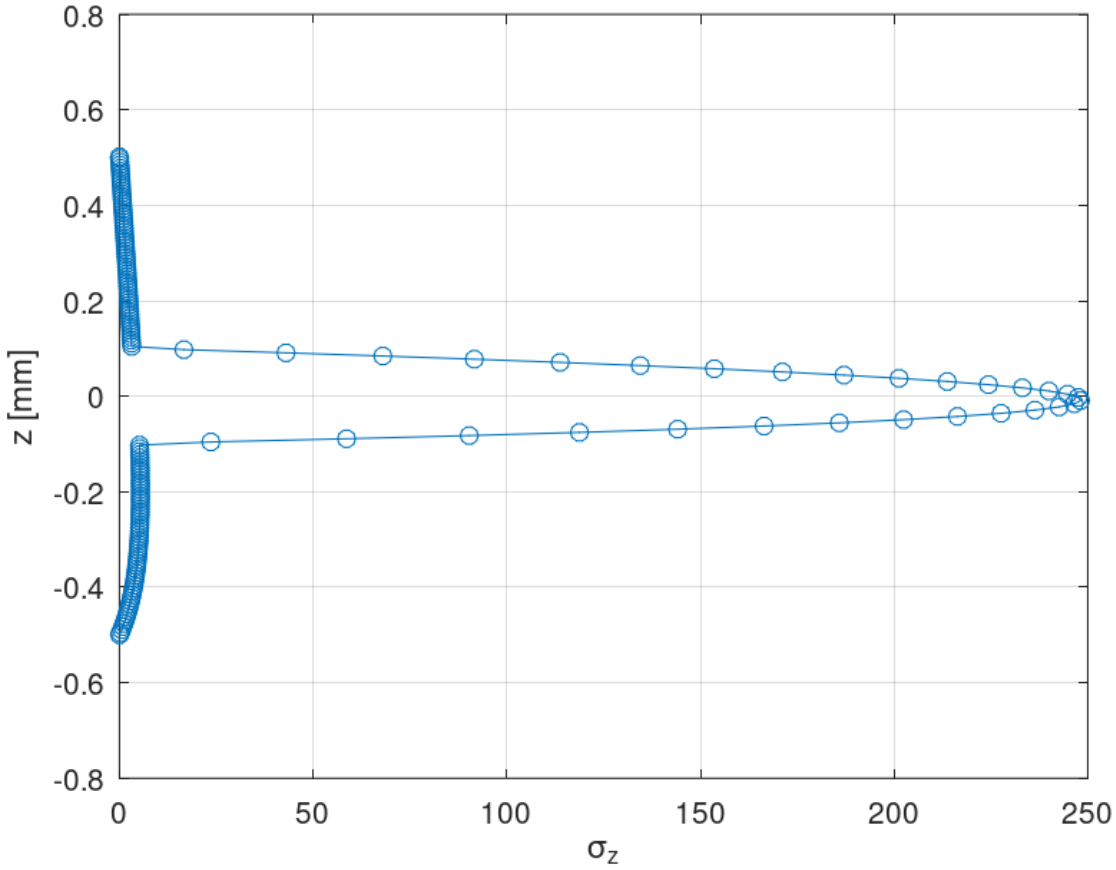

Figure 5.18: Through–thickness distribution of the interlaminar normal stress σ_{33} obtained from the proposed ILTS recovery procedure for the anti–sandwich laminate.

The resulting stress profile differs significantly from the classical parabolic shape observed in homogeneous or quasi–homogeneous laminates. This behaviour is expected and can be directly attributed to the particular material arrangement. Since the aluminium layers are confined to the central region of the laminate (layers 5–6), the bending stiffness is highly localised around the mid–thickness, while the surrounding polyurethane layers provide only a marginal contribution to load carrying.

As a consequence, the interlaminar normal stresses concentrate primarily in the vicinity of the aluminium layers, while remaining relatively low in the foam regions. This leads to a characteristic stress profile with steep gradients near the aluminium–foam interfaces and almost flat distributions within the compliant layers. The max-

imum interlaminar stress predicted by the recovery procedure is approximately

$$\sigma_{33,\max}^{\mathrm{ILTS}} \approx 250 \text{ MPa}.$$

For comparison, the peak value of the interlaminar normal stress obtained directly from the 3D FEM model is approximately

$$\sigma_{33,\max}^{\mathrm{FEM}} \approx 275 \text{ MPa}.$$

The corresponding relative error is therefore

$$\varepsilon_{\mathrm{rel}} = \frac{|250 - 275|}{275} \approx 9\%.$$

While this error is higher than those observed for the aluminium and CFRP laminates, it remains reasonably low considering the extreme stiffness contrast and the nonstandard material layout of the anti–sandwich configuration.

A more detailed comparison between the recovered and FEM–computed interlaminar stresses is provided in Fig. 5.19, where the stress profiles are normalised with respect to the reference circumferential stress σ_{22} extracted from the 3D FEM model.

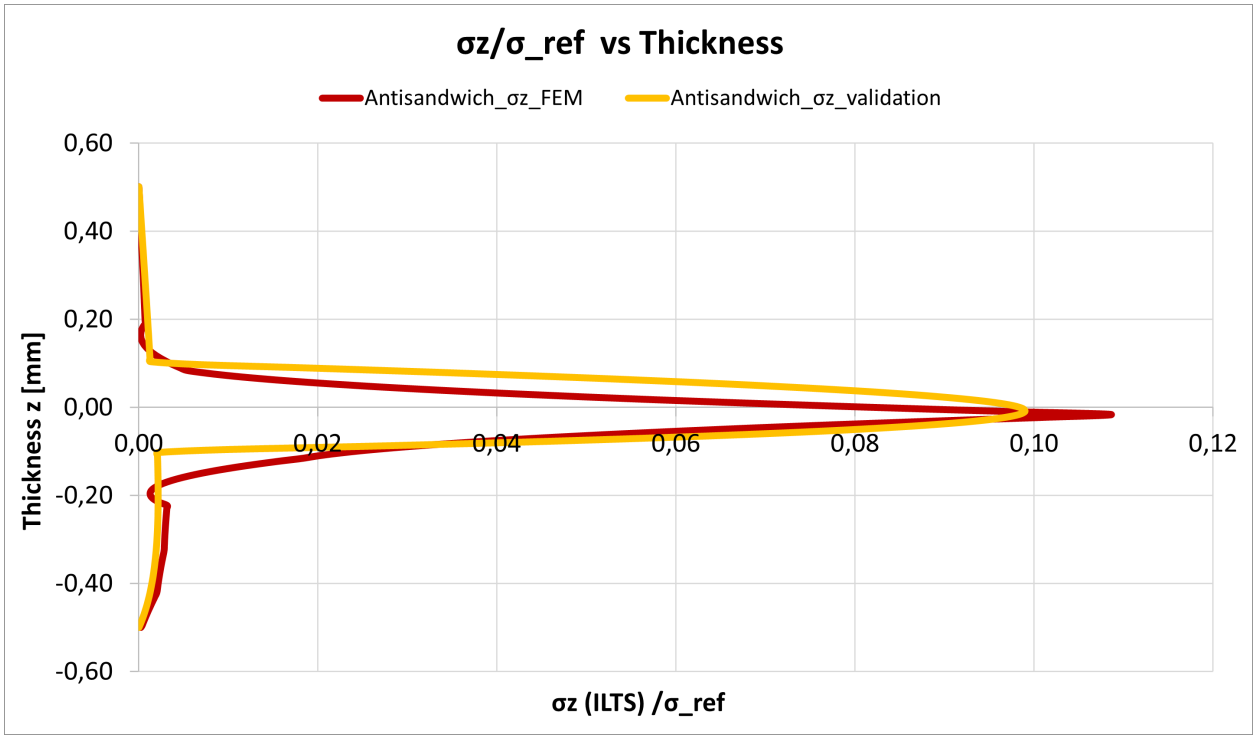

Figure 5.19: Comparison between the interlaminar normal stress σ_{33} obtained from the 3D FEM model and from the proposed recovery procedure for the anti–sandwich laminate, normalised by the reference circumferential stress σ_{22}.

The comparison highlights a clear discrepancy between the two solutions within the polyurethane layers. In particular, the recovered stress distribution predicts nearly zero interlaminar stresses in the outer foam regions, whereas the 3D FEM model exhibits non–negligible stress levels.

This difference can be explained by the fundamental assumptions underlying the recovery procedure. The proposed method is curvature–driven and relies on the dominant bending behaviour of the structure. In the anti–sandwich configuration, however, the compliant foam layers are weakly coupled to the global bending curvature and are strongly affected by local three–dimensional effects, including transverse constraint, shear deformation, and local compatibility conditions at the aluminium–foam interfaces.

These effects are fully captured by the 3D solid finite element model but are not explicitly represented in the reduced recovery framework, which assumes a through–thickness stress distribution primarily governed by bending curvature. As a result,

the recovery procedure tends to underestimate interlaminar stresses in the foam regions, particularly near the outer surfaces of the laminate.

Nevertheless, the normalised comparison confirms that the recovery procedure accurately captures the dominant stress mechanism associated with the aluminium layers, which govern the overall bending response of the structure. The location of the peak stress and its relative magnitude with respect to the driving circumferential stress are correctly reproduced.

Overall, this validation case highlights both the strengths and the limitations of the proposed ILTS recovery framework. While the method performs extremely well for homogeneous, quasi–isotropic, and classical sandwich laminates, its accuracy decreases in configurations where bending stiffness is highly localised and three–dimensional effects in compliant layers become dominant. These results provide valuable insight into the range of applicability of the method and further confirm its physical consistency.

5.4.5 Summary of the previous results

The four validation cases analysed in this section provide a comprehensive assessment of the proposed interlaminar stress recovery (ILTS) procedure, ranging from ideal homogeneous configurations to highly heterogeneous laminates characterised by extreme stiffness contrasts.

In the isotropic aluminum laminate, the recovery method achieves an excellent level of accuracy. The through–thickness distribution of σ_{33} is reproduced with almost perfect agreement with the three–dimensional FEM reference solution, both in terms of peak value and relative stress distribution. The very small relative error (below 1%) confirms that, when the assumptions of classical curved beam theory are fully satisfied, namely material homogeneity and the existence of a single effective bending curvature, the proposed curvature–driven recovery framework is able to faithfully reproduce the dominant interlaminar stress mechanism.

The quasi–isotropic CFRP laminate represents a first increase in complexity, as ply–level orthotropy and orientation effects are introduced. Despite this, the results demonstrate that the recovery procedure remains highly accurate. The normalised comparison with the 3D FEM solution shows a very close overlap of the stress profiles, and the relative error on the peak interlaminar stress remains below 2%. This indicates that, although the laminate is locally anisotropic, its global bending behaviour can still be effectively described by a single equivalent curvature. Local three–dimensional effects at ply interfaces and stiffness redistributions induced by fibre orientation lead only to minor deviations, which do not compromise the overall accuracy of the method. These results confirm that the proposed framework is robust and applicable to realistic composite laminates of engineering relevance.

A fundamentally different behaviour emerges for the sandwich laminate with compliant polyurethane core. In this case, the extreme stiffness contrast between aluminum facesheets and core material leads to a nonclassical bending response. The three–dimensional FEM results clearly show that the circumferential strain ε_{22} does not vanish at a single through–thickness location, but instead exhibits multiple zero–strain points, indicating the presence of more than one effective neutral axis. This behaviour violates one of the key assumptions underlying the recovery procedure, namely the existence of a unique curvature κ_{22} describing the bending state of the laminate.

As a consequence, the curvature extracted from the FEM strain field represents only an averaged measure of the global bending response and is not sufficient to fully describe the local deformation mechanisms developing within the compliant core. The recovered interlaminar stresses therefore underestimate the FEM solution in the core region. This discrepancy does not stem from numerical inaccuracies, but rather highlights a theoretical limitation of curvature–based shell recovery methods when applied to highly heterogeneous sandwich structures. In such cases, local bending, shear and three–dimensional constraint effects become dominant and cannot be

captured by a single curvature parameter.

The anti–sandwich laminate further accentuates these limitations and represents an extreme test case for the proposed method. Here, the bending stiffness is highly localised within the central aluminum layers, while the surrounding foam regions play only a marginal role in carrying bending loads. As a result, the interlaminar normal stresses concentrate near the aluminum layers, leading to steep stress gradients at the aluminum–foam interfaces and relatively low stress levels elsewhere.

The recovery procedure correctly captures the dominant stress mechanism associated with the stiff aluminium layers, including the location of the peak interlaminar stress and its scaling with the reference circumferential stress. However, the comparison with the 3D FEM solution reveals noticeable differences in the compliant foam regions, where the recovered stresses are significantly lower than those predicted by the solid model. These discrepancies can be attributed to three–dimensional effects such as transverse constraint, local compatibility conditions and shear deformation, which are inherently captured by the 3D FEM model but lie outside the scope of a curvature–driven recovery framework. The higher relative error observed in this case (approximately 9%) therefore reflects the physical limitations of the underlying assumptions rather than deficiencies of the implementation.

Overall, the four validation cases clearly delineate the range of applicability of the proposed ILTS recovery procedure. The method performs exceptionally well for homogeneous, quasi–isotropic and classical bending–dominated laminates, where the deformation can be described by a single effective curvature. Its accuracy progressively decreases as the through–thickness stiffness heterogeneity increases and three–dimensional deformation mechanisms become dominant. Nevertheless, even in extreme configurations, the recovery framework retains the ability to identify the dominant interlaminar stress mechanisms and provides physically consistent trends.

These results confirm that the proposed method constitutes a reliable and computationally efficient tool for the recovery of interlaminar normal stresses in curved lam-

inated structures, while also clearly identifying the conditions under which higher–order or fully three–dimensional approaches may be required.

5.5 Validation against reference results from literature

In order to further assess the robustness and generality of the proposed interlaminar stress recovery procedure, an additional validation is performed against independent reference data available in the open literature. Unlike the previous validation stage, which relied on a tailored 3D finite element model developed within this work, the present comparison is based on a benchmark configuration characterised by different geometry, materials, stacking sequence and loading conditions. This step therefore provides an independent verification of the proposed approach.

The reference data are taken from the study by Raju et al. (QuEST Global, 2014), where interlaminar stresses in curved composite laminates subjected to bending are investigated through detailed three-dimensional finite element analyses [**?**].[31]

Reference geometry and loading configuration.

The benchmark structure consists of a curved L–bend composite specimen, as illustrated in Fig. 5.20.

[31]The reference paper is provided as supplementary material and is freely available online.

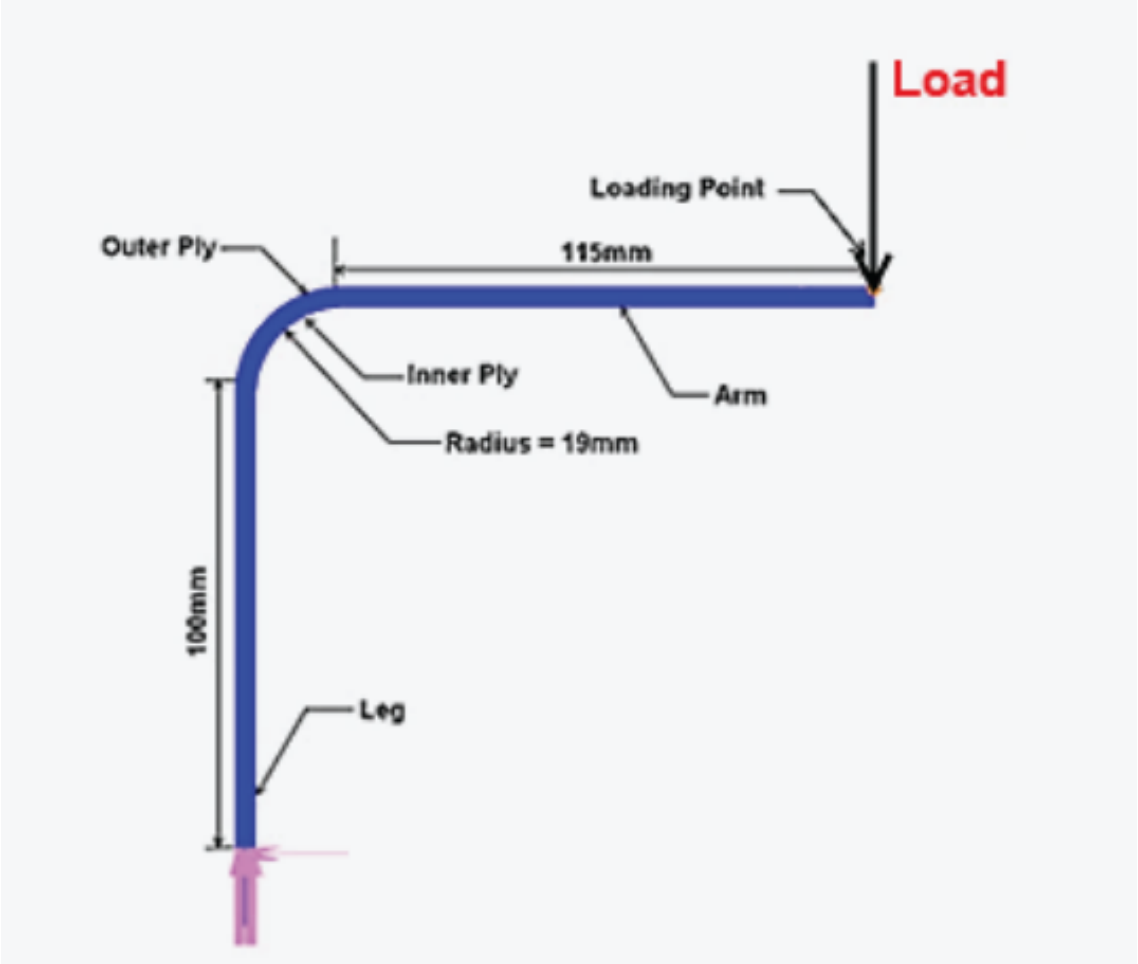

Figure 5.20: Geometry and loading configuration of the curved L–bend specimen considered for validation against literature data.

The specimen comprises two straight arms connected by a curved region with constant radius. The inner bend radius is equal to $r = 19$ mm, while the horizontal arm length is $L = 115$ mm. All nodes at the base of the vertical arm are fully constrained, whereas a prescribed vertical displacement of 100 mm is applied at the tip of the horizontal arm. This loading condition induces a predominantly bending–dominated response in the curved region, leading to the development of significant interlaminar tensile stresses.

Laminate configuration and material properties.

Among the three stacking sequences analysed in the reference study, only *Layup 1* is considered here for validation purposes. This laminate is composed exclusively

of chopped strand mat (CSM) plies, with a total of seven layers and an overall thickness of 4.62 mm. The corresponding stacking sequence is

$$[\text{CSM/CSM/CSM/CSM/CSM/CSM/CSM}].$$

The orthotropic elastic properties of the CSM material are reported in Table 5.1 and are representative of hand–layup glass fibre reinforced polymer systems.

Property	**CSM**
E_{11} [MPa]	9607
E_{22} [MPa]	9607
E_{33} [MPa]	6062
ν_{12} [-]	0.347
ν_{23} [-]	0.139
ν_{31} [-]	0.108
G_{12} [MPa]	2602
G_{23} [MPa]	1847
G_{31} [MPa]	1847

Table 5.1: Orthotropic elastic properties of the CSM laminate used for validation against literature data (hand–layup process).

Evaluation of the input curvature.

Since the reference study does not directly provide curvature values, the input curvature required by the present ILTS recovery procedure must be estimated from the prescribed displacement and specimen geometry. Assuming small rotations and a bending–dominated deformation of the curved region, the effective curvature κ_{22} is approximated as

$$\kappa_{22} \approx \frac{\theta}{L}, \qquad \theta \approx \frac{u}{L},$$

where u is the imposed vertical displacement at the loading point and L is the length of the horizontal arm. For $u = 100$ mm and $L = 115$ mm, this yields

$$\kappa_{22} \approx \frac{u}{L^2} \simeq 7.56 \times 10^{-3}\ \text{mm}^{-1}.$$

This curvature value is subsequently used as the master input variable κ_{22} for the interlaminar stress recovery procedure described in Chapter 4.

Comparison of interlaminar stress distributions.

The reference finite element results reported by Raju et al. show that the interlaminar tensile stress σ_{33} reaches its maximum value between the third and fourth layers of the laminate, i.e. close to the mid–thickness of the curved , as shown in Fig. 5.21.

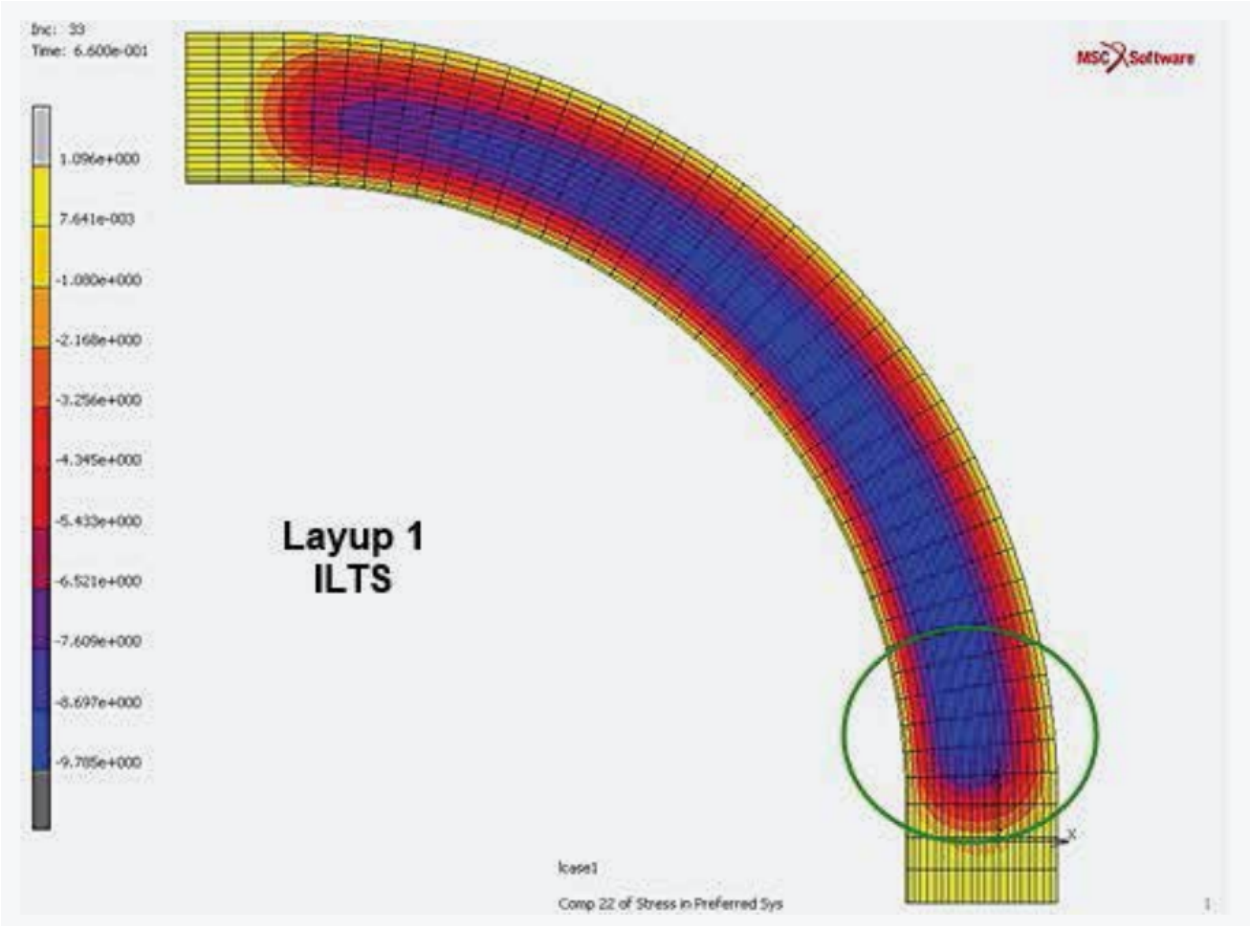

Figure 5.21: Interlaminar tensile stress (ILTS) distribution obtained from the reference 3D finite element model for Layup 1.

The peak ILTS for Layup 1 is reported as

$$\sigma_{33}^{\text{ref}} \approx 9.78 \text{ MPa}.$$

Applying the proposed recovery procedure with the estimated curvature input

yields the through–thickness distribution shown in Fig. 5.22.

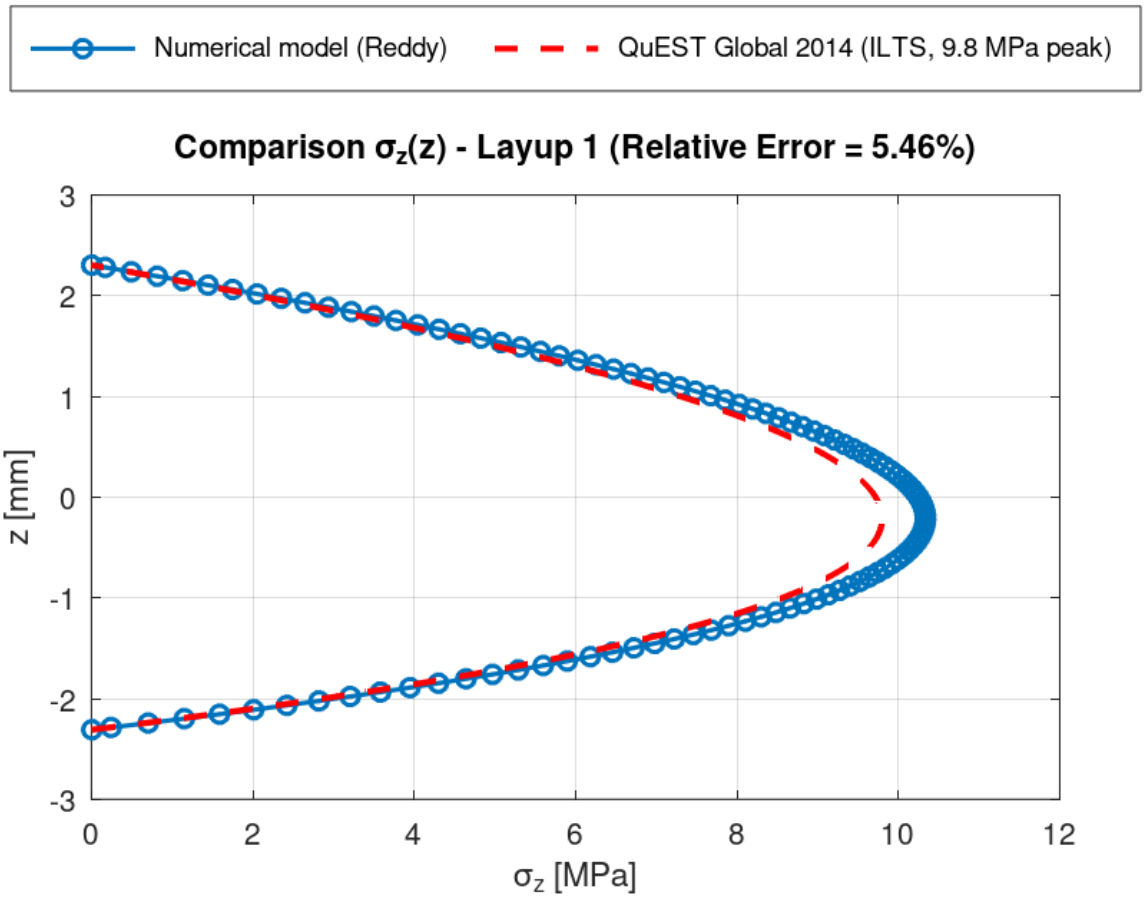

Figure 5.22: Through–thickness comparison of the transverse normal stress σ_{33} for Layup 1. Results obtained with the proposed ILTS recovery method are compared with the reference data reported by QuEST Global (2014).

The recovered interlaminar stress exhibits the expected qualitative behaviour: zero values at the outer surfaces and a maximum located in the central region of the laminate. The predicted peak value is

$$\sigma_{33}^{\mathrm{num}} \approx 10.31 \text{ MPa}.$$

The relative error with respect to the reference result is therefore

$$\varepsilon_{\mathrm{rel}} = \frac{|\sigma_{33}^{\mathrm{num}} - \sigma_{33}^{\mathrm{ref}}|}{\sigma_{33}^{\mathrm{ref}}} \simeq 5.46\%.$$

Discussion.

The agreement between the recovered and reference interlaminar stress distributions is considered very satisfactory, both in terms of magnitude and spatial location of the peak stress. The observed discrepancy of approximately 5% can be reasonably attributed to the approximations introduced in the estimation of the input curvature, which is derived from global displacement data rather than from a direct strain–based evaluation. Additional sources of deviation include differences in the effective boundary conditions, material modelling assumptions, and the fact that the reference finite element results are obtained from a fully nonlinear three–dimensional analysis.

Despite these simplifications, the recovered ILTS values remain within the same order of magnitude as the reference data and correctly capture the through–thickness stress evolution. This independent validation therefore confirms the reliability of the proposed interlaminar stress recovery method and supports its applicability to curved composite structures beyond the specific configurations analysed in this work.

5.6 Shell finite element model as target application

The final objective of the proposed interlaminar stress recovery procedure is its application to shell-based finite element models, which are widely employed in the analysis and design of laminated composite structures due to their computational efficiency.

To this end, a two-dimensional shell finite element model is considered as the target application of the method. The shell model is derived directly from the previously introduced three-dimensional reference geometry and represents a reduced-order description of the same physical structure.

5.6.1 Geometrical and material consistency

The shell model preserves exactly the same midsurface geometry of the three-dimensional ring segment described in Section 5.2, including the angular opening, inner and outer radii, and axial length (Fig. 5.23 and Fig. 5.24).

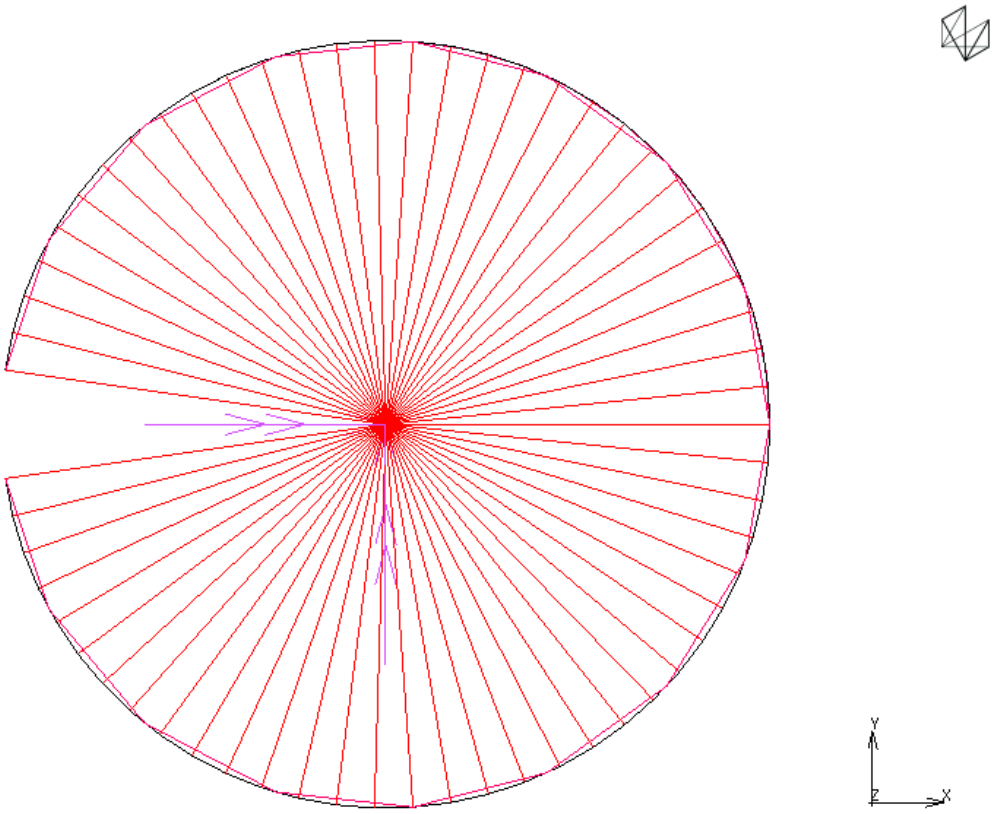

Figure 5.23: Lateral view of the 2D shell model

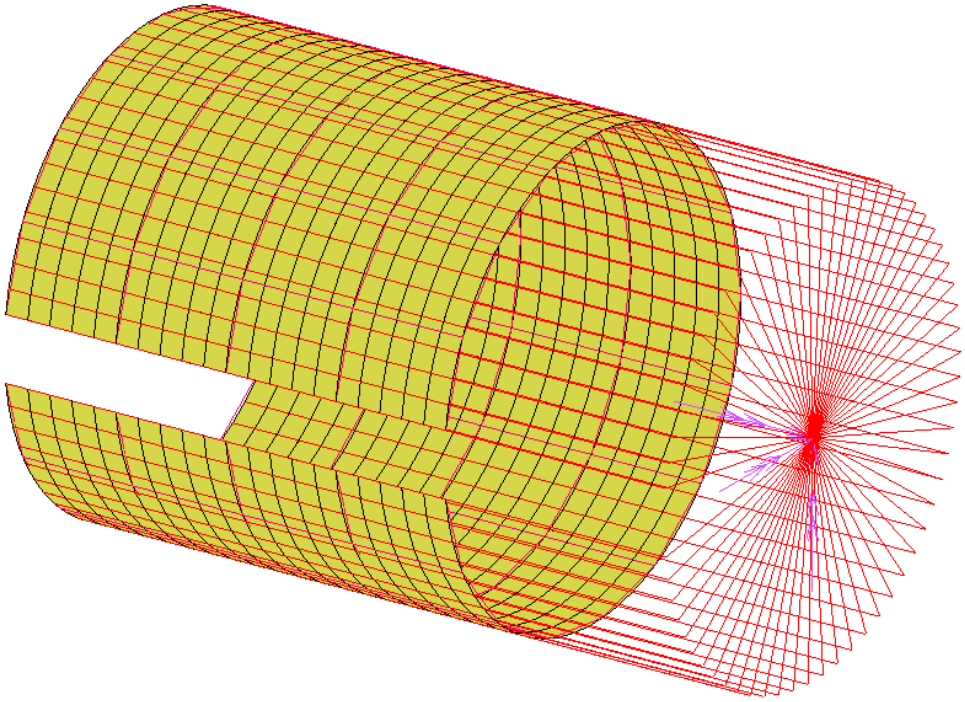

Figure 5.24: Isometric view of the 2D shell model

All material properties and laminate stacking sequences are kept identical to those used in the corresponding 3D simulations.

In particular, the laminated shell is defined by assigning a layered composite section to the shell elements. Although the shell formulation represents the structure through a single midsurface, the full through–thickness material description is retained internally by the shell element through a set of virtual layers. The visible geometry therefore corresponds to the midsurface located at the mean radius of the laminate.

5.6.2 Shell discretisation and kinematics

The three-dimensional solid discretisation based on HEX20 elements is replaced by a two-dimensional shell mesh. Each shell element carries the standard shell kinematic variables, namely membrane strains, bending curvatures, and transverse shear strains, consistently with the shell theory adopted by the finite element solver. Each node of the shell elements possesses six degrees of freedom, namely three

translational components (u_x, u_y, u_z) and three rotational components $(\theta_x, \theta_y, \theta_z)$ associated with the rotation of the shell normal. This kinematic description allows the element formulation to capture membrane deformation, bending effects, and transverse shear behaviour within a unified framework.

As a consequence, the shell model provides direct access to:

- in-plane strain components,
- bending curvatures,
- sectional forces and moments,

while the transverse normal stress component σ_{33}, i.e. the interlaminar stress, is *not* available as a direct output of the shell analysis.

This intrinsic limitation of shell formulations motivates the need for a dedicated post-processing procedure capable of reconstructing interlaminar stresses from shell-level quantities.

5.6.3 Boundary conditions and periodicity constraints

As in the three-dimensional reference model, kinematic coupling constraints (RBE2 elements) are introduced in the shell model. These constraints connect the nodes located along the circumferential edges of the ring segment to a master node and enforce a periodic-like behaviour of the structure.

The use of RBE2 elements ensures a consistent transfer of rotations and moments, prevents spurious rigid-body motions, and allows the shell model to reproduce the same global deformation mode observed in the 3D configuration.

5.6.4 Loading strategy in the shell model

Unlike the three-dimensional case, where a spatially varying pressure (field-defined butterfly bending load) is applied on the solid faces, the shell model is loaded through an equivalent nodal moment.

Specifically, a bending moment is applied to the nodes along the opening edges of the shell model, acting about the cylindrical axis of the ring. This moment is designed to reproduce, in an equivalent energetic sense, the bending state induced by the butterfly load in the three-dimensional model.

The procedure adopted to determine the correct magnitude of the equivalent nodal moment, and its relation to the curvature κ_{22} used as input for the interlaminar stress recovery, is described in detail in Section 5.7.

5.6.5 Implications for interlaminar stress recovery

Because the shell model does not provide σ_{33} directly, the evaluation of interlaminar stresses necessarily relies on a post-processing step.

The shell analysis supplies the kinematic quantities (strains and curvatures), from which the relevant master variables (e.g. κ_{22}) are extracted. These quantities are then used as inputs to the recovery procedure developed in Chapter 4, which reconstructs the full through–thickness stress field, including the interlaminar stress component.

This modelling level therefore represents the most relevant and challenging application of the proposed method, as it reflects the typical industrial use of shell finite element models for composite structures, where interlaminar stresses are not directly accessible but are often critical for damage and delamination assessment.

5.7 Equivalent loading and curvature transfer from 3D to shell models

The transition from three-dimensional solid models to two-dimensional shell formulations requires particular care in the definition of equivalent loading conditions. While geometry and material properties can be directly transferred, the applied loads must be reformulated in order to reproduce in the shell model a deformation state consistent with the reference 3D solution.

In the present work, the three-dimensional model is subjected to a distributed pressure field applied on the faces delimiting the angular opening of the ring segment, generating a pure bending condition commonly referred to as a *butterfly bending load*. This pressure distribution produces a well-defined bending state in the solid model, characterized by a specific curvature field.

In contrast, the shell formulation does not admit an equivalent pressure-based representation of this loading configuration. Bending in the shell model must instead be induced by applying nodal moments along the shell edges. As a consequence, a direct force-based equivalence between the two models is neither straightforward nor physically meaningful.

The solid and shell models differ in their kinematic assumptions, stress representations, and load transfer mechanisms. Therefore, imposing identical pressures or forces would not generally lead to the same deformation state. For this reason, the equivalence between the three-dimensional and shell models is established in terms of *curvature*, rather than force.

The key quantity governing the bending response is the curvature component κ_{22}, which controls the through-thickness stress distribution and directly enters the interlaminar stress recovery procedure developed in Chapter 4. The objective of this section is thus to determine an equivalent shell loading that reproduces, as closely as possible, the same bending curvature κ_{22} observed in the three-dimensional reference solution.

To this end, an analytical approach is adopted. Starting from the distributed pressure field applied in the 3D model, the resulting global bending moment is evaluated by integrating the pressure over the loaded surfaces. This moment is then converted into an equivalent nodal bending moment per unit length and applied along the shell edges. The procedure provides a physically consistent mapping between the distributed pressure in the solid model and the concentrated bending action in the shell formulation.

Once curvature equivalence is achieved, the shell model can be reliably used for the subsequent interlaminar stress reconstruction. Although the shell formulation does not directly provide the transverse normal stress σ_{33}, the correct reproduction of the curvature field ensures that the bending-driven stress state is consistently transferred from the three-dimensional reference configuration.

5.7.1 Curvature-based equivalence: analytical evaluation of the nodal bending moment

As a first step towards the definition of an equivalent shell loading, a direct analytical procedure is employed to estimate the nodal bending moment corresponding to the distributed pressure applied in the three-dimensional reference model.

The objective of this approach is to compute an equivalent resultant bending moment that reproduces, in an average sense, the bending effect of the radial pressure field acting on the 3D solid. This moment is then redistributed to the shell model in the form of nodal moments applied along the opening edges.

Radial pressure distribution in the 3D model.

In the three-dimensional configuration, bending is induced by a spatially varying radial pressure applied on the faces delimiting the angular opening of the ring segment. The pressure varies linearly along the radial direction and can be written as

$$p(r) = 2\,p_0\,(r - r_{\mathrm{ref}}),$$

where p_0 is the reference pressure magnitude and r_{ref} denotes a reference radius. In the present case, $r_{\mathrm{ref}} = 1$ mm corresponds to the mean radius of the laminate.

Resultant bending moment due to the pressure field.

The local contribution to the bending moment generated by the pressure acting on an infinitesimal radial strip of width $\mathrm{d}r$ is given by

$$\mathrm{d}M = p(r)\, L\, r\, \mathrm{d}r,$$

where L is the axial length of the ring segment and r represents the moment arm with respect to the cylindrical axis.

The total bending moment generated by the pressure distribution is obtained by integrating over the radial domain of the laminate:

$$M_{\mathrm{tot}} = \int_{r_{\mathrm{int}}}^{r_{\mathrm{ext}}} p(r)\, L\, r\, \mathrm{d}r.$$

Substituting the expression of $p(r)$ yields

$$M_{\mathrm{tot}} = 2p_0 L \int_{r_{\mathrm{int}}}^{r_{\mathrm{ext}}} (r - r_{\mathrm{ref}})\, r\, \mathrm{d}r,$$

which can be evaluated analytically or numerically, depending on the chosen level of approximation. In the present implementation, numerical integration is adopted to ensure robustness and flexibility with respect to geometry and loading parameters.

Distribution of the bending moment to shell nodes.

The shell model represents the opening edges through a finite number of nodes, which are connected to a master node by kinematic coupling constraints. Let N_{nodes} denote the number of active shell nodes along the loaded edge.

The total bending moment is therefore converted into an equivalent nodal moment as

$$M_{\mathrm{node}} = \frac{M_{\mathrm{tot}}}{N_{\mathrm{nodes}}}.$$

This nodal moment is applied uniformly to the shell edge nodes, acting about

the cylindrical axis of the ring. The resulting shell deformation is thus dominated by bending, in analogy with the three-dimensional reference configuration.

Role of the analytical estimate.

The analytically derived nodal moment provides a physically meaningful and computationally inexpensive estimate of the shell loading. It captures the correct order of magnitude of the bending action and serves as an initial guess for subsequent refinement.

Once the shell analysis is performed under this loading condition, the resulting in-plane strains at the inner and outer shell layers are extracted. From these quantities, the bending curvature component κ_{22} is evaluated using the strain-based procedure described in Section 5.3 and based on the approach proposed by Strozzi.

The computed curvature is then used as input to the interlaminar stress recovery procedure developed in Chapter 4, allowing the reconstruction of the through–thickness stress component σ_{33}.

This section presents the final validation of the proposed interlaminar stress recovery framework when applied to two-dimensional shell finite element models.

The shell loading considered in the following is the analytically derived equivalent bending moment introduced in Section 5.7. The applied nodal moment is obtained from the distributed pressure field acting in the three-dimensional reference model and ensures curvature consistency between the solid and shell formulations. No additional modelling assumptions are introduced here.

The focus of the present section is therefore exclusively on the *results* obtained from the shell simulations and on their comparison with the three-dimensional solid FEM reference solution.

Although the proposed methodology has been applied to both isotropic (aluminium) and composite (CFRP) configurations, the detailed discussion of results is restricted to the aluminium laminate case for the sake of clarity and conciseness. The physical mechanisms governing curvature transfer, strain-based curvature ex-

traction, and interlaminar stress recovery are identical for both material systems. As demonstrated in the previous validation sections, the relative error levels observed for the composite configurations are of the same order of magnitude as those obtained for the isotropic case. A separate discussion of the CFRP results would therefore be largely redundant and would not provide additional insight into the performance of the proposed framework.

The validation procedure follows the sequence: (i) shell FEM analysis under analytically derived equivalent bending loading, (ii) extraction of in-plane strains ε_{22} at the laminate surfaces, (iii) curvature evaluation via the Strozzi-based formulation, and (iv) reconstruction of the interlaminar normal stress σ_{33} through the recovery code developed in Chapter 4.

This section represents the final step of the proposed methodology, as it demonstrates that accurate interlaminar stress predictions can be obtained starting from shell models alone, provided that curvature equivalence with the three-dimensional reference configuration is properly enforced.

5.7.2 Shell model with analytically derived nodal moment

The first shell simulation is performed by applying a nodal bending moment derived using the analytical procedure described in Section 5.7.1. The method is based on the computation of an equivalent bending moment generated by the radial pressure distribution acting in the three-dimensional model.

For the present case, the geometric parameters of the structure are $r_{\text{int}} = 0.5$ mm, $r_{\text{ext}} = 1.5$ mm, and an axial length $L = 2$ mm. The applied butterfly-type bending load is defined by a peak radial pressure $p_0 = 1000$ N/mm^2. Using the analytical formulation, the resulting equivalent nodal bending moment to be applied at the shell edge is found to be

$$M_{\text{node}}^{\text{analytical}} = 16.6667 \text{ N mm}.$$

Once this moment is applied, the shell finite element analysis is carried out. The in-plane strain component ε_{22} is extracted at the inner and outer surfaces of the laminate, far from the opening edges, in order to minimise local end effects (Fig. 5.25 and Fig. 5.26).

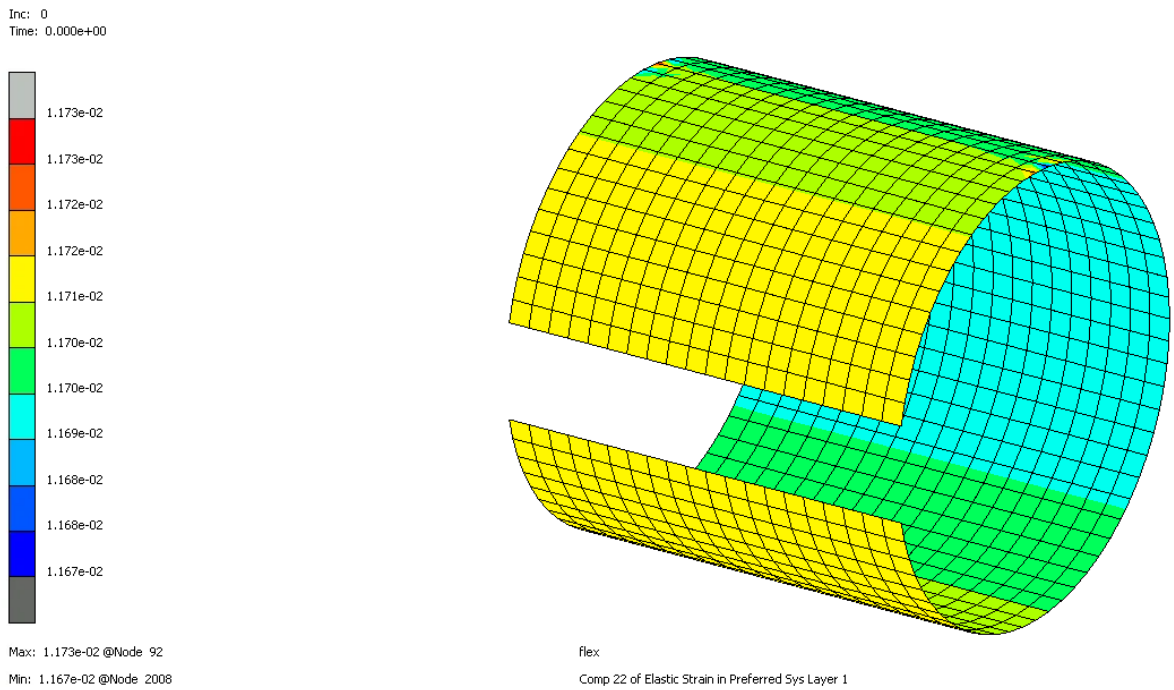

Figure 5.25: Distribution of the in-plane strain component ε_{22} at the inner laminate surface (Layer 1) obtained from the two-dimensional shell finite element model under analytically derived equivalent nodal bending moment loading.

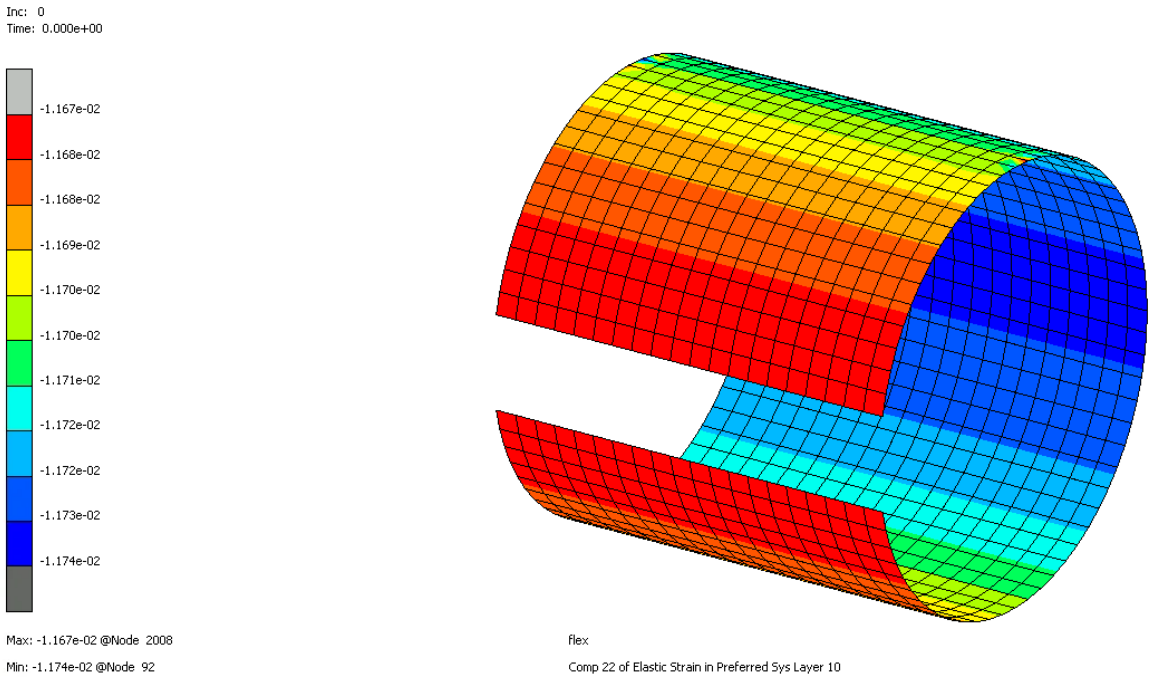

Figure 5.26: Distribution of the in-plane strain component ε_{22} at the outer laminate surface (Layer 10) obtained from the two-dimensional shell finite element model under analytically derived equivalent nodal bending moment loading.

The resulting strain values are:

$$\varepsilon_{22}^{\text{int}} = 1.170 \times 10^{-2}, \qquad \varepsilon_{22}^{\text{ext}} = -1.174 \times 10^{-2}.$$

Minor spatial variations in the strain field are observed, particularly in the upper region of the model. These variations are attributed to local numerical irregularities and do not affect the global bending response, which remains dominated by curvature.

The bending curvature is then computed using the Strozzi approach, leading to

$$\kappa_{22}^{\text{analytical}} = -2.577344 \times 10^{-2}\ \text{mm}^{-1}.$$

This curvature is provided as input to the interlaminar stress recovery procedure. The resulting through-thickness stress distribution $\sigma_{33}(z)$ exhibits a peak magnitude

of approximately

$$|\sigma_{33}^{\max}| \approx 282 \text{ MPa},$$

with the peak located close to the neutral radius, as shown in Fig. 5.27.

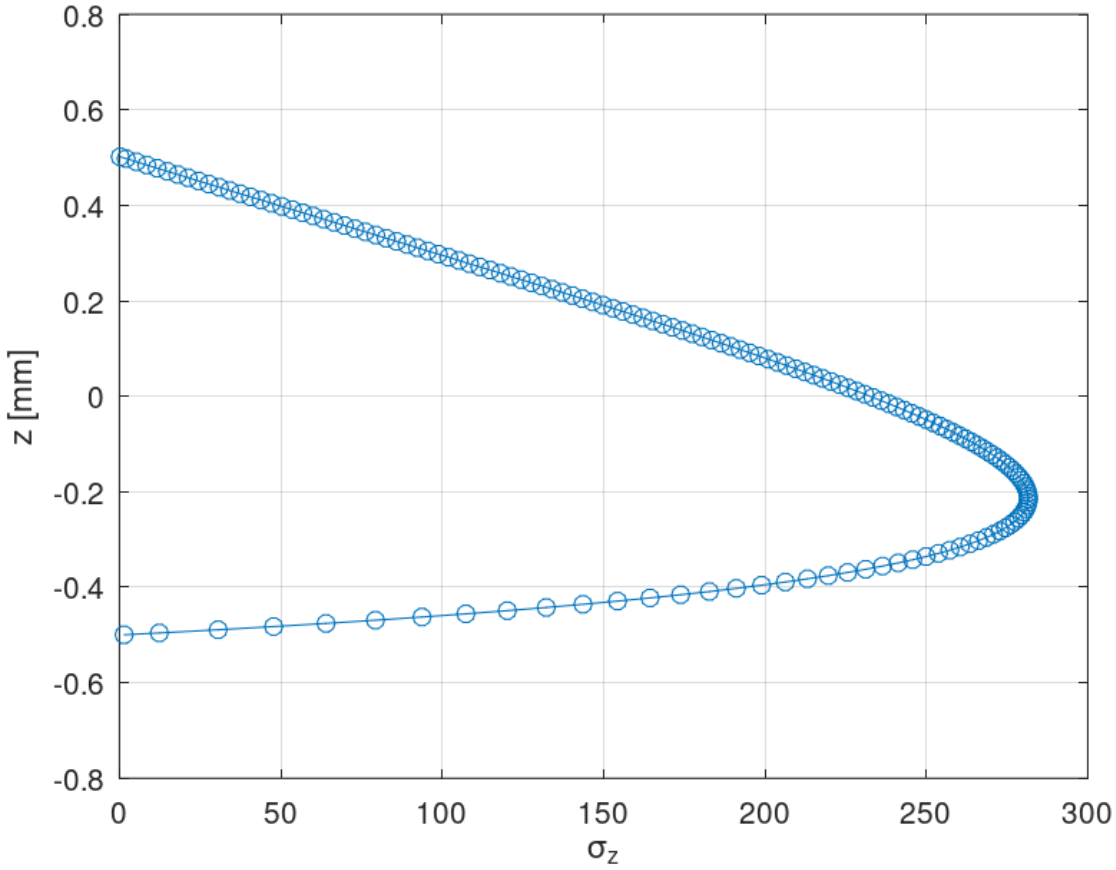

Figure 5.27: Through-thickness distribution of the interlaminar normal stress σ_{33} reconstructed from the two-dimensional shell finite element solution using the proposed recovery procedure, for the case of analytically derived equivalent nodal bending moment loading.

Although the recovered stress profile is physically consistent and exhibits the correct shape, the peak magnitude is lower than that predicted by the three-dimensional FEM reference, suggesting that the analytical moment underestimates the effective bending action experienced by the structure.

5.7.3 Comparison with 3D FEM and error assessment

The reference three-dimensional solid FEM analysis predicts a peak interlaminar stress, as shown in Section 5.4.1, of approximately

$$|\sigma_{33}^{\max,3D}| \approx 300 \text{ MPa}.$$

The peak value obtained from the shell-based recovery procedure, employing the analytically derived equivalent bending moment, is

$$|\sigma_{33}^{\max,\text{shell}}| \approx 282 \text{ MPa}.$$

The corresponding relative error is computed as

$$\text{Error}_{\text{shell}} = \frac{|282 - 300|}{300} \times 100 \approx 6.0\%.$$

A global comparison of the through–thickness stress distributions is shown in Fig. 5.28. For consistency with the previous validation results, all curves are reported in normalised form, with the interlaminar normal stress σ_{33} scaled by the reference circumferential stress σ_{22} extracted from the three–dimensional FEM model and reported in Section 5.4.1.

Three curves are presented: the direct σ_{33} distribution obtained from the 3D FEM model, the validation curve obtained by directly feeding the 3D-derived curvature into the recovery code, and the shell-based result obtained using the analytically derived equivalent nodal bending moment.

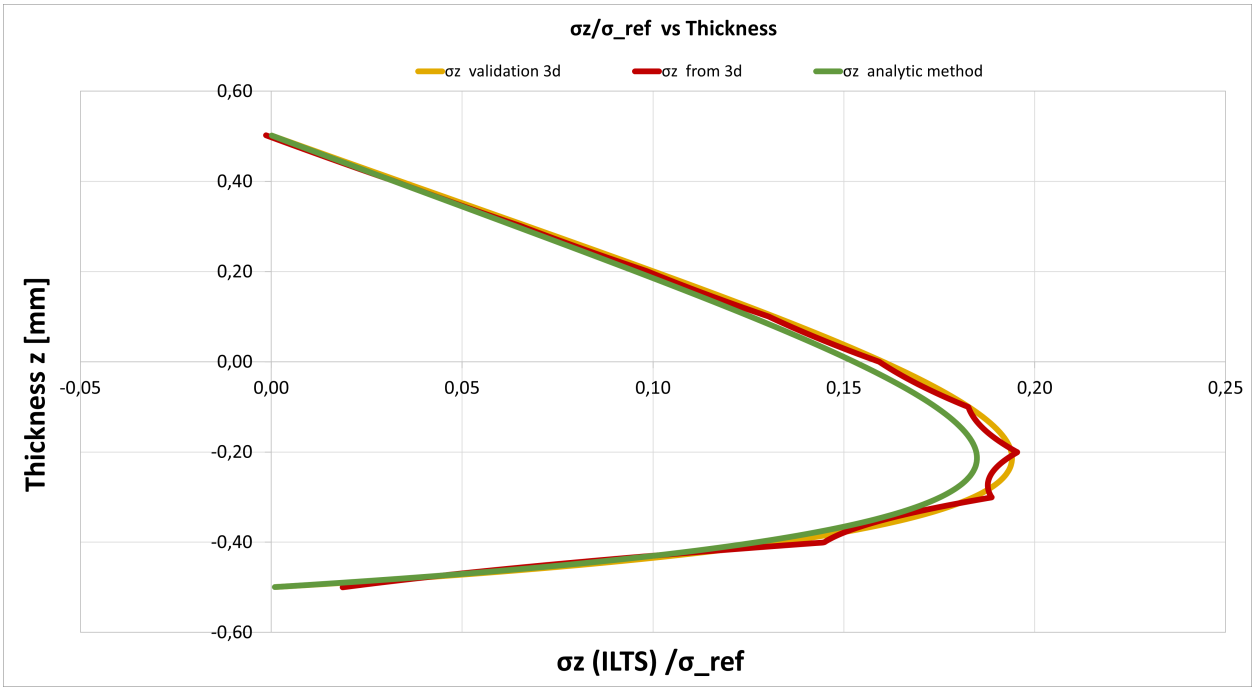

Figure 5.28: Normalised comparison of the through–thickness interlaminar normal stress σ_{33} distributions. Results are shown for the three-dimensional solid FEM reference solution, the direct 3D-based validation recovery, and the shell-based recovery approach employing analytically derived equivalent nodal bending moments.

The shell-based curve shows good agreement with the 3D reference solution over the entire thickness, accurately reproducing the overall shape of the stress distribution. A moderate underestimation of the peak interlaminar stress is observed, which remains within a relative error of approximately 6%. Considering the reduced kinematic description inherent to shell models and the indirect nature of the stress reconstruction procedure, this level of accuracy confirms the robustness of the analytical curvature-based loading transfer and the reliability of the proposed recovery framework.

5.8 Moment-driven post-processing formulation

The analytical shell-based validation highlighted that the residual discrepancy with respect to the three-dimensional reference solution was mainly associated with the curvature extraction step from the FEM strain field. Although curvature-driven input provides reliable results, it still requires a prior finite element solution and

introduces a secondary reconstruction layer.

For this reason, the post-processing framework has been reformulated in a fully moment-driven configuration. Instead of prescribing the curvature component κ_{22} extracted from FEM strains, the bending moment per unit length M_{22} is directly imposed as mechanical input. The curvature and all associated generalized deformations are then computed internally through the laminate constitutive equations.

The implementation of this part is fully available in Appendix B.

Generalized laminate system

At laminate level, the constitutive relation is written in compact form as

$$\mathbf{R} = \mathbf{K}\,\mathbf{d}_m, \tag{5.1}$$

where

$$\mathbf{d}_m = \begin{bmatrix} \varepsilon_{11} \\ \varepsilon_{22} \\ \varepsilon_{12} \\ \kappa_{11} \\ \kappa_{22} \\ \kappa_{12} \end{bmatrix}, \qquad \mathbf{R} = \begin{bmatrix} N_{11} \\ N_{22} \\ N_{12} \\ M_{11} \\ M_{22} \\ M_{12} \end{bmatrix}.$$

The vector $\mathbf{d}_m$ contains the master membrane strains and curvatures of the laminate, while $\mathbf{R}$ collects the corresponding membrane forces and bending moments per unit length. The matrix $\mathbf{K}$ is the reduced laminate stiffness matrix computed from the stacking sequence and material properties (stored in the implementation as `o.rKmat`).

Input definition and use of `NaN`

In the moment-driven configuration, only the circumferential bending moment per unit length M_{22} is prescribed:

$$M_{22} = M_{22}^{\text{input}}.$$

All other generalized resultants are left unspecified. In the numerical implementation, this is achieved by assigning the value `NaN` (Not-a-Number) to the corresponding components of the resultant vector.

The use of `NaN` has a precise algebraic meaning: it identifies degrees of freedom that are not explicitly constrained and therefore must be determined consistently by the constitutive system.

Accordingly, the deformation vector is initialized as

$$\mathbf{d}_m = \begin{bmatrix} \text{NaN} \\ \text{NaN} \\ 0 \\ 0 \\ \text{NaN} \\ 0 \end{bmatrix},$$

which reflects cylindrical bending conditions:

- $\varepsilon_{12} = 0$,
- $\kappa_{11} = 0$,
- $\kappa_{12} = 0$,

while ε_{11}, ε_{22} and κ_{22} are treated as unknowns.

The resultant vector is defined as

$$\mathbf{R} = \begin{bmatrix} 0 \\ 0 \\ \text{NaN} \\ \text{NaN} \\ M_{22} \\ \text{NaN} \end{bmatrix},$$

so that only the bending moment component is explicitly imposed.

Partitioned solution of the linear system

The global system

$$\mathbf{K}\mathbf{d}_m = \mathbf{R} \tag{5.2}$$

is solved by separating constrained and free components. Let the indices f denote entries marked as `NaN` in $\mathbf{d}_m$, and v those explicitly assigned.

The partitioned system reads

$$\begin{bmatrix} \mathbf{K}_{ff} & \mathbf{K}_{fv} \\ \mathbf{K}_{vf} & \mathbf{K}_{vv} \end{bmatrix} \begin{bmatrix} \mathbf{d}_{m,f} \\ \mathbf{d}_{m,v} \end{bmatrix} = \begin{bmatrix} \mathbf{R}_f \\ \mathbf{R}_v \end{bmatrix}.$$

The unknown master variables are obtained as

$$\mathbf{d}_{m,f} = \mathbf{K}_{ff}^{-1} \left(\mathbf{R}_f - \mathbf{K}_{fv} \mathbf{d}_{m,v} \right). \tag{5.3}$$

This corresponds exactly to the algebraic operation implemented in the code:

```
x(ixf) = inv(A(ixf,ixf))*(b(ixf) - A(ixf,ixv)*x(ixv));
```

After solution, the full vector $\mathbf{d}_m$ is completely defined. In particular, the curvature component κ_{22} is not imposed, but emerges naturally as the constitutively consistent response of the laminate to the applied bending moment M_{22}.

Importantly, the procedure determines the entire set of master deformation variables, not only κ_{22}. Any membrane strains arising from bending–membrane coupling effects are automatically included.

Reconstruction of the complete generalized DOFs

The recovery framework operates on a larger set of generalized kinematic degrees of freedom collected in the vector $\mathbf{d}_g$. These are reconstructed from the master variables through the linear mapping

$$\mathbf{d}_g = \mathbf{L}_{dg,dm}\, \mathbf{d}_m, \tag{5.4}$$

where $\mathbf{L}_{dg,dm}$ is a transformation matrix defined in the implementation (stored as `o.L_dg_dm`).

Numerically, this corresponds to

```
dg = o.L_dg_dm * dm;
```

This step embeds the laminate-level membrane strains and curvatures into the complete kinematic description required for the through-thickness strain evaluation.

Final stress reconstruction

Once $\mathbf{d}_g$ is obtained, the full through-thickness strain distribution is evaluated according to the kinematic relations of the model. The interlaminar normal stress $\sigma_{33}(z)$ is then reconstructed exactly as described in Chapter 4.

Methodological implications

The moment-driven formulation provides a fully intrinsic pathway:

$$M_{22} \longrightarrow \mathbf{d}_m \longrightarrow \mathbf{d}_g \longrightarrow \sigma_{33}(z).$$

No curvature extraction from finite element strains is required. The curvature κ_{22} and all associated deformation components are obtained directly from laminate constitutive theory.

As a consequence, the post-processing framework becomes independent of any prior FEM solution and fully driven by the applied mechanical resultant. This represents a conceptually cleaner and mechanically consistent formulation of the interlaminar stress recovery procedure.

5.8.1 Comparative assessment: curvature-driven vs moment-driven input

This subsection presents a comprehensive comparison of the interlaminar stress distributions obtained for three representative configurations: isotropic aluminium, CFRP laminate, and antisandwich laminate. For each case, three approaches are compared:

- Direct 3D FEM solution (reference);
- Curvature-driven recovery (input κ_{22});
- Moment-driven recovery (input M_{22});

For the aluminium case, the shell solution obtained using the analytical curvature transfer is also shown.

All curves are reported in normalised form, with σ_{33} scaled by the maximum circumferential stress $\sigma_{22}^{\max}$ extracted from the 3D FEM model.

Aluminium laminate

Figure 5.29 shows the comparison for the aluminium case.

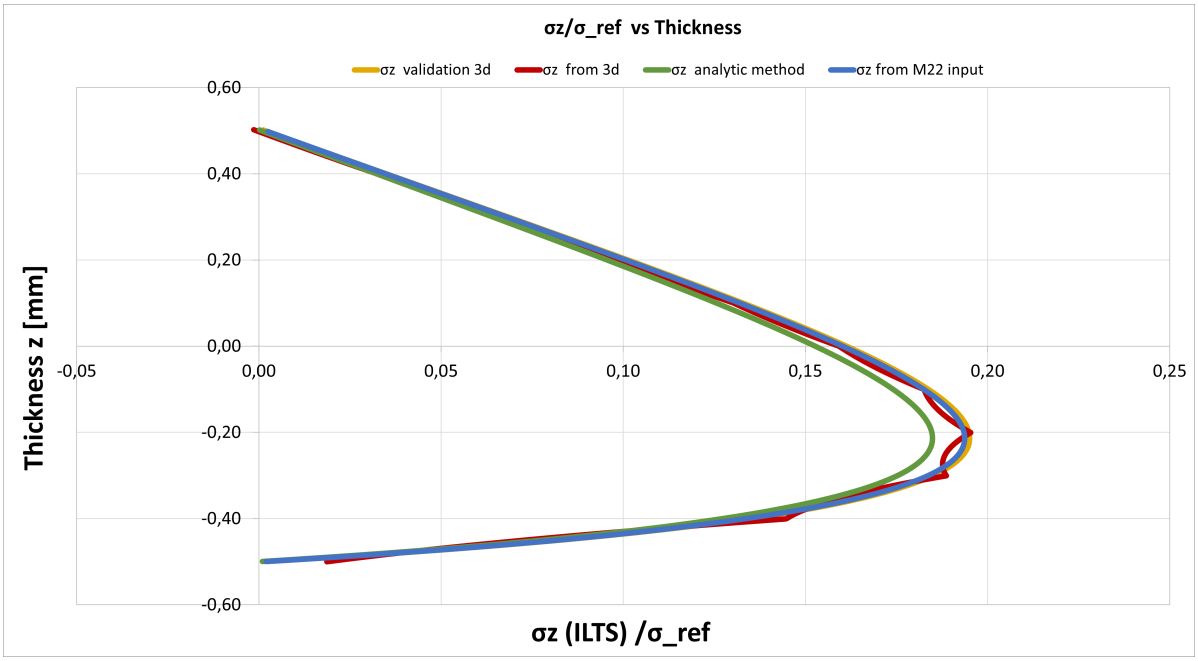

Figure 5.29: Aluminium case: comparison between 3D FEM, curvature-driven recovery, analytical shell approach, and moment-driven recovery.

The three principal curves (3D FEM, κ_{22} input, and M_{22} input) are practically superposed. The peak interlaminar stress corresponds to approximately

$$\sigma_{33}^{\max} \approx 0.19\,\sigma_{22}^{\max}.$$

The moment-driven formulation reproduces exactly the same peak level and stress distribution shape obtained from both the FEM reference and the curvature-driven approach. The analytical shell-based solution also follows the same trend, with only minor local deviations previously discussed.

The agreement confirms that, for homogeneous laminates without strong coupling effects, prescribing the bending moment directly yields a constitutively consistent curvature and therefore an identical interlaminar stress field.

CFRP laminate

Figure 5.30 reports the CFRP case.

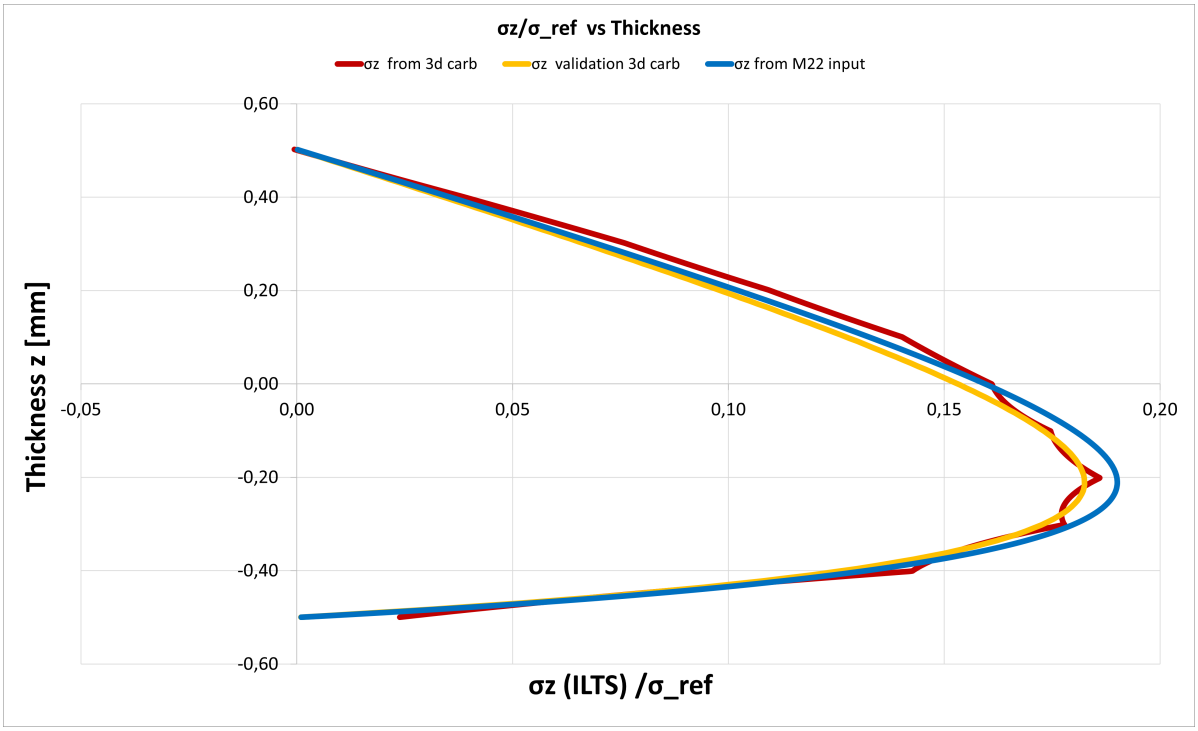

Figure 5.30: CFRP case: comparison between 3D FEM, curvature-driven recovery and moment-driven recovery.

In this configuration, the peak interlaminar stress levels are:

$$\begin{aligned} \text{Curvature-driven:} \quad & 0.18\,\sigma_{22}^{\max}, \\ \text{3D FEM:} \quad & 0.19\,\sigma_{22}^{\max}, \\ \text{Moment-driven:} \quad & 0.195\,\sigma_{22}^{\max}. \end{aligned}$$

The three solutions differ by approximately 1%, which is within the expected numerical tolerance associated with discretisation and post-processing reconstruction.

The moment-driven approach slightly overestimates the peak stress, while the curvature-driven solution slightly underestimates it. However, the global shape and thickness-wise distribution remain essentially identical.

This confirms that, even in anisotropic laminates where bending–membrane coupling effects may arise, the direct imposition of M_{22} produces a deformation state

that is fully coherent with the FEM solution.

Antisandwich laminate

The antisandwich configuration, shown in Figure 5.31, confirms the robustness of the proposed moment-driven formulation even for strongly heterogeneous laminates.

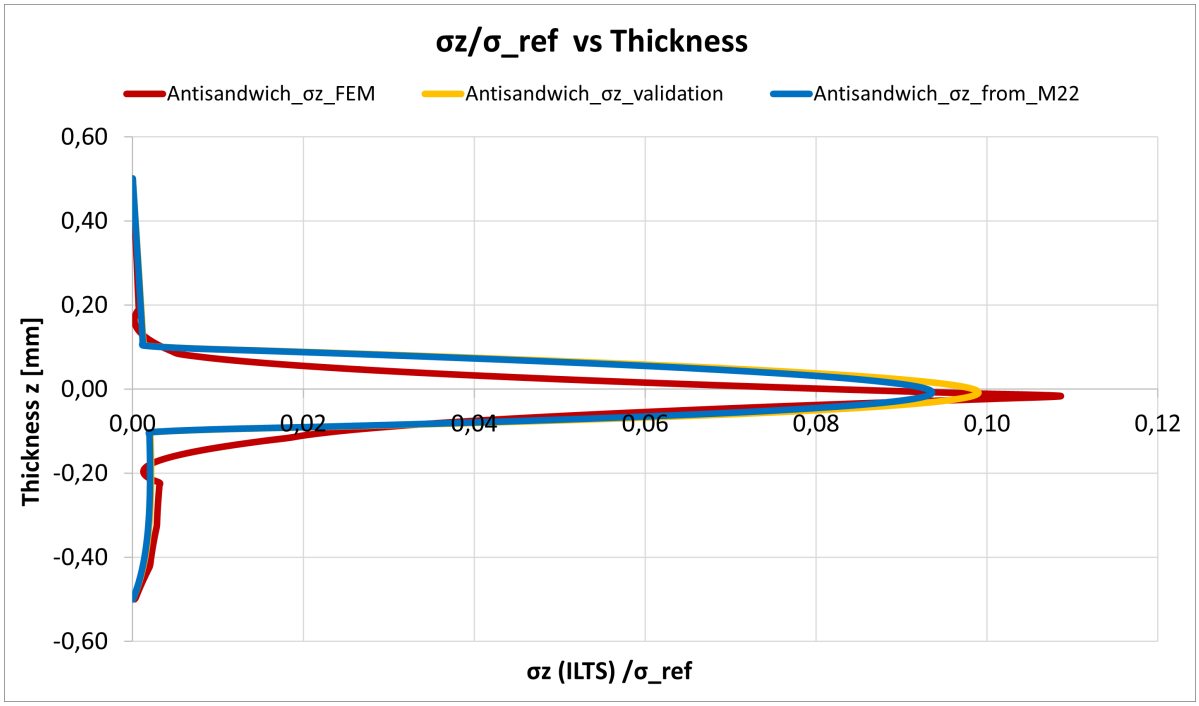

Figure 5.31: Antisandwich case: comparison between 3D FEM, curvature-driven recovery and moment-driven recovery.

All three curves exhibit very similar through-thickness distributions, with consistent shape and peak location. The maximum interlaminar normal stress levels are:

$$\begin{aligned} \text{Moment-driven:} \quad & 0.09\,\sigma_{22}^{\max}, \\ \text{Curvature-driven:} \quad & 0.10\,\sigma_{22}^{\max}, \\ \text{3D FEM:} \quad & 0.11\,\sigma_{22}^{\max}. \end{aligned}$$

The maximum discrepancy between the three approaches is therefore approximately 2%, which remains fully acceptable from both a structural and numerical

standpoint.

It is worth noting that, compared to the aluminium and CFRP cases, the antisandwich laminate develops significantly lower interlaminar normal stresses relative to the circumferential stress level. This behaviour is mechanically consistent with the presence of a strongly heterogeneous through-thickness stiffness distribution. The compliant core and stiff outer layers redistribute bending effects in such a way that interlaminar normal stresses are reduced relative to the global bending stress.

Despite the strong stiffness contrast across the thickness, the moment-driven formulation remains fully consistent with the curvature-driven recovery and the 3D FEM reference. This confirms that the reduced laminate constitutive representation accurately captures the effective bending response of the antisandwich structure in the present loading configuration.

From a methodological perspective, this result is particularly relevant. The antisandwich configuration represents the most mechanically complex case among those analysed, due to the pronounced material heterogeneity. The excellent agreement observed here demonstrates that the direct moment-to-curvature mapping embedded in the laminate stiffness matrix is sufficient to reproduce the interlaminar stress field without requiring curvature extraction from finite element strains.

Global interpretation

Across all three configurations (aluminium, CFRP and antisandwich), the moment-driven formulation consistently reproduces the interlaminar stress distributions obtained from both the 3D FEM reference and the curvature-driven recovery.

The relative discrepancies remain within 1% for aluminium and CFRP, and within 2% for the antisandwich case. Such deviations fall well within typical modelling tolerances and do not affect structural assessment conclusions.

These results confirm that the proposed moment-driven post-processing strategy provides:

- Mechanical consistency with laminate constitutive theory,
- Numerical stability across homogeneous and heterogeneous stacking sequences,
- Independence from finite element strain extraction,
- Accurate prediction of interlaminar normal stresses.

The framework can therefore be considered fully validated for the range of configurations analysed in this study.

5.9 Discussion of results

The results presented in this chapter provide a comprehensive assessment of the proposed interlaminar stress recovery framework when applied to two-dimensional shell finite element models and, more generally, to laminate-level constitutive representations.

The primary outcome of this study is that interlaminar normal stresses σ_{33} can be reconstructed with high accuracy starting from reduced kinematic descriptions. Although classical shell formulations do not directly provide through-thickness stress components, the proposed recovery strategy demonstrates that this limitation is not fundamental. When the bending state is correctly represented at laminate level, the interlaminar stress field can be consistently reconstructed.

A key aspect emerging from the validation process is the central role of curvature consistency. Initially, curvature κ_{22} was extracted from finite element strain fields and used as input for the recovery code. This curvature-driven approach already yielded excellent agreement with the three-dimensional FEM reference solution across all tested configurations.

However, in order to remove any dependency on strain extraction from finite element models, the post-processing framework was further modified. Instead of prescribing κ_{22}, the bending moment per unit length M_{22} is now directly imposed

as input. The complete set of laminate generalized deformations is then obtained by solving the reduced constitutive system

$$\mathbf{R} = \mathbf{K}\mathbf{d}_m,$$

and the curvature component κ_{22} emerges naturally as part of the solution.

This modification represents a conceptual improvement of the framework. The interlaminar stress recovery becomes fully driven by mechanical resultants rather than by quantities extracted from a numerical model. As a consequence, the method is no longer dependent on any prior FEM simulation for curvature evaluation.

The comparative results confirm the validity of this reformulation. For the aluminium and CFRP laminates, the moment-driven and curvature-driven approaches reproduce the 3D FEM reference with relative discrepancies below 1%. Not only the peak stress values, but also the complete through-thickness distributions are accurately captured.

The antisandwich configuration further demonstrates the robustness of the method. Despite the strong stiffness heterogeneity across the thickness, all three approaches (3D FEM, curvature-driven and moment-driven) remain closely aligned, with differences limited to approximately 2%. Moreover, the interlaminar stresses remain significantly lower than the maximum circumferential stress σ_{22}, confirming the mechanical consistency of the predicted bending response.

Across all cases, the normalised peak interlaminar stresses remain within a narrow band relative to $\sigma_{22}^{\max}$: approximately 19% for aluminium, 19–19.5% for CFRP, and 9–11% for the antisandwich laminate. Such consistency confirms that the proposed framework correctly captures the relative interlaminar stress mechanisms driven by bending, independently of material system or stiffness contrast.

From a broader perspective, the most significant outcome of this work is methodological. Accurate interlaminar stress predictions, traditionally associated with computationally expensive three-dimensional solid models, can be obtained from a re-

duced laminate-level formulation through a physically consistent recovery procedure. The moment-driven reformulation further strengthens this result by removing the need for curvature extraction from finite element strains.

This opens important practical perspectives. Shell-based analyses, which are computationally efficient and widely used in industrial applications, can now be coupled with a reliable interlaminar stress reconstruction tool. This enables early-stage design studies, parametric analyses, and large-scale simulations where full 3D solid modelling would be computationally prohibitive.

Finally, it is worth emphasising that the methodology is general and not restricted to the specific geometries or materials investigated here. The framework relies solely on laminate constitutive relations and kinematic consistency. Provided that the global bending moment is known, the complete interlaminar stress distribution can be reconstructed without resorting to three-dimensional finite element models. This makes the approach particularly attractive for structural assessment, damage prediction, and optimisation of curved laminated components in advanced engineering applications.

Chapter 6

Conclusions and Outlook

6.1 Summary of the proposed methodology

This thesis has addressed the problem of recovering interlaminar tensile stresses (ILTS) in curved laminated composite structures analysed using reduced–order finite element models. While two–dimensional shell formulations represent the standard choice in industrial practice due to their favourable balance between accuracy and computational efficiency, they are intrinsically unable to directly provide through–thickness stress components, which govern the initiation of delamination.

To overcome this limitation, a physically consistent post–processing framework has been developed for the reconstruction of the interlaminar normal stress distribution $\sigma_{33}(z)$ starting from reduced shell solutions or from three–dimensional strain information. The proposed approach departs from conventional force– or moment–equivalence strategies and is instead grounded on a curvature–based description of bending in curved laminates, inspired by classical curved beam theory and extended to layered anisotropic configurations.

The central concept of the methodology is the enforcement of *curvature consistency* between a reference three–dimensional solid model and a reduced representation. The bending state is initially characterised by extracting an effective circumferential curvature κ_{22} directly from the strain field, which is subsequently employed

as the master variable driving the interlaminar stress recovery. This choice allows the bending kinematics to be transferred in a manner that is independent of the specific loading representation and consistent with the actual deformation state of the structure.

In a subsequent refinement of the framework, the post–processing input strategy was further generalised. Instead of prescribing κ_{22} extracted from a finite element solution, the bending moment per unit length M_{22} is directly imposed. The complete vector of laminate generalized deformations is then obtained by solving the reduced constitutive system

$$\mathbf{R} = \mathbf{K}\mathbf{d}_m,$$

allowing the curvature component κ_{22} and all associated membrane strains to emerge naturally from the constitutive response. This reformulation makes the recovery procedure fully driven by mechanical resultants and removes any intrinsic dependency on curvature extraction from FEM strain fields.

From a numerical standpoint, the framework follows a modular workflow. The bending state is characterised either through curvature extraction from a reference strain field or through direct imposition of the bending moment per unit length. The corresponding generalized laminate deformations are then obtained within a laminate constitutive formulation in which material stiffness matrices and through–thickness kinematics are explicitly accounted for.

The original contribution of this work lies in the development of a computationally efficient ILTS recovery strategy for curved laminates that bridges rigorous shell kinematics, energetic consistency, and industrial compatibility. The methodology provides a direct pathway to obtain interlaminar stress fields comparable to full three–dimensional analyses while retaining the computational advantages of shell finite element models.

The entire procedure has been implemented in a dedicated numerical code devel-

oped in Octave, providing full control over material properties, stacking sequences, geometric parameters and numerical options. This implementation enables systematic validation, transparent verification of each computational step, and constitutes a robust platform for further methodological extensions and research-oriented developments.

6.2 Main findings

The results obtained in this work highlight several key aspects regarding the nature of interlaminar tensile stresses in curved laminates and the effectiveness of curvature–based recovery strategies.

First, the validation against three–dimensional solid finite element models confirms that the proposed methodology is able to accurately reconstruct the through–thickness distribution of σ_{33} for a wide range of material configurations. For moderate thickness–to–radius ratios, the reconstructed stress profiles closely follow the reference three–dimensional solutions, both in terms of peak magnitude and peak location.

In the isotropic aluminium case, the recovered stress profile is in almost perfect agreement with the reference solution, providing a clear baseline verification of the formulation in the absence of material anisotropy or stiffness discontinuities. This result confirms the theoretical consistency of the curvature-based description when applied to homogeneous curved beams.

For the quasi–isotropic CFRP laminate, the method demonstrates robust performance despite the presence of strongly orthotropic plies and multiple interfaces. The correct location and magnitude of the peak interlaminar tensile stress are reproduced, confirming that the curvature–based description remains valid in layered anisotropic systems and is not compromised by bending–extension coupling effects.

More importantly, the results obtained for heterogeneous laminates clearly highlight both the physical meaning and the domain of applicability of the adopted

curvature–driven approach.

In the sandwich configuration, characterised by stiff face sheets and a highly compliant core, the bending kinematics is governed by strong through–thickness stiffness contrasts that lead to the appearance of multiple effective neutral axes. As a consequence, the deformation state cannot be described by a single global curvature parameter. Under these conditions, the assumptions underlying the proposed post–processing strategy are no longer satisfied, and the recovered interlaminar stress distribution does not reliably reproduce the three–dimensional reference solution. The discrepancies observed are not artefacts of the recovery procedure, but reflect the intrinsic limitation of curvature–based descriptions when local three–dimensional effects dominate the structural response of the core region.

In contrast, the anti–sandwich configuration exhibits a markedly different behaviour. Although material heterogeneity is still present, the stiffer layers embedded within a more compliant matrix govern the global bending response, which remains effectively characterised by a single curvature parameter. In this case, the proposed methodology provides very good agreement with the three–dimensional reference solution across the laminate thickness, accurately capturing both the magnitude and the location of the peak interlaminar tensile stresses. This result confirms that the recovery procedure is reliable when the bending kinematics can be meaningfully represented by an effective global curvature.

A central outcome of this work concerns the refinement of the bending state transfer strategy.

The initial curvature–driven approach already demonstrated excellent agreement with the three–dimensional reference solutions. The subsequent moment–driven reformulation further strengthened the methodology by eliminating the need for curvature extraction from FEM strain fields.

For the aluminium and CFRP configurations, both curvature–driven and moment–driven approaches reproduce the 3D FEM interlaminar stress distributions with dis-

crepancies below 1%. The normalised peak ILTS values remain approximately 19% of the maximum circumferential stress for aluminium and between 19% and 19.5% for CFRP.

For the anti–sandwich configuration, all approaches remain closely aligned, with peak ILTS values between 9% and 11% of the maximum circumferential stress and discrepancies limited to approximately 2%. Despite the pronounced through–thickness stiffness heterogeneity, the bending state remains effectively described by a global curvature parameter, confirming the robustness of the proposed framework.

These results demonstrate that the moment–driven formulation provides a fully self–contained and mechanically consistent pathway for ILTS recovery, while preserving the accuracy of the curvature–based description.

6.3 Limitations of the present work

The proposed methodology has been formulated and validated within a well–defined domain of applicability, and its limitations should be interpreted accordingly.

The recovery framework is based on the extraction of a limited set of effective curvature components to characterise the bending state. This assumption is appropriate for the considered geometries and loading conditions, which are representative of many industrial shell applications. However, deformation states involving strong curvature gradients, significant torsional coupling, highly localised loading, or rapidly varying geometry may require an extended set of master variables and a more generalised curvature representation.

Furthermore, the reconstruction relies on a global equilibrium description across the thickness. As a consequence, purely local three–dimensional effects induced by sharp geometric discontinuities, local constraints, or extreme material stiffness contrasts cannot be fully captured. This limitation becomes evident when the structural response is governed by local mechanisms rather than by global bending kinematics.

The present study has been restricted to linear elastic material behaviour. While

this assumption is appropriate for validating the proposed framework and for assessing delamination onset, it does not account for damage evolution, interface degradation, nonlinear material response, or stiffness redistribution under service conditions. The current formulation therefore predicts stress fields but does not directly simulate progressive failure.

Finally, the validation has focused on controlled bending scenarios designed to generate well–defined curvature states. Although these configurations are representative and suitable for methodological verification, the extension to more general loading conditions, including combined mechanical loads, dynamic effects, thermal gradients, or residual stresses from manufacturing processes, remains outside the scope of the present investigation.

6.4 Future developments

The proposed framework opens several promising directions for future research and development.

A first extension concerns the generalisation to fully doubly–curved shells with spatially varying curvature fields. In such cases, multiple curvature components could be extracted and employed simultaneously, enabling the reconstruction of more complex interlaminar stress states and improving the accuracy in components with non-uniform geometry.

Another important development involves coupling the recovery procedure with progressive damage and delamination models. By linking the reconstructed interlaminar stresses to fracture mechanics criteria (such as VCCT or cohesive zone models), the framework could be extended to predict not only delamination onset but also its subsequent propagation within shell–based analyses. This integration would enable fully delamination-aware reduced-order design workflows.

From a numerical perspective, the methodology could be embedded into commercial finite element post–processing environments or implemented within user-defined

routines. Its integration into global–local strategies would allow the recovery procedure to act as an efficient screening tool for identifying critical regions requiring detailed three–dimensional analyses, thereby optimising computational resources in large-scale structural models.

A further extension concerns the recovery of interlaminar shear stresses (ILSS). Although this thesis has focused on interlaminar tensile stresses, the curvature–driven and laminate–consistent framework provides a natural basis for extending the recovery to shear components by introducing appropriate master variables associated with transverse shear deformation.

Overall, this work demonstrates that accurate and physically meaningful interlaminar stress predictions are achievable without abandoning the efficiency of shell finite element models. By combining curvature–based kinematics with laminate constitutive consistency and direct moment–driven input capability, the proposed methodology represents a significant step towards safer, more reliable, and computationally efficient design of curved composite structures.

Software and computational tools

The numerical analyses presented in this work were carried out using a combination of commercial finite element software and in-house numerical codes.

Three-dimensional and shell finite element simulations were performed using *MSC Marc/Mentat*, which was employed for geometry definition, mesh generation, material modelling, application of boundary conditions and post-processing of strain fields.

The interlaminar stress recovery procedure and all curvature-based post-processing operations were implemented through custom numerical scripts developed in *GNU Octave*. These scripts were used to extract master variables from the FEM results, compute bending curvatures according to the Strozzi approach, and reconstruct the through-thickness stress distributions.

Symbolic manipulations and verification of analytical expressions were performed using *Maxima*, while *Microsoft Excel* was used for data organisation, numerical checks and graphical comparisons.

This hybrid computational framework allowed for a flexible and efficient integration of finite element analyses with advanced post-processing and analytical validation tools.

References

This section gathers and recapitulates all the bibliographic sources cited in the different chapters of the present thesis.

- Reddy, J. N. (2003). Mechanics of laminated composite plates and shells: Theory and analysis (2nd ed.). Boca Raton, FL: CRC Press.
- Strozzi, A. (1998). *Costruzione di macchine*. Bologna, IT: Pitagora.
- Y. Huang et al., *Delamination behavior in curved laminates under flexural loading*, Composite Structures, vol. 220, 2019.
- S. W. Tsai and H. T. Hahn, *Introduction to Composite Materials*, Technomic Publishing, 1980.
- T. Gries et al., *Curved CFRP components for motorsport: Modeling and Testing *, Automotive Composites Conference, 2022.
- R. Ahmad, A. Khan, M. Z. Abdullah, "A Review of Delamination Damage of Composite Materials," *Polymers*, MDPI, vol. 15, no. 18, 2023.
- S. T. Pinho, L. Iannucci, P. Robinson, "Physically-based failure models and criteria for laminated fibre-reinforced composites with emphasis on fibre kinking. Part II: FE implementation," *Composites Part A: Applied Science and Manufacturing*, vol. 37, no. 5, pp. 766–777, 2006.

- J. Y. Cognard, “Numerical simulation of delamination in curved composite laminates using cohesive elements,” *International Journal of Adhesion and Adhesives*, vol. 29, no. 4, pp. 356–365, 2009.

- A. P. Mouritz, “Delamination in complex composite structures,” in *Introduction to Aerospace Materials*, Woodhead Publishing, 2012, pp. 264–281.

- H. Totry, O. Rabinovitch, D. Rittel, “The effects of temperature and loading mode on delamination in curved laminates,” *Journal of Composite Materials*, vol. 45, no. 15, pp. 1609–1620, 2011.

- R. Mishra, A. Das, “Recovery of interlaminar stresses in composite laminates from shell FE results,” *Composite Structures*, vol. 250, 2020.

- D. Pueyo, J. Cuartero, D. Ranz, M. Barburski, “Experimental investigation of ILTS in curved flax/epoxy laminates,” *Mechanics of Advanced Materials and Structures*, 2023.

- R. Kedward, R. Graff, “Interlaminar stresses in curved composite straps: An elastic and FEM study,” NASA Technical Report 89–1456, 1989.

- S. Fanelli, “Procedures for the Interlaminar Tensile Stress evaluation in Finite Element models,” Ph.D. Thesis, University of Modena and Reggio Emilia, 2020.

- K. Komarov, L. Petrov, A. Akhmetova, “Effect of tufting on interlaminar tensile strength of curved CFRP composites,” *Polymer Composites*, vol. 44, no. 12, 2023.

- Grankäll, T., Hallander, P., & Åkermo, M. (2021). Vacuum-Assisted Hot Forming Using Tailored Laminate Temperature. Applied Composite Materials, 28(4), 1237–1256.

- Shao, D., Hu, S., Wang, Q., & Pang, F. (2017). Free vibration of refined higher-order shear deformation composite laminated beams with general boundary conditions. Composites Part B: Engineering, 108, 75–90.

- M. Fekrmandi and A. M. Tabbakhha, *Application of Composites in Automotive Crashworthiness*, Materials Today: Proceedings, vol. 45, 2021.

- Roos, R., Kress, G., Barbezat, M., & Ermanni, P. (2007). Enhanced model for interlaminar normal stress in singly curved laminates. Composite Structures, 80(3), 327–333.

  https://doi.org/10.1016/j.compstruct.2006.05.022

- Roos, R., Kress, G., & Ermanni, P. (2007). A post-processing method for interlaminar normal stresses in doubly curved laminates. Composite Structures, 81(3), 463–470.

  https://doi.org/10.1016/j.compstruct.2006.09.016

- Maragoni, L., Carraro, P. A., & Quaresimin, M. (2018). Periodic boundary conditions for FE analyses of a representative volume element for composite laminates with one cracked ply and delaminations. Composite Structures, 201, 932–941.

  https://doi.org/10.1016/j.compstruct.2018.06.058

- Cao, Y., Feng, Y., Xue, X., Wang, W., & Bai, L. (2017). Evaluation of interlaminar stresses in composite laminates with a bolt-filled hole using a linear elastic traction-separation description. Applied Sciences, 7(1), 93.

  https://doi.org/10.3390/app7010093

- Whitney, J. M., & Pagano, N. J. (1970). Shear deformation in heterogeneous anisotropic plates. Journal of Applied Mechanics, 37(4), 1031–1036.

  https://doi.org/10.1115/1.3408654

- Mao, K. M., & Sun, C. T. (1991). A refined global–local finite element analysis method. International Journal for Numerical Methods in Engineering, 32(1), 29–43.

  https://doi.org/10.1002/nme.1620320103

- Seon, G., Choi, J., & Kim, H. (2019). Measurement of interlaminar tensile strength and elastic properties of CFRP laminates. Applied Sciences, 9(13), 2647.

  https://doi.org/10.3390/app9132647

- Taherzadeh-Fard, A., Cornejo, A., Jiménez, S., & Barbu, L. G. (2025). Numerical analysis of damage in composites: From intra-layer to delamination and data-assisted methods. Mathematics, 13(10), 1578.

  https://doi.org/10.3390/math13101578

- Huang, T., & Bobyr, M. (2023). A review of delamination damage of composite materials. Journal of Composites Science, 7(11), 468.

  https://doi.org/10.3390/jcs7110468

- Zumaquero, P. L., Justo, J., & Graciani, E. (2018). On the Thickness Dependence of Interlaminar Tensile Strength in Curved Composite Laminates. Key Engineering Materials, 774, 523–528.

  https://doi.org/10.4028/www.scientific.net/KEM.774.523

- Hiel, C. C. (1991). A Curved Beam Test Specimen for Determining the Interlaminar Tensile Strength of a Laminated Composite. Journal of Applied Mechanics, 58(3), 607–615.

  https://doi.org/10.1177/002199839102500705

- Carrera, E., Cinefra, M., Petrolo, M., & Zappino, E. (2014). Finite element analysis of structures through unified formulation. Chichester: Wiley.

https://doi.org/10.1002/9781118536646

- Mathematics Authors. (2022). Series solution-based approach for the inter-laminar stress analysis of angle-ply laminate. Mathematics, 10(2), 268.

  https://doi.org/10.3390/math10020268

- QuEST Global Services. (2014). Delamination damage analysis of curved composites subjected to compressive load using cohesive zone modelling (L-bend composite ILTS study). Technical report, QuEST Global Services, Pune, India. Available online at:

  https://www.questglobal.com/wp-content/uploads/2021/06/Delamination-damage-analysis-of-curved-composites-subjected-to-compressive-load-using-cohesive-zone-modelling.pdf

Appendix A

This appendix reports the symbolic `Maxima` scripts used to derive the curvilinear shell kinematics, metric quantities, energetic operators and kernel properties employed in the numerical implementation described in Chapter 4. The scripts are reported verbatim to ensure full traceability between theory and code.

```
/* Symbolic derivation of local curvilinear geometry */

kill(all);

/* Surface definition */
x(u,v):=u$
y(u,v):=v$
z(u,v):=Auu*u^2 + Auv*u*v + Avv*v^2;

/* Rotation to principal directions */
t:0$
h1:[cos(t), sin(t)]$
h2:[cos(t+%pi/2), sin(t+%pi/2)]$

/* Position vector */
r:[
  x(u,v),
  y(u,v),
  z(u,v)
], u=xi1*h1[1]+xi2*h2[1],
   v=xi1*h1[2]+xi2*h2[2];

/* Covariant basis */
g1:diff(r,xi1);
g2:diff(r,xi2);

```

```
/* Metric quantities */
sprod(u,v):=u[1]*v[1]+u[2]*v[2]+u[3]*v[3]$
vprod(u,v):=[
  u[2]*v[3]-v[2]*u[3],
  u[3]*v[1]-v[3]*u[1],
  u[1]*v[2]-v[1]*u[2]
]$

[g11,g12,g22]:[sprod(g1,g1),sprod(g1,g2),sprod(g2,g2)];
[a1,a2]:sqrt([g11,g22]);

/* Unit normal */
n:vprod(g1,g2)/a1/a2;
```

Listing 6.1: Essential `Maxima` script (`riprovo_curvature`) illustrating the symbolic derivation of the curvilinear surface geometry, covariant bases, and metric quantities used in the proposed ILTS recovery framework.

```
/* ------------------------------------------------------------ */
/*  riprovo_formulazione.mxm       Essential symbolic formulation  */
/* ------------------------------------------------------------ */

/* Simplifying assumptions: constant curvature, principal directions */
kill(all);

[a1,a2] : [1,1]$
R1 : 1/c1$
R2 : 1/c2$

/* Metric scaling through thickness */
[A1,A2] : [a1,a2] * (1 + zeta/[R1,R2])$

/* ------------------------------------------------------------ */
/* Stress resultants (membrane, bending, shear) */
[dN11,dN22,dN12,dN21] : [
  sigma1*(1+zeta/R2),
  sigma2*(1+zeta/R1),
  sigma6*(1+zeta/R2),
  sigma6*(1+zeta/R1)
]*dzeta$

[dM11,dM22,dM12,dM21] : zeta*[dN11,dN22,dN12,dN21]$
```

```
25
26 [Q1,Q2] : Ks*[sigma5*(1+zeta/R2), sigma4*(1+zeta/R1)]*dzeta$
27
28 /* ------------------------------------------------------------ */
29 /* Generalized strain definitions (Reddy-type kinematics) */
30 defs : [
31   ex  = u01,
32   ey  = v02,
33   gxy = u02 + v01,
34
35   kx  = drot2d1,
36   ky  = -drot1d2,
37   kxy = drot2d2 - drot1d1,
38
39   w01 = gzx - rot2,
40   w02 = gzy + rot1
41 ]$
42
43 /* ------------------------------------------------------------ */
44 /* Through-thickness strain reconstruction */
45 eps01 : ex + c1*g$
46 eps02 : ey + c2*g$
47
48 eps11 : kx$
49 eps12 : ky$
50
51 eps1 : 1/(1+zeta/R1)*(eps01 + zeta*eps11)$
52 eps2 : 1/(1+zeta/R2)*(eps02 + zeta*eps12)$
53
54 eps6 : 1/(1+zeta/R1)*(om01 + zeta*om11)
55      + 1/(1+zeta/R2)*(om02 + zeta*om12)$
56
57 eps4 : 1/(1+zeta/R2)*(gzy - c2*q) + dqd_zeta$
58 eps5 : 1/(1+zeta/R1)*(gzx - c1*p) + dpd_zeta$
59 eps3 : dgd_zeta$
60
61 /* ------------------------------------------------------------ */
62 /* Kinematic operator matrix */
63 eps_i : [eps1,eps2,eps3,eps4,eps5,eps6]$
64 di    : [ex,ey,gxy,kx,ky,kxy,gzx,gzy,psi0,psi1]$
65
66 Kmat : coefmatrix(eps_i, di)$
67
```

```
68 /* ------------------------------------------------------------ */
69 /* Flat plate limit (verification) */
70 Kmat, c1=0, c2=0;
```

Listing 6.2: Essential `Maxima` script (`riprovo_formulazione`) illustrating the symbolic derivation of generalized strain measures, through–thickness kinematics, and the associated kinematic operator employed in the ILTS recovery framework.

Appendix B

This appendix reports the complete `Octave` scripts developed in this work to support the numerical implementation and validation of the proposed ILTS recovery framework. The scripts address three complementary aspects: the main post–processing of the Reddy–type shell formulation, the analytical evaluation of equivalent bending loads for two–dimensional FEM models and the moment-driven post-processing formulation.

All scripts are reported in full, without omissions, in order to ensure complete traceability between the theoretical formulation discussed in Chapter 4 and the numerical procedures adopted for the generation of the results.

```
%% ================================================================
%% Post-process Reddy con variabili master e condensazione statica
%% ================================================================

clear all; clc;
pkg load optim;

global o;

%% ---------------- Definizione laminato ----------------
o = struct();
o.zinf = -0.5; % mm (quota inferiore)

% spessori strati
o.hlist = [0.001, 0.1, 0.1, 0.1, 0.1, 0.1, 0.1, 0.1, 0.1, 0.1, 0.1,
```

```
    0.001];
% materiali
o.mlist = [1, 1, 1, 1, 1, 1, 1, 1, 1, 1, 1, 1];
% orientamenti
o.tlist = zeros(1,length(o.hlist));

% --- Materiale 1: Alluminio isotropo (E=70000 MPa, nu=0.3)
E1 = 70000; nu1 = 0.3; G1 = E1 / (2 * (1 + nu1));
o.Dlist(:,:,1) = Dmat_ortho(E1, E1, E1, nu1, nu1, nu1, G1, G1, G1);

% --- Materiale 2: Carbon/Epoxy trasversalmente isotropo (valori da
    roos2007enhanced, table 1)
%% Tipici valori convertiti:
o.Dlist(:,:,2) = Dmat_ortho(...
110000, ... % E1
 10000, ... % E2
 10000, ... % E3
  0.27, ... % nu12
  0.30, ... % nu23
  0.27/110000*10000, ... % nu31 da vij=vji/Ej*Ei, j=1,i=3
  5000, ... % G12
  3846, ... % G23
  5000  ... % G31
);



% Materiale 3: Core isotropo (es. schiuma strutturale Divinycell
   H80 (PVC a celle chiuse))
% da H_Man_M.pdf, p. 27, dati approx.
o.Dlist(:,:,3) = Dmat_ortho(...
80, ... %
80, ... %
80,  ... %
```

```
0.3, ... %
0.3,  ... %
0.3, ... %
80/2.6, ... %
80/2.6,  ... %
80/2.6); ... %

o.n = length(o.hlist);

% suddivisione in sottostrati
nref=3;
m=ones(1,o.n)*5*nref;
m(1)=1; m(end)=1;      % non divido estremali

oldh=o.hlist; oldm=o.mlist; oldt=o.tlist;
k=0;
for i=1:o.n
  for j=1:m(i)
    k=k+1;
    o.hlist(k)=oldh(i)/m(i);
    o.mlist(k)=oldm(i);
    o.tlist(k)=oldt(i);
  end
end
o.n=length(o.hlist);

% quote z
zlist=[0,cumsum(o.hlist)]+o.zinf;
o.zsup=zlist(end);

% curvature geometriche
o.c1=0.0; o.c2=1;

% punti integrazione
```

```
ipn=1; ipx=[0]; ipw=[2]; ipl=sum(ipw);

% inizializzazione
ng=10+3*(o.n+1);
o.L_epsi_dg=zeros(6,ng,o.n,ipn);
o.L_sigmai_dg=zeros(6,ng,o.n,ipn);
o.L_si_dg=zeros(6,ng);
o.H_U_dg=zeros(ng,ng);
o.ipzn=zeros(o.n,ipn);

% definizione L_epsi_dj_strato (unico blocco)
L_epsi_dj_strato = @(c1,c2,za,zb,xi) [...
                  2/((c1*zb-c1*za)*xi+c1*zb+c1*za+2),     0,       0,
                           ((zb-za)*xi+zb+za)/((c1*zb-c1*za)*xi+c1*zb
                     +c1*za+2),     0,       0,       0,       0,       0,
                           0,       0,       0,       -((c1*xi-c1)/((c1*
                     zb-c1*za)*xi+c1*zb+c1*za+2)), 0,       0,       (
                     c1*xi+c1)/((c1*zb-c1*za)*xi+c1*zb+c1*za+2); ...
                  0,       2/((c2*zb-c2*za)*xi+c2*zb+c2*za+2),     0,
                           0,       ((zb-za)*xi+zb+za)/((c2*zb-c2*za)*
                     xi+c2*zb+c2*za+2),     0,       0,       0,       0,
                           0,       0,       0,       -((c2*xi-c2)/((c2*
                     zb-c2*za)*xi+c2*zb+c2*za+2)), 0,       0,       (
                     c2*xi+c2)/((c2*zb-c2*za)*xi+c2*zb+c2*za+2); ...
                  0,       0,       0,       0,       0,       0,       0,
                           0,       0,       0,       0,       0,
                     +(1/(zb-za)),   0,       0,       -1/(zb-za); ...
                  0,       0,       0,       0,       0,       0,       0,
                           2/((c2*zb-c2*za)*xi+c2*zb+c2*za+2),     0,
                           0,       0,       -((2*c2*zb+2)/((c2*zb^2-2*
                     c2*za*zb+c2*za^2)*xi+c2*zb^2+2*zb-c2*za^2-2*za))
                     ,     0,       0,       (2*c2*za+2)/((c2*zb^2-2*c2
                     *za*zb+c2*za^2)*xi+c2*zb^2+2*zb-c2*za^2-2*za),
                              0; ...
```

```
97                  0,      0,      0,      0,      0,      0,
                    2/((c1*zb-c1*za)*xi+c1*zb+c1*za+2),     0,
                    0,      0,      -((2*c1*zb+2)/((c1*zb^2-2*c1*za*
                    zb+c1*za^2)*xi+c1*zb^2+2*zb-c1*za^2-2*za)),
                    0,      0,      (2*c1*za+2)/((c1*zb^2-2*c1*za*zb
                    +c1*za^2)*xi+c1*zb^2+2*zb-c1*za^2-2*za),
                    0,      0; ...
98                  0,      0,      (((c2+c1)*zb+(-c2-c1)*za)*xi+(c2+c1
                    )*zb+(c2+c1)*za+4)/((c1*c2*zb^2-2*c1*c2*za*zb+c1
                    *c2*za^2)*xi^2+(2*c1*c2*zb^2+(2*c2+2*c1)*zb-2*c1
                    *c2*za^2+(-(2*c2)-2*c1)*za)*xi+c1*c2*zb^2+(2*c1*
                    c2*za+2*c2+2*c1)*zb+c1*c2*za^2+(2*c2+2*c1)*za+4)
                    ,   0,      0,      (((c2+c1)*zb^2+(-(2*c2)-2*
                    c1)*za*zb+(c2+c1)*za^2)*xi^2+((2*c2+2*c1)*zb
                    ^2+4*zb+(-(2*c2)-2*c1)*za^2-4*za)*xi+(c2+c1)*zb
                    ^2+((2*c2+2*c1)*za+4)*zb+(c2+c1)*za^2+4*za)/((2*
                    c1*c2*zb^2-4*c1*c2*za*zb+2*c1*c2*za^2)*xi^2+(4*
                    c1*c2*zb^2+(4*c2+4*c1)*zb-4*c1*c2*za^2+(-(4*c2)
                    -4*c1)*za)*xi+2*c1*c2*zb^2+(4*c1*c2*za+4*c2+4*c1
                    )*zb+2*c1*c2*za^2+(4*c2+4*c1)*za+8), 0,     0,
                          (((c2-c1)*zb+(c1-c2)*za)*xi+(c2-c1)*zb+(c2
                    -c1)*za)/((c1*c2*zb^2-2*c1*c2*za*zb+c1*c2*za^2)*
                    xi^2+(2*c1*c2*zb^2+(2*c2+2*c1)*zb-2*c1*c2*za
                    ^2+(-(2*c2)-2*c1)*za)*xi+c1*c2*zb^2+(2*c1*c2*za
                    +2*c2+2*c1)*zb+c1*c2*za^2+(2*c2+2*c1)*za+4),
                           (((c2-c1)*zb^2+(2*c1-2*c2)*za*zb+(c2-c1)*
                    za^2)*xi^2+((2*c2-2*c1)*zb^2+(2*c1-2*c2)*za^2)*
                    xi+(c2-c1)*zb^2+(2*c2-2*c1)*za*zb+(c2-c1)*za^2)
                    /((2*c1*c2*zb^2-4*c1*c2*za*zb+2*c1*c2*za^2)*xi
                    ^2+(4*c1*c2*zb^2+(4*c2+4*c1)*zb-4*c1*c2*za
                    ^2+(-(4*c2)-4*c1)*za)*xi+2*c1*c2*zb^2+(4*c1*c2*
                    za+4*c2+4*c1)*zb+2*c1*c2*za^2+(4*c2+4*c1)*za+8),
                      0,      0,      0,      0,      0,      0; ...
99          ];
```

```
100
101 %% ---------------- Loop sugli strati ----------------
102 for l=1:o.n
103   ja=l; jb=l+1;
104   za=zlist(ja); zb=zlist(jb); dz=zb-za;
105   Dloc=sxy3_from_s123(o.tlist(1))*o.Dlist(:,:,o.mlist(1))*
          e123_from_exy3(o.tlist(1));
106
107   for ipk=1:ipn
108     xi=ipx(ipk);
109     z=za*(1-xi)/2+zb*(1+xi)/2;
110     dV=(1+z*o.c1)*(1+z*o.c2)*dz*(ipw(ipk)/ipl);
111
112     o.L_epsi_dg(:,[1:10,(11:13)+(ja-1)*3,(11:13)+(jb-1)*3],l,ipk) =
            ...
113         L_epsi_dj_strato(o.c1,o.c2,za,zb,xi);
114
115     o.L_sigmai_dg(:,[1:10,(11:13)+(ja-1)*3,(11:13)+(jb-1)*3],l,ipk)
            = ...
116         Dloc*o.L_epsi_dg(:,[1:10,(11:13)+(ja-1)*3,(11:13)+(jb-1)
              *3],l,ipk);
117
118     o.L_si_dg = o.L_si_dg + o.L_sigmai_dg(:,:,l,ipk)*dV;
119     o.H_U_dg = o.H_U_dg + o.L_sigmai_dg(:,:,l,ipk)'*o.L_epsi_dg
          (:,:,l,ipk)*dV;
120
121     o.ipzn(l,ipk)=(z-o.zinf)/(o.zsup-o.zinf)*2-1;
122   end
123 end
124
125 o.H_U_dg=(o.H_U_dg+o.H_U_dg')/2; % simmetrizza
126 o.H_U_dg = o.H_U_dg + 1e-8*eye(size(o.H_U_dg));
127
128
```

```
129
130
131 % parametri numerici di riferimento
132 smallfactor = 1e-4;
133 %kernel per via automatica
134 [o.Kmat,o.kern,o.lmin]=tosymmpd(o.H_U_dg,6,7,smallfactor);
135 %%creo una matrice di rigidezza compensata
136 %o.lmin=smallval*smallfactor;
137 %o.Kmat=o.H_U_dg+o.kern*o.kern'*o.lmin;
138 [vecs,dvals]=eig(o.Kmat);
139 vals=diag(dvals); % vengono restituiti in forma NON NECESSARIAMENTE
        ORDINATA!!!
140 [~,isort]=sort(vals); vals=vals(isort); dvals=dvals(isort,isort);
      vecs=vecs(:,isort);
141
142
143
144
145 %% ---------------- Condensazione statica ----------------
146 % vincolo: uso e11,e22,g12,k11,k22,k12 come input
147 idgcnst = 1:6;
148 % libero: gzx,gzy,phi0,phi1 + assestamenti
149 idgfree = setdiff(1:10+3*(o.n+1),idgcnst);
150
151 % invKff
152 o.invKff=pinv(o.H_U_dg(idgfree,idgfree));
153
154 % costruiamo matrici
155 nm=6;
156 o.L_dg_dm=zeros(10+3*(o.n+1),nm);
157 o.L_dg_dm(idgcnst,:)=eye(6);
158 o.dgb=zeros(10+3*(o.n+1),1);
159 o.fgb=zeros(10+3*(o.n+1),1);
160 o.L_fg_dm=zeros(10+3*(o.n+1),nm);
```

```
161
162 % completamento L_dg_dm su idgfree
163 o.L_dg_dm(idgfree,:) = o.invKff*( ...
164    -o.H_U_dg(idgfree,idgcnst)*o.L_dg_dm(idgcnst,:) ...
165    + o.L_fg_dm(idgfree,:) );
166
167 % matrice ridotta (equivalente ABD)
168 o.rKmat=o.L_dg_dm'*o.H_U_dg*o.L_dg_dm;
169
170 %% ---------------- Input variabili master ----------------
171 dm=[0; 0; 0; 0; -2.704783e-02; 0]; % e11 e22 g12 k11 k22 k12
    analytic method 2d:-2.577344e-02  energetic method 2d:-2.704783e
    -02  k_giusto (al raggio neutro)=-2.705003e-02
172 dg=o.L_dg_dm*dm; % ricostruisco tutti i gradi di libert
173
174 %% ---------------- Post-process sigma_z ----------------
175 cnt=0;
176 z_vals=zeros(o.n*ipn,1);
177 sigma_z=zeros(o.n*ipn,1);
178
179 for l=1:o.n
180   for ipk=1:ipn
181     cnt=cnt+1;
182     z=(zlist(l)*(1-ipx(ipk))/2+zlist(l+1)*(1+ipx(ipk))/2);
183     z_vals(cnt)=z;
184     sig_vec=o.L_sigmai_dg(:,:,l,ipk)*dg;
185     sigma_z(cnt)=sig_vec(3);
186   end
187 end
188
189 %% ---------------- Output ----------------
190 figure;
191 plot(sigma_z,z_vals,'-o');
192 xlabel('\sigma_z'); ylabel('z [mm]');
```

```
193 grid on;
194
195 disp('z_vals (mm):'), disp(z_vals');
196 disp('sigma_z:'), disp(sigma_z');
197
198
199 %% ============================================================
200 %% EXPORT SIGMA_Z VS SPESSORE (Excel     SAFE VERSION)
201 %% ============================================================
202
203 % forza la directory dello script (molto importante)
204 cd(fileparts(mfilename("fullpath")));
205
206 % nome file
207 filename = "sigma_z_lungo_spessore.csv";
208
209 % apertura file
210 fid = fopen(filename, "w");
211
212 % controllo apertura
213 if fid == -1
214     error("ERRORE: impossibile creare il file CSV. Controlla
        permessi o percorso.");
215 end
216
217 % intestazione
218 fprintf(fid, "z_mm;sigma_z_MPa\n");
219
220 % scrittura dati
221 for i = 1:length(z_vals)
222     fprintf(fid, "%.6f;%.6f\n", z_vals(i), sigma_z(i));
223 end
224
225 % chiusura file
```

```
fclose(fid);

disp(["CSV creato correttamente in: ", pwd]);


%% ---------------- Funzioni di supporto ----------------
function D = Dmat_ortho(E1,E2,E3,nu12,nu13,nu23,G12,G13,G23)
  S=[1/E1, -nu12/E1, -nu13/E1, 0,0,0;
     -nu12/E1, 1/E2, -nu23/E2, 0,0,0;
     -nu13/E1, -nu23/E2, 1/E3, 0,0,0;
     0,0,0, 1/G23,0,0;
     0,0,0,0,1/G13,0;
     0,0,0,0,0,1/G12];
  D=inv(S);
end

function e123_from_exy3 = e123_from_exy3 (a)
  c=cos(a); s=sin(a);
  e123_from_exy3=[c^2,1-c^2,0,0,0,c*s;
                  1-c^2,c^2,0,0,0,-c*s;
                  0,0,1,0,0,0;
                  0,0,0,c,-s,0;
                  0,0,0,s,c,0;
                  -2*c*s,2*c*s,0,0,0,c^2-s^2];
end

function sxy3_from_s123 = sxy3_from_s123 (a)
  c=cos(a); s=sin(a);
  sxy3_from_s123=[c^2,s^2,0,0,0,-2*c*s;
                  s^2,c^2,0,0,0,2*c*s;
                  0,0,1,0,0,0;
                  0,0,0,c,s,0;
                  0,0,0,-s,c,0;
                  c*s,-c*s,0,0,0,c^2-s^2];
```

```
end
```

Listing 6.3: Complete Octave main script (`prova_formulazione_reddy.m`) implementing the Reddy–type curvilinear shell formulation, energetic stiffness assembly, kernel identification and static condensation.

```
%% ============================================================
%% MOMENTO EQUIVALENTE DA PRESSIONE RADIALE LINEARE
%% ============================================================

clear; clc;

%% ---------------- Parametri ----------------
p0 = 1000;           % [N/mm^2]
L  = 2.0;            % lunghezza assiale [mm]

r_min = 0.5;         % [mm]
r_max = 1.5;         % [mm]

Nr = 20001;          % suddivisioni radiali
Nnodes = 20;         % nodi attivi (uno tied escluso)

%% ---------------- Griglia radiale ----------------
r = linspace(r_min, r_max, Nr);

%% ---------------- Pressione radiale ----------------
p = p0 * 2 .* (r - 1);    % p(r) = p0 * 2 (r - 1)

%% ---------------- Integrando ----------------
dM = p .* L .* r;         % integrando p(r) * L * r

%% ---------------- Integrazione numerica ----------------
M_linear = trapz(r, dM); % [Nmm]

```

```
%% ---------------- Momento per nodo ----------------
M_node = M_linear / Nnodes;

%% ---------------- Output ----------------
printf('Momento totale      = %.4f Nmm\n', M_linear);
printf('Momento per nodo    = %.4f Nmm\n', M_node);
```

Listing 6.4: Octave script for the analytical evaluation of the equivalent bending moment generated by a linearly varying radial pressure distribution, used as equivalent load input for the 2D FEM shell model.

```
%% ============================================================
%% INPUT TRAMITE MOMENTO FARFALLA (NON PIU k22)
%% ============================================================

% Momento per unit  di lunghezza (N)
M22 = 166.67;    % <-- modifica qui

% e11    libero se il nodo di controllo dell'RBE2    libero di
    spostarsi in direzione assiale (z)
% e22    l'espansione media in dir. circonferenziale, ed    libero
% e12    bloccato se il nodo di controllo dell'RBE2 ha un fixed
    disp. attivo =0 sulla rotz
% k11    bloccato in quanto imponiamo cylindrical bending
% k22    libero o bloccato a seconda della formulazione
% k12    bloccato se il nodo di controllo dell'RBE2 ha un fixed
    disp. attivo =0 sulla rotz
%
%     e11,e22,e12,k11,k22,k12
% a M22 imposto
 mydm=[nan,nan,  0,  0,nan,  0]'; % nan= "libero" o "indefinito"
 myR =[  0,  0,nan,nan,M22,nan]';
%% a K22 imposto
% mydm=[nan,nan,  0,  0,K22,  0]'; % nan= "libero" o "indefinito"
```

```
% myR =[  0,   0,nan,nan,nan,nan]';



% A*x=b
% con all'interno di x, x[ixf] incogniti e x[ixv] vincolati
%      all'interno di b, b[ixf] noti       e b[ixv] incogniti
%
% x(ixf) = inv(A(ixf,ixf))*(b(ixf) - A(ixf,ixv)*x(ixv))
% b(ixv) = A(ixv,ixf)*x(ixf) + A(ixv,ixv)*x(ixv)

ixf=find(isnan(mydm)); %termini liberi/incogniti entro mydm
ixv=find(not(isnan(mydm)));
A = o.rKmat;
b = myR;
x = mydm;
x(ixf) = inv(A(ixf,ixf))*(b(ixf) - A(ixf,ixv)*x(ixv));
b(ixv) = A(ixv,ixf)*x(ixf) + A(ixv,ixv)*x(ixv);
dm = x;

disp('Deformazioni e curvature ottenute:')
disp(dm)



% Ricostruisco DOF completi
dg = o.L_dg_dm * dm;
```

Listing 6.5: Extract of the Octave script highlighting the modified input section, where the bending moment M_{22} is prescribed instead of the curvature k_{22} as in the original implementation. The remaining energetic formulation for the evaluation of the condensed moment–curvature stiffness matrix and the corresponding equivalent nodal bending moments remains unchanged.